Measurement of the $K^+ \to \pi^+ \nu\bar{\nu}$ branching ratio

FERMILAB-PUB-08-065-CD-E

S. Adler,[1] V. V. Anisimovsky,[2] M. Aoki,[3,*] M. Ardebili,[4] A. V. Artamonov,[5] M. Atiya,[1] B. Bassalleck,[6] A. O. Bazarko,[4] B. Bhuyan,[1,†] E. W. Blackmore,[3] D. A. Bryman,[7] S. Chen,[8,3] I-H. Chiang,[1] I.-A. Christidi,[9,‡] M. R. Convery,[4] P. S. Cooper,[10] M. V. Diwan,[1] J. S. Frank,[1] T. Fujiwara,[11] J. Haggerty,[1] J. Hu,[3] T. Inagaki,[12] M. M. Ito,[4] A. P. Ivashkin,[2] D. E. Jaffe,[1] S. Kabe,[12] M. Kazumori,[12,§] Y. Kuno,[12,*] M. Kuriki,[12,‖] S. H. Kettell,[1] M. M. Khabibullin,[2] A. N. Khotjantsev,[2] P. Kitching,[13] M. Kobayashi,[12] T. K. Komatsubara,[12] A. Konaka,[3] A. P. Kozhevnikov,[5] Yu. G. Kudenko,[2] A. Kushnirenko,[10,¶] L. G. Landsberg,[5,**] B. Lewis,[6] K. K. Li,[1] L. S. Littenberg,[1] J. A. Macdonald,[3,**] D. R. Marlow,[4] R. A. McPherson,[4] P. D. Meyers,[4] J. Mildenberger,[3] O. V. Mineev,[2] M. Miyajima,[14] K. Mizouchi,[11] V. A. Mukhin,[5] N. Muramatsu,[15] T. Nakano,[15] M. Nomachi,[16] T. Nomura,[11] T. Numao,[3] V. F. Obraztsov,[5] K. Omata,[12] D. I. Patalakha,[5] S. V. Petrenko,[5] R. Poutissou,[3] E. J. Ramberg,[10] G. Redlinger,[1] T. Sato,[12] T. Sekiguchi,[12] T. Shinkawa,[17] F. C. Shoemaker,[4] A. J. S. Smith,[4] J. R. Stone,[4] R. C. Strand,[1] S. Sugimoto,[12] Y. Tamagawa,[14] R. Tschirhart,[10] T. Tsunemi,[12,††] D. V. Vavilov,[5,‡‡] B. Viren,[1] N. V. Yershov,[2] Y. Yoshimura,[12] and T. Yoshioka[12,§§]

[1]*Brookhaven National Laboratory, Upton, New York 11973, USA*
[2]*Institute for Nuclear Research RAS, 60 October Revolution Pr. 7a, 117312 Moscow, Russia*
[3]*TRIUMF, 4004 Wesbrook Mall, Vancouver, British Columbia, Canada V6T 2A3*
[4]*Joseph Henry Laboratories, Princeton University, Princeton, New Jersey 08544, USA*
[5]*Institute for High Energy Physics, Protvino, Moscow Region, 142 280, Russia*
[6]*Department of Physics and Astronomy, University of New Mexico, Albuquerque, New Mexico 87131, USA*
[7]*Department of Physics and Astronomy, University of British Columbia, Vancouver, British Columbia, Canada V6T 1Z1*
[8]*Department of Engineering Physics, Tsinghua University, Beijing 100084, China*
[9]*Department of Physics and Astronomy, Stony Brook University, Stony Brook, New York 11794, USA*
[10]*Fermi National Accelerator Laboratory, Batavia, Illinois 60510, USA*
[11]*Department of Physics, Kyoto University, Sakyo-ku, Kyoto 606-8502, Japan*
[12]*High Energy Accelerator Research Organization (KEK), Oho, Tsukuba, Ibaraki 305-0801, Japan*
[13]*Centre for Subatomic Research, University of Alberta, Edmonton, Canada T6G 2N5*
[14]*Department of Applied Physics, Fukui University, 3-9-1 Bunkyo, Fukui, Fukui 910-8507, Japan*
[15]*Research Center for Nuclear Physics, Osaka University, 10-1 Mihogaoka, Ibaraki, Osaka 567-0047, Japan*
[16]*Laboratory of Nuclear Studies, Osaka University, 1-1 Machikaneyama, Toyonaka, Osaka 560-0043, Japan*
[17]*Department of Applied Physics, National Defense Academy, Yokosuka, Kanagawa 239-8686, Japan*

(Received 6 September 2007; published 13 March 2008)

Experiment E949 at Brookhaven National Laboratory studied the rare decay $K^+ \to \pi^+ \nu\bar{\nu}$ and other processes with an exposure of 1.77×10^{12} K^+'s. The data were analyzed using a blind analysis technique yielding one candidate event with an estimated background of 0.30 ± 0.03 events. Combining this result with the observation of two candidate events by the predecessor experiment E787 gave the branching ratio $\mathcal{B}(K^+ \to \pi^+ \nu\bar{\nu}) = (1.47^{+1.30}_{-0.89}) \times 10^{-10}$, consistent with the standard model prediction of $(0.74 \pm 0.20) \times 10^{-10}$. This is a more detailed report of results previously published [V. V. Anisimovsky *et al.*, Phys. Rev. Lett. **93**, 031801 (2004)].

PACS numbers: 13.20.Eb, 12.15.Hh, 14.80.Mz

I. INTRODUCTION

Although the standard model (SM) has successfully accounted for all low energy *CP*-violating phenomena thus far observed, it is insufficient as the source of *CP*-violation needed to explain the cosmological baryon asymmetry in our Universe [1]. According to Sakharov [2], one of the conditions necessary to generate such an asymmetry is that the elementary interaction violates charge conjugation symmetry (*C*) and the combined *CP* symmetry (where *P* is the parity symmetry). However, the size of the asymmetry needed for this cannot be derived in model

*Present address: Department of Physics, Osaka University, Osaka 560-0043, Japan.
†Also at: Department of Physics, University of Delhi, Delhi 1100007, India.
‡Present address: Department of Physics, Aristotle University of Thessaloniki, Thessaloniki 54124, Greece.
§Also at: Graduate School of Science, The University of Tokyo, Tokyo 113-0033, Japan.
‖Present address: Graduate School of Advanced Sciences of Matter, Hiroshima University, Hiroshima, 739-8530, Japan.
¶Present address: Institute for High Energy Physics, Protvino, Moscow Region, 142 280, Russia.
**Deceased.
††Present address: Department of Physics, Kyoto University, Sakyo-ku, Kyoto 606-8502, Japan.
‡‡Present address: Department of Physics and Astronomy, Stony Brook University, Stony Brook, New York 11794, USA.
§§Present address: International Center for Elementary Particle Physics, University of Tokyo, Tokyo 113-0033, Japan.

calculations based on the SM [3] and new sources of CP violation have been sought for many years in particle physics experiments. Prominent among these are the rare decays $K \to \pi\nu\bar{\nu}$ which are sensitive to new physics involving both CP-violating and CP-conserving interactions. In this paper, we present a detailed description of the previously reported measurement of the reaction $K^+ \to \pi^+\nu\bar{\nu}$ performed by Brookhaven National Laboratory (BNL) experiment BNL-E949 [4]. This paper is arranged as follows. We first briefly review CP violation and rare kaon decays, with an emphasis on $K^+ \to \pi^+\nu\bar{\nu}$ decays. We then describe previous results on this reaction and discuss the sources of potential background and the methods for suppressing backgrounds. We also discuss the design of the K^+ beam line, the detector and the selection criteria used in data analysis and describe the methods used for estimating background levels and for evaluating the acceptance. After examining the signal region, we present the method used for extracting the branching ratio, making full use of our knowledge of the background in the signal region. In the last section, we show how the measurement of $\mathcal{B}(K^+ \to \pi^+\nu\bar{\nu})$ impacts the search for new physics beyond the SM.

A. CP violation and the rare decay $K^+ \to \pi^+\nu\bar{\nu}$

Standard model CP violation arises from a complex phase in the three-generation quark mixing matrix [5]. In the Wolfenstein parametrization [6] of the Cabibbo-Kobayashi-Maskawa (CKM) matrix, the parameters can be written in powers of $\lambda = \sin\theta_c \approx 0.22$:

$$V_{\rm CKM} = \begin{pmatrix} V_{ud} & V_{us} & V_{ub} \\ V_{cd} & V_{cs} & V_{cb} \\ V_{td} & V_{ts} & V_{tb} \end{pmatrix} \simeq \begin{pmatrix} 1-\lambda^2/2 & \lambda & A\lambda^3(\rho - i\eta) \\ -\lambda & 1-\lambda^2/2 & A\lambda^2 \\ A\lambda^3(1-\rho-i\eta) & -A\lambda^2 & 1 \end{pmatrix}, \tag{1}$$

where A, λ, ρ and η are real numbers. CP invariance of the Lagrangian for weak interactions is violated when the CKM matrix is complex. The parameter η quantifies CP violation in the SM.

The unitarity of the CKM matrix implies six unitarity conditions, which can be represented graphically in the form of triangles, all of which must have the same area. The area of these triangles is equal to one half of the Jarlskog invariant, J_{CP} [7]. Applying the unitarity property $V^\dagger V = 1$ to the CKM matrix in (1) yields

$$V^*_{ub}V_{ud} + V^*_{cb}V_{cd} + V^*_{tb}V_{td} \simeq V^*_{ub} - \lambda V^*_{cb} + V_{td} = 0, \tag{2}$$

where the approximations $V_{ud} \simeq V^*_{tb} \simeq 1$ and $V_{cd} \simeq -\lambda$ have been made. This equation can be represented graphically, as shown in Fig. 1, where we have divided all of the sides by λV^*_{cb}. The apex of the triangle is given by two Wolfenstein parameters, $\bar{\rho}$ and $\bar{\eta}$, where $\bar{\rho} = \rho(1-\lambda^2/2)$ and $\bar{\eta} = \eta(1-\lambda^2/2)$ [8].

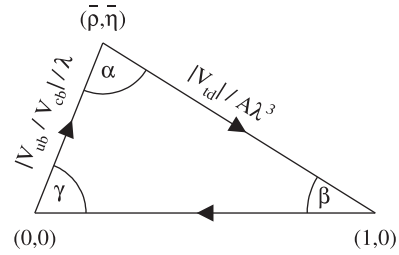

FIG. 1. Unitarity triangles in the $\bar{\rho} - \bar{\eta}$ plane. Two sides of the triangle can be expressed by the CKM matrix elements $|V_{td}|/A\lambda^3$ and $|V_{ub}/V_{cb}|/\lambda$, respectively, where A and λ are parameters in the Wolfenstein parametrization.

B's and K's are so far the only two mesons showing evidence of CP violation in their decay processes. Whether or not the observed CP violation can be completely explained by the CKM phase within the SM can be probed by the independent determination of ρ and η, from B and K decays as shown in Fig. 2. Two sensitive methods for making the comparison are

(i) A comparison of angle β from the ratio $\mathcal{B}(K^0_L \to \pi^0\nu\bar{\nu})/\mathcal{B}(K^+ \to \pi^+\nu\bar{\nu})$ with that from the CP violating asymmetry ($\mathcal{A}_{CP}$) in the decay $B^0_d \to J/\psi K^0_s$; and

(ii) A comparison of the magnitude $|V_{td}|$ from $K^+ \to \pi^+\nu\bar{\nu}$ with that from the mixing frequencies of B_s and B_d mesons, expressed in terms of the ratio of the mass differences, $\Delta M_{B_s}/\Delta M_{B_d}$.

Although the decay $K^+ \to \pi^+\nu\bar{\nu}$ is a flavor changing neutral current (FCNC) process prohibited at tree level in the SM, it is allowed at the one-loop level. In leading order, it is described by a "Box" diagram and two "Z-penguin" diagrams, as shown in Fig. 3. The weak amplitude for this process is represented as

$$\mathcal{M} \sim \sum_{i=u,c,t} V^*_{is}V_{id}\frac{\gamma^\mu q_\mu + m_i}{q^2 - m_i^2}, \tag{3}$$

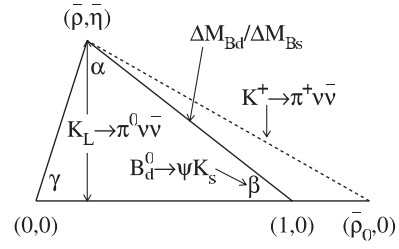

FIG. 2. Unitarity triangle determined by B and K decays. The parameters $\bar{\rho}$ and $\bar{\eta}$ can be determined in two ways: the angle β from the CP-violating asymmetry in the decay $B^0_d \to J/\psi K^0_s$, and from the length of the side from $\Delta M_{B_s}/\Delta M_{B_d}$ in $B - \bar{B}$ mixing; the height of the triangle from $\mathcal{B}(K^0_L \to \pi^0\nu\bar{\nu})$ and the radius of a circle centered at $(\bar{\rho}_0, 0)$ from $\mathcal{B}(K^+ \to \pi^+\nu\bar{\nu})$.

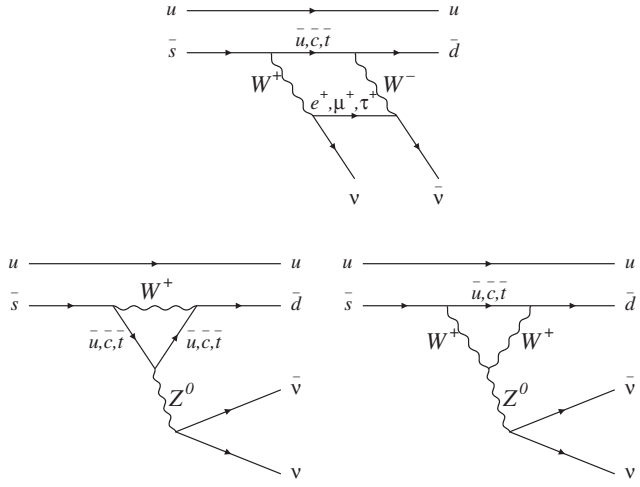

FIG. 3. Second-order weak processes that contribute to the $K^+ \to \pi^+ \nu\bar{\nu}$ branching ratio: the Box diagram (upper) and two "Z-penguin" diagrams (bottom).

where V_{ij}'s are the CKM matrix elements, γ^μ's are the Dirac matrices, q_μ is the momentum transfer, and m_i's are quark masses. $\mathcal{M}$ vanishes if all of the quark masses, m_i, are equal, because of the unitarity of the CKM matrix. However, the breaking of flavor symmetry, which results in the variation of quark masses, allows this decay to proceed at a very small rate. The top quark provides the dominant contribution to the $K^+ \to \pi^+ \nu\bar{\nu}$ branching ratio due to its very large mass in spite of the small coupling of top to down quarks (V_{td}) in the CKM matrix.

Following Ref. [9], the branching ratio for $K^+ \to \pi^+ \nu\bar{\nu}$ is calculated as follows. The effective Hamiltonian can be written in the SM as

$$\mathcal{H}_{\text{eff}}^{\text{SM}} = \frac{G_F}{\sqrt{2}} \frac{\alpha}{2\pi \sin^2\Theta_W} \sum_{l=e,\mu,\tau} (V_{cs}^* V_{cd} X_{\text{NL}}^l + V_{ts}^* V_{td} X(x_t))(\bar{s}d)_{V-A}(\bar{\nu}_l \nu_l)_{V-A}, \quad (4)$$

in next-to-leading order (NLO), where

$$X(x_t) \equiv X_0(x_t) + \frac{\alpha_s(m_t)}{4\pi} X_1(x_t) \approx \eta_X \cdot X_0(x_t) \quad (5)$$

and

$$X_0(x_t) \equiv C_0(x_t) - 4B_0(x_t), \qquad \eta_X = 0.995. \quad (6)$$

$B_0(x_j)$ and $C_0(x_j)$ in (6) are functions of $x_j \equiv m_j^2/M_W^2$, and were derived for the first time by Inami and Lim in 1981 [10]. The coefficient X_{NL}^l and the function $X(x_t)$ are the charm and top quark contributions, including QCD corrections at next-to-next-to-leading order (NNLO) [11–15].

With the top quark mass in the minimal subtraction scheme $m_t(m_t) = (162.3 \pm 2.2)$ GeV [9],

$$X(x_t) = 1.464 \pm 0.025 \quad (7)$$

is obtained.

The perturbative charm contribution gives the largest theoretical uncertainty and can be described in terms of the parameter

$$P_c(X) \equiv \frac{1}{\lambda^4}\left[\frac{2}{3} X_{\text{NL}}^e + \frac{1}{3} X_{\text{NL}}^\tau\right] = 0.34 \pm 0.04, \quad (8)$$

where the error is obtained by varying the charm mass, m_c, the scale factor, $\mu_c = \mathcal{O}(m_c)$, and the coupling constant, $\alpha_s(M_Z^2)$, by reasonable amounts. One obtains

$$\mathcal{B}(K^+ \to \pi^+ \nu\bar{\nu}) = \kappa_+ \cdot \left[\left(\frac{\text{Im}\lambda_t}{\lambda^5} X(x_t)\right)^2 + \left(\frac{\text{Re}\lambda_c}{\lambda}(P_c(X) + \delta P_{c,u}) + \frac{\text{Re}\lambda_t}{\lambda^5} X(x_t)\right)^2\right], \quad (9)$$

where

$$\kappa_+ \equiv r_+ \frac{3\alpha^2 \mathcal{B}(K^+ \to \pi^0 e^+ \nu)}{2\pi^2 \sin^4\Theta_W} \lambda^8 = (5.26 \pm 0.08) \times 10^{-11} \left[\frac{\lambda}{0.2257}\right]^8, \quad (10)$$

$\delta P_{c,u} = 0.04 \pm 0.02$ comprises the long-distance contribution calculated in Ref. [16], and the λ_j's ($\equiv V_{js}^* V_{jd}$) are from the CKM matrix elements. The r_+ ($= 0.901$) represents isospin breaking corrections in relating $K^+ \to \pi^+ \nu\bar{\nu}$ to the well-measured decay $K^+ \to \pi^0 e^+ \nu$ [17]. In obtaining the numerical value in (10), we used [18]

$$\sin^2\Theta_W = 0.231, \qquad \alpha = \frac{1}{127.9}, \qquad \mathcal{B}(K^+ \to \pi^0 e^+ \nu_e) = (4.98 \pm 0.07) \times 10^{-2}. \quad (11)$$

Expression (9) describes in the $\bar{\rho} - \bar{\eta}$ plane an ellipse with a small eccentricity, namely

$$(\sigma\bar{\eta})^2 + (\bar{\rho} - \bar{\rho}_0)^2 = \frac{\sigma \mathcal{B}(K^+ \to \pi^+ \nu\bar{\nu})}{\bar{\kappa}_+ |V_{cb}|^4 X^2(x_t)}, \quad (12)$$

where

$$\bar{\rho}_0 \equiv 1 + \frac{\lambda^4 (P_c(X) + \delta P_{c,u})}{|V_{cb}|^2 X(x_t)}, \qquad \sigma \equiv \left(1 - \frac{\lambda^2}{2}\right)^{-2}, \qquad \bar{\kappa}_+ \equiv \frac{\kappa_+}{\lambda^8}. \quad (13)$$

Using (9) and varying m_t, $|V_{cb}|$, $P_c(X)$ and $|V_{td}|$, which is constrained by $|V_{ub}/V_{cb}|$ and $B - \bar{B}$ mixing in the $\bar{\rho} - \bar{\eta}$ plane, the branching ratio of $K^+ \to \pi^+ \nu\bar{\nu}$ is predicted to be

$$\mathcal{B}(K^+ \to \pi^+ \nu\bar{\nu}) = (0.74 \pm 0.20) \times 10^{-10} \quad (14)$$

within the SM. It should be noted that, of the uncertainty of 27% in (14), the theoretical uncertainty is ~6% at present, mainly due to the uncertainty in the charm quark mass.

Theoretically a precise measurement of $\mathcal{B}(K^+ \to \pi^+ \nu\bar{\nu})$ is one of the cleanest ways to extract $|V_{td}|$. This is due to the following factors:

(i) the long-distance contributions to the branching ratio are small [19] and under control, the most recent calculation gives a contribution of $(+6 \pm 3)\%$ to the branching ratio [16];

(ii) the uncertainty from the hadronic matrix element has been reduced to $<1\%$ by recent theoretical and experimental developments [20], and

(iii) the recent NNLO calculation [14,15] has reduced the total theoretical uncertainties to $\sim 6\%$, i.e., relatively small and reliably calculated as compared with the uncertainties present in other K and B decays.

If a precise measurement of the neutral analog $K_L^0 \to \pi^0 \nu\bar{\nu}$ could also be made, the intrinsic theoretical error on $|V_{td}|$ could be reduced to $\sim 1\%$ [15].

As determinations of B-system parameters become increasingly precise, the uncertainty on the SM prediction for $K^+ \to \pi^+ \nu\bar{\nu}$ will approach the current theoretical accuracy of $\sim 6\%$. A correspondingly precise measurement of the $K^+ \to \pi^+ \nu\bar{\nu}$ branching ratio therefore provides a stringent test of the SM and probes for new physics. There have been numerous predictions for $K^+ \to \pi^+ \nu\bar{\nu}$ in the models beyond the SM and applications of the measured branching ratio to constrain new models. These include the minimal supersymmetric standard model with [21,22] and without [22,23] new sources of flavor or CP violation, generic supersymmetry (SUSY) with minimal particle content [24], SUSY with nonuniversal A terms [25], SUSY with broken R parity [26,27], topcolor [28], topcolor-assisted technicolor models [29,30], multiscale walking technicolor [31], four generation models [32], leptoquarks [33], left-right model with right-handed Z' [34], extension of the SM to a gauge theory with $J = 0$ mesons [35], a multi-Higgs multiplet model [36], light sgoldstinos [37], universal extra dimensions [38], 5-dimensional split fermions [39], a Randell-Sundrum scenario [40], a littlest Higgs model [41,42], nonstandard neutrino interactions [43], and a minimal 3-3-1 model [44].

B. History of $K^+ \to \pi^+ \nu\bar{\nu}$ experiments

Searches for this process which began over 35 years ago have used stopped-K^+ beams. It was believed at the time of the first of these that the branching ratio might be as high as a few $\times 10^{-5}$ [45]. It was recognized that even at this level, a poor-signature process such as $K^+ \to \pi^+ \nu\bar{\nu}$ would need effective particle identification, precise kinematic measurement and the ability to veto extra charged and neutral tracks to discriminate it from common decay modes such as $K^+ \to \mu^+ \nu_\mu$ and $K^+ \to \pi^+ \pi^0$ (referred to as $K_{\mu 2}$ and $K_{\pi 2}$, respectively). The earliest published result was from a heavy liquid bubble chamber experiment [46] at the Argonne Zero Gradient Synchrotron, in which a 90% C.L. upper limit $\mathcal{B}(K^+ \to \pi^+ \nu\bar{\nu}) < 10^{-4}$ was obtained. In that paper it was recognized that $K_{\pi 2}$ decay in flight and hadronic π^+ interaction in the detector were dangerous sources of potential background.

The final analysis of the Argonne experiment improved the limit to 5.7×10^{-5} [47], but before it appeared in print, a subsequent counter/spark-chamber experiment at the Berkeley Bevatron improved the limit to 1.4×10^{-6} [48]. However this experiment was sensitive to only the most energetic of π^+, whereas the bubble chamber experiment covered a wide kinematic range. In addition to the background from common K^+ decay modes, this experiment considered possible background from K^+ charge exchange in the stopping target followed by $K_L^0 \to \pi^+ e^- \bar{\nu}_e$, and from beam π^+ which scattered into the detector. The Chicago-Berkeley group continued their program with a setup sensitive to π^+ in the kinetic energy range 60–105 MeV, i.e., below that of the potential background process $K_{\pi 2}$ rather than above it. This required reconfiguring their photon veto system so that it became nearly hermetic. Combining results from the two configurations, the branching ratio upper limit was improved slightly to 5.6×10^{-7} [49].

About a decade later, an experiment at the KEK Proton Synchrotron improved the limit to 1.4×10^{-7} [50]. The technique of waveform digitization to record the $\pi^+ \to \mu^+ \to e^+$ decay chain was introduced for the first time. This experiment was sensitive only to the π^+ with momenta greater than that from $K_{\pi 2}$ (referred to as the "$\pi\nu\bar{\nu}(1)$" region) and its setup resembled that of Ref. [48].

The BNL series of experiments was initiated in the early 1980s. They were based on a large-acceptance solenoidal spectrometer with a hermetic photon veto situated at the end of a highly pure, very intense stopped-K^+ beam [51] from the BNL Alternating Gradient Synchrotron (AGS). The experimental signature of the $K^+ \to \pi^+ \nu\bar{\nu}$ decay was

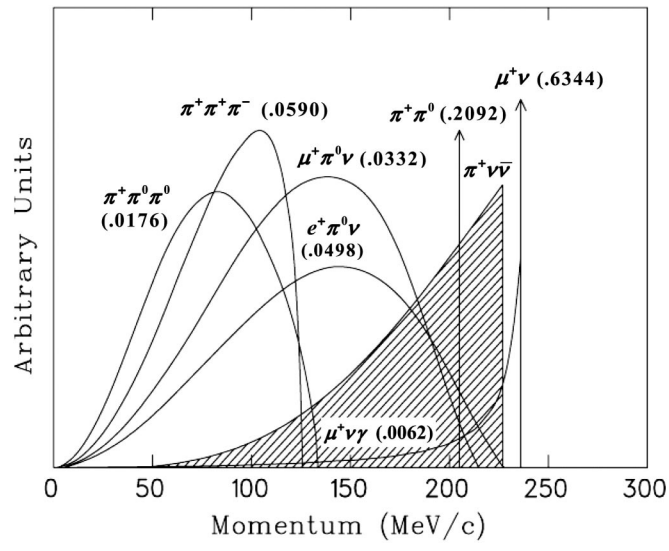

FIG. 4. Momentum spectra (in MeV/c) of charged particles from K^+ decays in the rest frame. The values in the parentheses represent the branching ratios of the decay modes [18]. The hatched spectrum shows the π^+ momentum from $K^+ \to \pi^+ \nu\bar{\nu}$ decay assuming the $V - A$ interaction.

a single π^+ track with π^+ momentum less than 227 MeV/c plus no other particle from a K^+ decay. Figure 4 shows momentum spectra of major decay modes of K^+.

The first phase of E787 in 1988–1991 achieved a 90% C.L. upper limit on the branching ratio of 2.4×10^{-9} [52], using data from the $\pi\nu\bar{\nu}(1)$ region. A separate limit of 1.7×10^{-8} at 90% C.L. [53] was extracted from the kinematic region in which the π^+ is softer than that of the π^+ from $K_{\pi 2}$ (referred to as the "$\pi\nu\bar{\nu}(2)$" region). This program completed the identification of backgrounds needed to reach the 10^{-10} level of sensitivity and developed methods to reliably measure them.

A major upgrade of both the beam line and the detector was undertaken between 1992 and 1994. The search for $K^+ \to \pi^+\nu\bar{\nu}$ resumed in 1995 and continued through 1998. The limit on the branching ratio from the $\pi\nu\bar{\nu}(2)$ region was improved by an order of magnitude to 2.2×10^{-9} at 90% C.L. [54], but the major output of this series of runs was the observation of two clean $K^+ \to \pi^+\nu\bar{\nu}$ events [55] in the $\pi\nu\bar{\nu}(1)$ region and a measurement of the branching ratio $\mathcal{B}(K^+ \to \pi^+\nu\bar{\nu}) = (1.57^{+1.75}_{-0.82}) \times 10^{-10}$. The BNL-E787 detector was upgraded again over the period from 1999–2001. The E949 experiment was proposed to use this detector to run for 60 weeks. After the first 12 weeks of running in 2002 no further funds were provided to complete the experiment. Based on the collected BNL-E949 data, the first result was already published in 2004 [4]. This paper provides an extended and detailed description of the detector and data analysis techniques used to produce the E949 result.

II. EXPERIMENTAL METHOD

A. Overview

E949 (BNL-E949) which succeeded BNL-E787 had a sensitivity goal of detecting ten SM signal events [56]. E949 employed a low momentum beam of K^+'s which were degraded and stopped in the detector. Measurement of the $K^+ \to \pi^+\nu\bar{\nu}$ decay involved observation of the daughter π^+ in the absence of other coincident activity. The π^+ was identified by its kinematic features obtained from energy, momentum and range measurements, and by the observation of a $\pi^+ \to \mu^+ \to e^+$ decay sequence. Since the signal was expected at the 10^{-10} level, the detector was designed to have powerful π^+ identification for rejection of $K_{\mu 2}$ and $K^+ \to \mu^+\bar{\nu}_\mu\gamma$ decays ($K_{\mu 2\gamma}$), 4-π solid angle photon detection coverage for vetoing $K_{\pi 2}$ decays, and efficient K^+ identification system for eliminating beam-related backgrounds.

The entire E949 spectrometer was surrounded by a 1 T solenoidal magnetic field along the beam direction. The coordinate of detector used a Cartesian coordinate system in which the origin was at the center of the target; the $+z$ axis was along the incident beam direction and the $+y$ axis in the vertical up direction as shown in Fig. 5. Under this coordinate system, the azimuthal angle of a track was defined as the arctangent of y/x and, the polar angle θ was defined as the angle with the $+z$ axis. Many detector components have been discussed elsewhere [57–62]. Figure 5 shows the E949 detector after upgrades (1999–2001 [56,63]) with the following improved components: photon veto detection efficiency, tracking and trigger efficiency, and data acquisition (DAQ) live time. E949 was designed to run at the same instantaneous rate as E787, and to achieve a factor of 5 improvement in sensitivity, through the use of a higher duty factor and reduced K^+ momentum for a higher stopping fraction. The higher duty factor was not achieved in the engineering run in 2001 or the first physics run in 2002 due to a broken motor generator set that supplied power to the AGS. The regular supply was removed from operation on August 3, 2001 and the backup was used during the rest of 2001 and 2002. E949 ran at about twice the beam rate of E787.

B. Accelerator and K^+ beam line

The K^+ beam was produced by a high-intensity proton beam from the AGS at BNL: the entire AGS beam of 65×10^{12} protons (Tp/spill) at a momentum of 21.5 GeV/c was delivered to the E949 K^+ production target. Prior to 2001 the AGS typically ran at 24 GeV/c, but at this momentum the longest spill achievable was 0.5 s. Combined with the

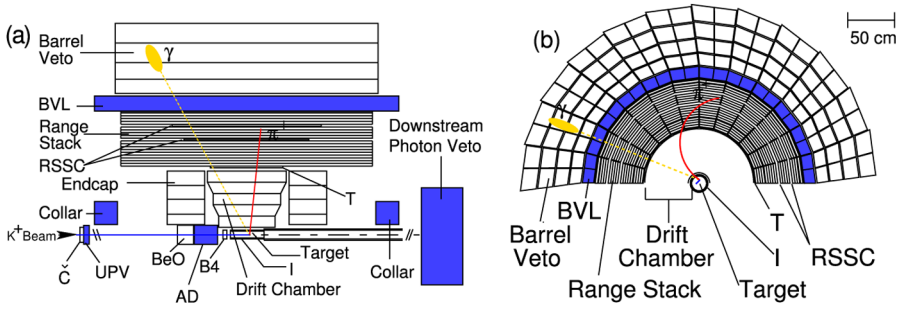

FIG. 5 (color online). Schematic side (a) and end (b) views of the upper half of the E949 detector. Illustrated in this figure, an incoming K^+ that traverses all the beam instruments, stops in the target and undergoes the decay $K^+ \to \pi^+\pi^0$. The outgoing π^+ and one photon from $\pi^0 \to \gamma\gamma$ are also shown. The detector elements and acronyms are described in detail in the text.

longer cycle time (3.2 s between spills, as compared to 2.3 s), the duty factor at 24 GeV/c was unacceptably low. By lowering the proton momentum to 21.5 GeV/c, the spill length was increased to a maximum of 2.2 s, resulting in a duty factor of 2.2 s/5.4 s. At this lower proton momentum the production of 710 MeV/c K^+'s was reduced by 10%. The K^+ production target was made of 2/3 of an interaction length of platinum (6 cm along the beam direction), and was located on a water-cooled copper base. At the typical AGS running condition 65 Tp on the production target per 2.2 s spill, the maximum target temperature was measured to be ~700 °C.

The Low Energy Separated Beam (LESB III) [64] collected and transported K^+'s emitted at 0° (along with 500 π^+'s and 500 protons per K^+), and momentum-selected by the first dipole magnet. Two electromagnetostatic separators swept π^+'s and protons out of the K^+ beam axis. The resulting beam was further selected by a second dipole magnet. LESB III had a total length of 19.6 m from the production target to the E949 target with an angular acceptance of 12 msr and a momentum acceptance of 4.5% FWHM at a mean momentum of 710 MeV/c. During most of the 2002 running period the first separator voltage was lowered from the standard voltage of 600 kV to ~250 kV due to high voltage discharges. Under these conditions a K^+:π^+ ratio in the beam of 3:1 was achieved with a 40% loss in K^+ flux (typically E787 ran with 4:1). Proton contamination was suppressed to a negligible level by the separators. At the same typical AGS running condition described previously, 1.3×10^7 K^+'s were transported through the beam line.

The typical conditions during the 2002 run had 3.5×10^6 K^+'s entering the E949 target every spill. This corresponded to a rate of 1.6×10^6 K^+/s during the 2.2 s spill. The effective spill length was actually 8% shorter (2.0 s) due to some residual modulation of the beam intensity out of the AGS. The typical instantaneous rate of beam particles at the Čerenkov counter was 6.3 MHz of K^+'s and 1.5–2.5 MHz of π^+'s.

C. Beam counters

The incoming K^+ beam traversed a scintillation counter (B0), a Čerenkov counter, two beam wire proportional chambers (BWPCs), a passive BeO degrader, an active degrader (AD) and a beam hodoscope (B4) as depicted in Fig. 5. The BWPCs and B0 counter are not shown in Fig. 5.

The B0 counter, which was a 30.5-cm long, 0.6-cm thick and 7.6-cm wide Bicron BC408 plastic scintillator, was located just downstream of the last quadrupole magnet and counted all charged particles in the beam. It was readout by an analog-to-digital converter (ADC), a time-to-digital converter (TDC) and a 500 MHz transient digitizers based on gallium-arsenide charge-coupled device (CCD) [57]. The Čerenkov counter [51] located just downstream of the B0 counter identified particles as K^+'s or π^+'s. The Čerenkov light from the K^+ (π^+) was transmitted (internally reflected) at the downstream surface of the Čerenkov radiator and readout with 14 "K Čerenkov" (C_K) and 14 "π Čerenkov" (C_π) EMI9954KB photomultiplier tubes (PMTs). The PMT signals were split, with 90% sent to TDCs via fast LRS3412 discriminators and 10% to a ×10 amplifier. The amplifier output was sent to CCDs. The pulse-height information in every 2 ns interval was recorded to reproduce the time development of the pulses and to detect two particles close in time to each other. The multiplicity output of $C_K(C_\pi)$ PMTs was discriminated (typical threshold: $n > 5$) to identify K^+'s and π^+'s in the trigger (KB and πB defined in Sec. II H).

The two BWPCs were located downstream of the Čerenkov counter to monitor the beam profile and identify multiple incoming particles. The first chamber (BWPC1) was located 168.5 cm upstream of the target entrance and contained three planes of sense wires: vertical (x plane) and ±45° to the vertical (u and v planes). The sense wires were 12-μm-diameter gold-plated tungsten. The x, u and v planes had 144, 60 and 60 readout channels, respectively, with a 1.27 mm wire spacing. In the u and v planes, wires in the same plane were multiplexed by 2 in the readout channels. The active area was 17.8 cm (horizontal) by 5.08 cm (vertical). The cathode foils were 25-μm thick aluminized mylar coated with carbon. The anode-cathode distance was 3.18 mm, and the total thickness of BWPC1 was approximately 56 mm. The second chamber (BWPC2) was located 1.0 m downstream of BWPC1 and also contained three planes (x, u and v). The direction of the sense wires was vertical (x plane) and ±60° to the vertical (u and v planes). Each plane had 120 active sense wires with a 0.8-mm wire spacing. Among the 120 wires, the central 72 ones were multiplexed by 3 and the remaining were multiplexed by 6 in the readout channels, yielding a total of 32 readout channels for each plane. The cathode foils were 8-μm single-sided aluminized mylar coated with carbon. The anode-cathode distance was 1.6 mm. Both chambers were filled with a recirculated mixture of CF4 (80%) and isobutane (20%).

Downstream of the BWPCs a degrader slowed the K^+'s so that they stopped in the center of the scintillator fiber target. The upstream section of the degrader was inactive, consisting of 11.11 cm of beryllium oxide (BeO) and 4.76 mm of Lucite. The high density (3.0 g/cm^3) and low atomic number of BeO were used to minimize multiple scattering. The AD consisting of 40 layers of 2 mm thick disks of Bicron BC404 scintillator (13.9 cm diameter) alternating with 2.2-mm thick copper disks (13.6 cm diameter) was divided into 12 azimuthal segments with readout to a single Hamamatsu R1924 PMT through 14 1-mm-diameter Bicron BCF99-29-AA-MC wavelength shifting (WLS) fibers. The PMT outputs were provided to TDCs, CCDs and a fourfold analog sum that was provided to an ADC. These measurements enabled the AD to identify the

beam particles and to detect activity coincident with K^+ decays.

Downstream of the degrader the B4 hodoscope detected the entrance position of the incoming particle in the target and identified the particle type by measuring its energy loss. The B4 hodoscope consisted of two planes, u and v, with about a 11.8-cm diameter oriented at a $\pm 33.50°$ angle with respect to the horizontal axis. Each plane had 16 Bicron BC404 scintillator fingers with a 7.2-mm pitch. The cross section of each finger had a "Z shape" with a 6.4-mm thick middle part and 3.2-mm thick edges. This shape reduced inactive regions and improved the spatial resolution. Three Bicron BCF99-29-AA-MC WLS fibers were embedded in each finger and connected to a single Hamamatsu H3165-10 PMT that was readout by TDCs, ADCs and CCDs. At the same position as the B4 hodoscope, but at larger radius was an annular scintillator counter, the ring veto (RV). The RV was designed to veto particles that passed through perimeter of the B4 hodoscope. The RV was composed of two 180° arcs of 3.3 mm thick Bicron BC404 scintillator with an inner diameter varying from 11.9 to 12.0 cm and an outer diameter of 14.6 cm. The two RV elements were readout by Hamamatsu H3165-10 PMTs and the signals were split three ways to ADCs, TDCs and CCDs.

D. Target

The target consisted of 413 Bicron BCF10 scintillating fibers of 5-mm square cross section and 3.1-m length that were bundled to form a 12-cm-diameter cylinder. A number of 1-, 2- and 3.5-mm square scintillating fibers (called "edge fibers") filled the gaps near the outer edge of the target. Each of the 5-mm fibers was connected to a Hamamatsu R1635-02 PMT, whereas the adjacent edge fibers were grouped onto 16 PMTs, providing signal readout by ADCs, TDCs and CCDs.

The fiducial region of the target was defined by two layers of six plastic-scintillating counters surrounding the target. The inner scintillators, called I counters (ICs), helped to define the fiducial volume and the OR (OR refers to the requirement of at least one of the logical signals) of the six ICs (IC for trigger condition) used by the trigger for this purpose. The ICs were 6.4-mm thick (with an inner radius of 6.0 cm) and extended 24 cm from the upstream face of the target. The outer scintillators, called V counters (VCs), overlapped the downstream edge of the ICs by 6 mm, and served to detect particles that decayed downstream of the fiducial region of the target. The VCs consisted of six 5-mm thick and 1.96-m long scintillators, and were staggered azimuthally with respect to the ICs. Each IC and VC element was instrumented with an EMI 9954KB PMT which was readout by an ADC, TDC and a 500 MHz transient digitizer (TD) based on a flash ADC [58].

Approximately 27% of the incident K^+'s (typically 3.5×10^6 K^+/spill) penetrated far enough into the target to satisfy the online target criteria for KB defined in Sec. II H 2. The remaining K^+'s either underwent decay-in-flight, nuclear interaction in the degrader or scattered in the material of the beam instrumentation and did not reach the target. It should be noted that some of the K^+'s ($<$ 25%) that satisfied the online KB requirement did not stop in the target, and a factor for the stopping fraction of K^+'s was introduced as described in Sec. III H 7. The K^+'s deposited an average energy of 100 MeV in the scintillating fiber target when coming to rest in the center of the target fiducial volume. The low velocity K^+'s typically lost 5–40 MeV in each fiber, while the nearly minimum ionizing (MIP) π^+'s from K^+ decays deposited about 1 MeV per fiber, as they passed transversely through the fibers.

E. Drift chamber

The drift chamber, called the "ultra thin chamber" (UTC) [59], was located just outside of the IC. The primary functions of the UTC were to measure the momenta of charged particles and to provide tracking between the target and the range stack (RS). The UTC had inner and outer radii of 7.85 cm and 43.31 cm, respectively. Twelve layers of 5–8 mm drift cells were grouped into three superlayers (each consisting of four layers) with active lengths of 38.8 cm (inner), 44.8 cm (middle) and 50.8 cm (outer). The superlayers were filled with a 49.8%:49.8%:0.4% mixture of argon, ethane and ethanol. Each anode wire was instrumented with an ADC and a TDC. The drift time to the anode wires was used to determine the (x, y) positions for the charged track. At the inner and outer radii of each superlayer were cathode foils, with 7 mm helical cathode strips at a $\sim$45° pitch angle. Each cathode strip was instrumented with an ADC and a TDC. The combination of the charge centroid on the cathode strips and anode hits provided the z hit position. There were two inactive regions filled with nitrogen gas between the three superlayers. Differential pressures of $\sim$2 mbar in the five gas volumes supported the cathode foils. The total mass of the UTC (excluding the inner and outer support tubes with the attached foils) amounted to 2×10^{-3} radiation lengths. The UTC position resolutions were approximately 175 μm for x and y and 1 mm for z.

F. Range stack

Located just outside the UTC at an inner radius of 45 cm and an outer radius of 84 cm, the RS consisted of both scintillation counters and embedded straw chambers, providing energy and range measurement of the charged particles, information on the $\pi^+ \to \mu^+ \to e^+$ decay sequence and measurement of photon activity.

1. Scintillation counters

The RS consisted of 19 layers of Bicron BC408 plastic scintillator, azimuthally segmented into 24 sectors as

shown in Fig. 5. Layers 2–18 were 1.9 cm thick and 1.82 m long. Layer 19 was 1.0 cm thick and was mainly used to veto longer range muons. Each scintillator in layers 2–19 was coupled through Lucite light guides to EMI 9954KB PMTs at both upstream and downstream ends. The innermost counters were 6.4 mm thick and 52 cm long trigger counters (T counters), defining the fiducial volume for charged K^+ decay products. The T counters were thinner than layers 2–19 to suppress rate from photon conversions. Seventeen 1-mm-diameter WLS fibers (Bicron multiclad BCF-92) with a pitch of 6.9 mm were embedded in each scintillator and coupled to a single Hamamatsu R1398 PMT at each end.

The signal from each PMT of the RS scintillators was passively split 1:2:2 for ADCs, discriminators and fan-in modules, respectively. The discriminator output was sent to a TDC and the trigger. Each PMT was read by an ADC and a TDC. The TDCs (LeCroy 3377) recorded up to 16 hits in a 10.5 μs time window, and thus allowing for efficient detection of the $\mu^+ \to e^+$ decay. The analog fan-in summed the signals from 4 PMTs on each end in the same hextant (four adjacent sectors) and layer. This analog sum was readout by a single TD [58] and was provided to mean timers [63] for good timing on the photon veto in the trigger and a z measurement for each layer of the track. The OR of the mean-timer outputs from each layer in a hextant was provided as input to the hextant photon veto algorithm in the trigger (vetoing more than one nonadjacent hextant). The TDs recorded the charge in 2 ns intervals (500 MHz sampling) in a 2.5 μs time window with a resolution of 8 bits. The 500 MHz sampling provided sufficient pulse-shape information to separate pulses from different events as close as 5 ns apart, and enabled the detection of the $\pi^+ \to \mu^+$ decay as described in Sec. III F 3. The time window of the TDs was narrower than that of the TDCs in order to reduce the data size.

2. Range stack straw chambers

Two range stack straw chambers (RSSCs) were located outside RS layer 10 and 14 [60]. The inner (outer) RSSC consisted of two staggered layers of 24 (28) straws per sector with a length 97.8 (113.0) cm. The average density of an RSSC was 0.054 g/cm^2. Each straw tube was 3.4 mm in radius with a 50-μm-diameter gold-coated tungsten anode wire at the center. A schematic drawing is given in Fig. 6. The straw chambers were operated with 67% argon and 33% isobutane mixture with a trace of water in a self-quenching streamer mode at 3450 V. The local x axis of a chamber was defined to be along the width of the chamber. There were a total of 48 chambers, with 2496 straws installed in the E949 experiment. Because of access restriction, a pair of straws from the right and left halves in the same layer were connected at the upstream end to allow downstream-only readout.

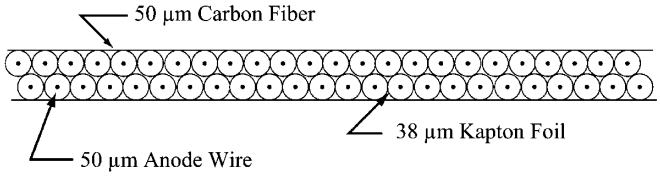

FIG. 6. Schematic end view of the inner RSSC. The tubes run through the beam direction.

The position of the hit straws provided $x - y$ position information, while the end-to-end time differences provided the z measurement. The z resolution of the E787 RSSCs was degraded due to a pulse-height dependent time-walk effect. For E949 an amplifier and two discriminators were installed on each channel to allow for low threshold timing discriminator and a high threshold logic discriminator (above the noise level). The z resolution was improved from 3.0 cm (rms) observed in E787 to 1.5 cm (rms).

G. Photon veto counters

The detection of activity coincident with the charged track was crucial for suppressing background processes that can mimic $K^+ \to \pi^+ \nu\bar{\nu}$. Photons from $K_{\pi 2}$ and other radiative decays were detected by the hermetic photon system as shown in Fig. 5. The photon detectors surrounding the K^+ decay vertex with a 4π solid angle coverage were located in the barrel, upstream and downstream end caps, and near the beam line. The photon system consisted of essentially every scintillator detector in experiment: the barrel veto (BV), the barrel veto liner (BVL), the RS, the upstream and downstream end caps (ECs), the upstream photon veto (UPV), the upstream and downstream collar detectors (CO), the downstream microcollar detector (μCO), the downstream photon veto (DPV), the RV, the IC, the VC, the AD and the target. The regions of the target, IC and RS traversed by the charged track were excluded from the photon veto. The AD and DPV were part of the E949 detector upgrade but were only used in the $\pi\nu\bar{\nu}(2)$ analysis, where photon veto near the beam axis was more important.

The 1.9-m-long, 14.3 r.l. thick BV covering 2/3 of the 4π sr solid angle was located in the outermost barrel region with an inner radius of 94.5 cm and an outer radius of 145 cm [51]. The BV was divided into 48 azimuthal sectors. Each sector consisted of four radial layers, in which there were 16 (innermost), 18, 20, 21 (outermost) layers of 1-mm thick lead and 5-mm thick Bicron BC408 plastic scintillator. The light collected in the scintillators accounted for 30% of the total energy deposit in the BV. The azimuthal boundaries of each sector were tilted so that there were no projective cracks for photons from the decay vertex. Both ends of every module were readout by an EMI 9821KB PMT and the signals were recorded by an ADC and a TDC. The time resolution of individual BV counter was measured to be 1.2 ns.

In order to improve the photon veto capability, the BVL, located between the RS and the BV, replaced the outermost layers 20 and 21 of the RS in E787. Each BVL counter was 10 cm wide and 2.2 m long. There were 48 azimuthal sectors, each with 12 layers of 1-mm thick lead and 5-mm thick Bicron BC408 plastic scintillator, for a total thickness of 2.29 r.l. Both ends of the BVL modules were readout by EMI 9821KB PMTs and the signals were recorded by ADCs and TDCs. The eight adjacent sectors (hextant) in each end were grouped and readout by TDs. The timing resolution of an individual BVL counter was 0.7 ns. A comparison of radiation length coverage with and without the BVL is shown in Fig. 7. A factor of 2 improvement in the photon veto rejection of $K_{\pi 2}$ decays was expected from the BVL.

The ECs had roughly one-third of the 4π sr photon coverage [61]. The upstream EC detector consisted of seventy-five 25 cm long (13.5 r.l.) undoped cesium iodide (CsI) crystals segmented into four rings, and the downstream EC detector consisted of 68 crystals in four rings. To maximize light collection the PMTs were directly coupled to the crystals through a Sylgard cookie formed over the PMT and an ultraviolet transmitting optical filter that selectively passed the fast component of the CsI scintillation light (with a decay time of a few tens of nanoseconds at a wavelength of 305 nm) and blocked the slow component. Since the PMTs were situated in the magnetic field, high-field PMTs were used [62] (Hamamatsu R5543 3" PMTs for the outer three rings and Hamamatsu R5545 2" PMTs for the smaller inner ring crystals); the signals were split to ADCs, constant fraction discriminators (CFD), and CCDs. The CFD's outputs were ORed to provide an online photon veto signal and were also sent to TDCs. The pulses recorded in the CCDs were analyzed offline by a pulse-finding algorithm to provide the timing of the EC signals and to separate two pulses close in time (to reduce the possibility of accidental hits reducing the efficiency of photon detection). Since the EC was exposed to a high counting-rate environment near the beam line, good timing was required to reduce acceptance losses and the masking of $K_{\pi 2}$ photons from early accidental hits.

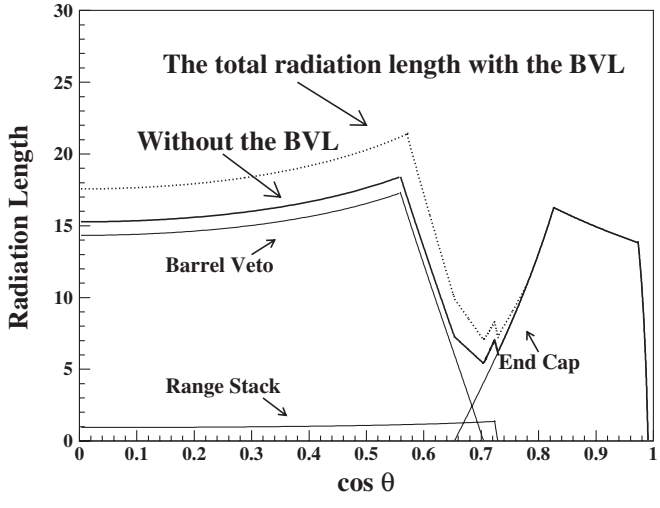

FIG. 7. Radiation length with (solid curve) and without (dotted curve) the BVL as a function of the cosine of the polar angle. These curves account for the contribution from RS, BV, EC and BVL. Other photon veto counters are not accounted for in this plot.

The UPV mounted to the downstream face of the Čerenkov counter was 3.1 r.l. thick, with an outer dimension of 28.4 cm $\times$ 28.4 cm and an inner hole for the beam of 17.5 cm (horizontal) $\times$ 4 cm (vertical). It consisted of 12 layers of 2 mm thick Bicron BC404 plastic scintillator and 1–2 mm thick lead plate. The scintillation light was readout by 12 $\times$ 21 WLS fibers coupled to two Hamamatsu R1924 PMTs. The UPV signals were sent to ADCs, TDCs and CCDs.

The upstream (downstream) CO detector was located just upstream (downstream) of the ECs [65]. Both of the COs consisted of twenty-four 2-mm thick lead sheets alternating with 25 layers of 5-mm thick Bicron BC404 scintillator sheets, providing about 9 r.l. along the beam direction. Each scintillator layer was segmented into 12 wedges forming 12 identical azimuthal sectors. Light from the wedges was readout by WLS multiclad fibers (Bicron BCF99-29AA). Each wedge had 16 fibers glued in grooves in the BC404 scintillator layer. One end of the fiber was polished and aluminized to provide reflective mirror surface. All fibers for each sector ($16 \times 25 = 400$) were terminated in a connector which was coupled to a 1.17-m long Lucite rod via a silicone cookie. The rods transmitted the light to EMI 9954KB PMTs in a low field outside the magnet. Signals were sent to ADCs and TDCs. The COs detected photons emitted with a small polar angle ($0.970 < |\cos\theta| < 0.995$) in both the upstream and downstream regions.

The μCO was installed between the inner face of the magnet end plate and the target downstream of the downstream CO to give more photon detection coverage. The μCO had an inner (outer) diameter of 15.6 cm (20.0 cm) and a length of 53 cm. The eight azimuthal sectors contained eight layers of 2 mm scintillating fibers (from the original E787 target [51]) separated by seven layers of 60 μm Pb. The 536 fibers from two adjacent sectors were readout by one EMI9954 PMT into AD's and TDCs.

H. Trigger

The E949 trigger selected $K^+ \to \pi^+ \nu\bar{\nu}$ events from the large number of K^+ decays and scattered beam particles with requirements on the range of the π^+ track, the presence of a $\pi^+ \to \mu^+ \nu_\mu$ decay in the RS, the absence of other activity at the time of the π^+ and the presence of a K^+ at an appropriately earlier time.

The trigger was composed of two stages: a fast level-0 trigger with a decision time of $\sim$100 ns and a slower level-

1 trigger with a decision time of 10–100 μs. The level-0 trigger was based on signals from the beam, target, RS and photon veto systems, processed with a combination of commercial and custom-built boards. The level-1.n trigger was composed of two parts running in parallel, the level-1.1 and level-1.2 triggers, that involved the partial processing of TD and ADC data, and operated only on events that passed the level-0 trigger.

The original E787 trigger has been described previously [51]. The trigger was upgraded for E949 with the addition of a new programmable level-0 trigger board and mean timers for the photon veto signals [63].

E949 collected data with triggers for the $K^+ \to \pi^+ \nu\bar{\nu}$ signal and for other physics studies and calibrations. In this paper, the triggers for calibration and other physics are referred to as the "monitor" samples.

1. Trigger architecture

For physics and most calibration triggers, level-0 required a signal from the beam system and a charged track in the RS. A beam K^+ or π^+ was identified in NIM logic by a coincidence of hits from the Čerenkov counter, B4 ($B4$), target (*target*) and AGS spill gate (*spill*). This KB signal served as the beam strobe (BS) for the trigger. A charged track $T \cdot 2$ was identified by a coincidence of the IC and T counter and second layer (mean time of the two ends) in a single RS sector. Additional requirements were placed on the crude estimate of the track range, which was the track length derived from the deepest layer of the RS hit in coincidence with the $T \cdot 2$ from that sector or the two proceeding sectors (for a positively charged track). Other requirements were placed on the photon veto (EC, RS, BV, BVL) and the delayed coincidence (DC). The DC was an OR over the six coincidences of the individual ICs and the delayed KB signal such that a track in the IC must typically have occurred at least 1.5 ns later than a prompt signal. The $T \cdot 2$ signal, an OR of the 24 individual sector $T \cdot 2$'s, typically served as the detector strobe (DS) that gated all of the ADCs not associated with the beam system or target and provided a common stop for many of the TDCs; the $T \cdot 2$ signal introduced 40 ns of dead time. When an event passed the level-0 trigger, the dead time was extended to 100 ns to allow further processing. Additional triggers that did not contain both a beam signal and a $T \cdot 2$ were produced on a separate trigger board that fed directly into the trigger bus (with external coordination of the dead time).

The level-1.1 trigger ($L1.1$) was based on information from the TD system for the hextant containing the RS counter in which the charged track was determined to have stopped. Stopped π^+'s were preferentially selected (over μ^+'s) by looking for the $\pi \to \mu$ decay by comparing the pulse height to the pulse area (for early decays) or by looking for a second detached pulse. This was done by a custom-built application-specific integrated circuit (ASIC) which had access to the TD memories. The ASIC could also reduce the TD data size for readout by discarding the waveform samples outside the "prompt" time window, keeping instead a calculation of the pulse area and leading-edge time. The prompt window typically extended from 0.5 (2) μs before (after) the π^+ track. Level-1.1 typically provided a decision in about 10–20 μs.

The level-1.2 ($L1.2$) used data digitized by the ADCs and had two components. One of them, the "level-1.1 afterburner" rejected events with an accidental hit near the stopping counter. Such hits might defeat the level-1.1 with an apparent double pulse. The other component, the "*HEX* afterburner," was used for the photon veto, rejecting events with hits in both of the two adjacent hextants when the $T \cdot 2$ counter and the stopping counter were found in the same hextant. This usually indicated that a single hextant fully contained the trajectory, thus those observed in the other hextant came from another particle. The level-1.2 trigger introduced a dead time of up to 100 μs per level-1.1 trigger.

2. $K^+ \to \pi^+ \nu\bar{\nu}$ triggers

The triggers as described below were valid for the bulk of the 2002 running period. The trigger conditions for $K^+ \to \pi^+ \nu\bar{\nu}$ were designed differently according to the π^+ momentum. For high π^+ momentum, the $\pi\nu\bar{\nu}(1)$ trigger condition was defined as

$$\begin{aligned}\pi\nu\bar{\nu}(1) = {} & KB \cdot DC \cdot (T \cdot 2) \cdot (6_{ct} + 7_{ct}) \cdot \overline{19_{ct}} \cdot \overline{zfrf} \\ & \cdot L0rr1 \cdot \overline{(BV + BVL + EC)} \cdot HEX \\ & \cdot L1.1 \cdot L1.2, \end{aligned} \tag{15}$$

where

$$KB = C_K \cdot B4 \cdot \text{target} \cdot \text{spill}. \tag{16}$$

The $6_{ct} + 7_{ct}$ required that the π^+ reached the 6th or 7th layer of the RS and suppressed the copious 3-body $K^+ \to \pi^+\pi^-\pi^+$ and $K^+ \to \pi^+\pi^0\pi^0$ backgrounds. The $\overline{19_{ct}}$ signal required that the charged track should not reach the 19th layer in order to suppress $K_{\mu 2}$ background. The "ct" designated the RS sectors that were associated with a $T \cdot 2$ ($T \cdot 2$ sector plus the next two clockwise sectors: this was the direction that a positive particle moved in the magnetic field). The $\overline{zfrf}$ condition was a fiducial cut on the z position of the charged track in each layer, vetoing tracks that exited the fiducial volume. The $L0rr1$ was a refined calculation of the charged track range, which included the number of target fibers hit and a measurement of the z position of the track from flash TDCs on layers 3 and 11–13 as well as the deepest layer of penetration of the track; this rejected events with long range such as the μ^+ from $K_{\mu 2}$ decay. The photon veto $\overline{BV + BVL + EC}$ and HEX were from the BV, BVL, EC and RS, respectively, which removed events with photons such as $K_{\pi 2}$, $K_{\mu 3}$ and $K_{\mu 2\gamma}$.

The number of K^+'s which met the KB trigger requirement when the detector was live (N_K) was recorded at the end of each AGS spill. The total exposure from the $\pi\nu\bar{\nu}(1)$ trigger data stream was

$$N_K = 1.77 \times 10^{12}. \tag{17}$$

E949 also provided a $\pi\nu\bar{\nu}(2)$ trigger for lower momentum π^+'s. Since the study involves different background mechanisms and a different kinematic region, the result will be presented in a separate paper.

3. Monitor triggers

In addition to the $K^+ \to \pi^+\nu\bar{\nu}$ triggers, there were monitor triggers for calibration and normalization, as well as triggers for other physics modes. All triggers were prescaled to reduce the impact on the total dead time except for the $K^+ \to \pi^+\nu\bar{\nu}$ triggers and the "γ" trigger which required the presence of photons in the barrel region for studying $K^+ \to \pi^+\gamma\gamma$ and $K^+ \to \pi^+\gamma$ decays [66].

To monitor detector performance several processes were employed, including $K_{\pi 2}$ and $K_{\mu 2}$ decays, beam particles scattered into the detector fiducial volume, beam K^+, charge exchange events and cosmic rays. These monitor samples were used for calibration and acceptance studies. They were taken simultaneously with the $\pi\nu\bar{\nu}(1)$ and $\pi\nu\bar{\nu}(2)$ triggers to reflect any condition changed into the acceptance and background calculations.

The $K_{\mu 2}$ decay has the largest branching ratio. Since the final state does not contain photons or additional tracks and the daughter μ^+ does not interact strongly, it was a convenient sample for a variety of acceptance measurements as well as several calibrations. This sample was also used for the normalization of the experiment; the measurement of the $K_{\mu 2}$ branching ratio effectively normalized the counting of K^+ stops to the well-known $K_{\mu 2}$ branching ratio. The $K\mu 2$ trigger condition for $K_{\mu 2}$ was defined as follows

$$K\mu 2 = KB \cdot (T \cdot 2) \cdot (6_{ct} + 7_{ct}) \cdot (17_{ct} + 18_{ct} + 19_{ct}). \tag{18}$$

The final state of the $K_{\pi 2}$ decay mode contains one charged π^+ and two photons from π^0 decay. Since the π^+ momentum is monochromatic, the $K_{\pi 2}$ sample was used to check the measurement of the charged track momentum, range and energy. Also the π^+'s were used to study particle identification, while the photons were used to study the photon veto. Two $K_{\pi 2}$ triggers were defined, a loose one, $K\pi 2(1)$:

$$K\pi 2(1) = KB \cdot (T \cdot 2) \cdot (6_{ct} + 7_{ct}) \cdot \overline{19_{ct}}, \tag{19}$$

and a tighter one, $K\pi 2(2)$:

$$K\pi 2(2) = K\pi 2(1) \cdot HEX \cdot L1.1 \cdot L1.2. \tag{20}$$

The $K\pi 2(2)$ monitor trigger was used only for calibration in this analysis.

Among the incoming beam particles there were many π^+'s, including some that scattered into the fiducial volume of the RS. These π_{scat} events were identified as π^+'s by the C_π and had an in-time track in the RS. The kinematic features of this π^+ sample were almost the same as the $K^+ \to \pi^+\nu\bar{\nu}$ signal except that the target pattern was different. This sample was suitable for calibrating the ionization energy loss (dE/dx) of π^+'s and for studying the acceptance. The trigger condition for scattered beam particles was defined as

$$\pi_{\text{scat}} = \pi B \cdot \overline{DC} \cdot (T \cdot 2) \cdot (6_{ct} + 7_{ct}) \cdot \overline{(BV + BVL + EC)} \cdot HEX, \tag{21}$$

where

$$\pi B = C_\pi \cdot B4 \cdot \text{target} \cdot \text{spill}. \tag{22}$$

The charge exchange process (CEX), $K^+n \to p + K^0$ followed by $K_L^0 \to \pi^+ l^- \bar{\nu}_l$ can mimic $K^+ \to \pi^+\nu\bar{\nu}$ events when the charged lepton l^- from the K_L^0 decay had a low momentum and was undetected. The largest uncertainty in this background was the determination of the reaction rate. Since K^0 has an equal fraction of K_L^0 and K_S^0, the $K^+n \to p + K_S^0$ process with a K_S^0 decay to $\pi^+\pi^-$ can be used to measure the reaction rate for the determination of the background from $K^+n \to p + K_L^0$. Since the $K_S^0 \to \pi^+\pi^-$ could be cleanly identified, a CEX trigger with two charged tracks was defined as

$$\text{CEX} = KB \cdot \overline{DC} \cdot 2(T \cdot 2) \cdot (6_{ct} + 7_{ct}) \cdot \overline{EC + \pi B}. \tag{23}$$

In addition, we also defined triggers for beam K^+ and cosmic ray, which were used in trigger efficiency measurement and detector geometrical alignment.

I. Data acquisition

Analog and discriminated signals from the detector were digitized by commercial ADC and TDC, and custom-built waveform digitizer (TD and CCD) systems. When an event was accepted by the trigger system, the digitized data for the event were transferred to a buffer module or a local crate controller. At the end of each spill, the data for the spill were transferred to a host computer. A summary of the digitizing electronics is shown in Table I.

For the Fastbus systems, SLAC Scanner Processor (SSP) modules [67] served as crate controllers and also to readout, reformat and buffer the data from the front end after each trigger accepted. The CAMAC ADCs were readout through the FERA bus by a Struck 370 QDP DSP (Fastbus) module. The CAMAC TDCs were readout by custom-built DYC3 modules [68] which pushed the data into Versa Module Eurocard (VME) memory boards. The readout time per event (as determined by the slowest crate) was typically 850 μs.

TABLE I. Digitizing electronics for E949.

Type	Model	Standard	Resolution	Subsystems
ADC	LRS 4300B	CAMAC	10 bits	RS, BV, BVL, EC, Beam
	LRS 1881	Fastbus	13 bits	Target, UTC
TDC	LRS 3377	CAMAC	0.5 ns	RS, BVL
	LRS 1879	Fastbus	2 ns	UTC, BV, Target
	LRS 1876	Fastbus	1 ns	EC, RSSC, Beam
WFD	TD	Fastbus	500 MHz sampling 8 bits, up to 10 μs depth	RS, BVL, IC
	CCD	Fastbus	500 MHz sampling 8 bits, 256 ns depth	Beam, Target, EC

At the end of each spill, the data from the Fastbus buffer memories were readout via the cable segment (12–15 MB/s) by Struck 340 SFI modules, each controlled by a Motorola VME 2604 single-board computer (SBC) running VxWorks. The VME memory boards were readout by a separate SBC. Data were transferred from the SBCs to the host computer (SGI Origin 200) via ethernet (9 MB/s per link) through a simple network switch. Event fragments from the readout segments were combined by event builder processes running on the host computer. Complete events were distributed to "consumer" processes which included data logging and online monitoring. The $K^+ \to \pi^+\nu\bar{\nu}$ triggers were written to two DLT-7000 drives at 5 MB/s per drive; a third DLT drive was used to log monitor triggers.

A slow control system, based on the MIDAS [69] framework, ran independently of the main DAQ system and was used to monitor a variety of experiment conditions, including crate voltages and temperatures.

Under typical running conditions, we wrote ~300 events per spill with a typical event size of ~80 kB. This was well within the maximum throughput of the system of about 50 MB/spill. The DAQ dead time was due entirely to the speed of the event-by-event readout of the front-end electronics at the crate level. The total dead time introduced by the trigger and DAQ was typically 26%. The E949 experiment collected its physics data for 12 weeks from March through June of 2002 or about 20% out of the total beam time approved by DOE's Office of High Energy Physics.

III. DATA ANALYSIS

The branching ratio of the $K^+ \to \pi^+\nu\bar{\nu}$ decay in the SM is $\sim 10^{-10}$ as discussed in Sec. I. Unlike the $K_{\mu 2}$ and $K_{\pi 2}$ backgrounds, the $K^+ \to \pi^+\nu\bar{\nu}$ signal is continuous with no peak. To establish that any possible observed candidate event was really from $K^+ \to \pi^+\nu\bar{\nu}$, we required that the backgrounds were suppressed to a level substantially below one event with small uncertainty. All the detectors were calibrated before the background and acceptance studies using $K\mu 2$, $K\pi 2(1)$, $K\pi 2(2)$ and cosmic-ray and beam trigger events. After a brief overview of the background sources, the data analysis technique will be described: including selection criteria, background evaluation, acceptance measurement and the signal candidate search.

A. Overview of background

Data selected by the $\pi\nu\bar{\nu}(1)$ trigger were primarily from background events as shown in Fig. 8. These events were classified into stopped-K^+-decay-related and beam-related backgrounds.

1. Origins of stopped-K^+-decay background

The stopped-K^+-decay backgrounds were categorized into two types: π^+-related, μ^+-related backgrounds. As can be seen in Fig. 4, multibody K^+ decays were suppressed by setting a signal momentum region higher than the $K_{\pi 2}$ peak but lower than the $K_{\mu 2}$ peak. However, since $K_{\pi 2}$ and $K_{\mu 2}$ have such large branching ratios (20.92% and 63.44% [18]), migration into the signal region through either resolution or scattering effects was a significant

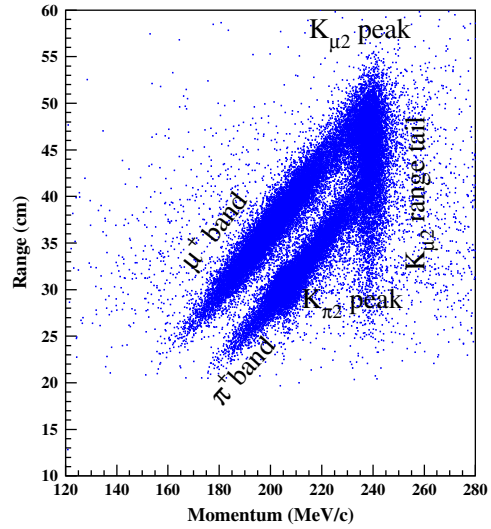

FIG. 8 (color online). Range in plastic scintillator (cm) versus the momentum (MeV/c) of the charged particles for events that passed the $\pi\nu\bar{\nu}(1)$ trigger. These data represent ~0.3% of N_K.

background. Radiative $K_{\mu 2}$ decay and $K^+ \to \mu^+ \pi^0 \nu$ ($K_{\mu 3}$) decays accounted for the majority of the observed μ^+ band events in Fig. 8. For the $K_{\mu 2}$ decay mode, the background originated from a $K_{\mu 2}$ peak event or a $K_{\mu 2}$ low momentum ("tail") event if the particle identification was fooled. This was also applicable to the $K_{\pi 2}$ decay mode when the photons escaped detection. Because of phase space limits, the $\pi\nu\bar{\nu}(1)$ analysis only needed to consider the K^+-decay-related backgrounds from the $K_{\mu 2}$, μ^+ band and $K_{\pi 2}$ decay.

2. Origins of beam background

The beam-related backgrounds were categorized into three types: single-beam background, double-beam background and CEX background. The first two beam backgrounds accounted for most of the π^+ band shown in Fig. 8.

The single-beam background consisted of the following components. (1) A K^+ entered the target and decayed in flight to a π^+ plus a π^0 as illustrated in Fig. 9. The kinematic values of the π^+ were shifted upward to the signal region by the Lorentz boost, faking a $K^+ \to \pi^+ \nu\bar{\nu}$ signal event. (2) A π^+ in the beam was misidentified as a K^+, scattered in the target and entered the fiducial region of the detector as illustrated in Fig. 9. This π^+ (referred to as scattered π^+) could mimic the target fiber pattern for signal and have kinematic values in the signal region. Rejection of these two background types required both good π^+/K^+ beam identification and time resolution for delayed coincidence measurements.

The following cases were classified as the double-beam background. A K^+ came to rest in the target accompanied by another K^+ entering the target that decayed in flight to a π^+, which traversed the fiducial region of the detector (Fig. 10). The second case was similar, except that the beam π^+ scattered in the target and entered the fiducial region (Fig. 10). Both cases could imitate a $K^+ \to \pi^+ \nu\bar{\nu}$ signal if the decay products from the first K^+ were missed. Rejection of these two backgrounds relied on the observation of extra activities in either the beam instrumentation or

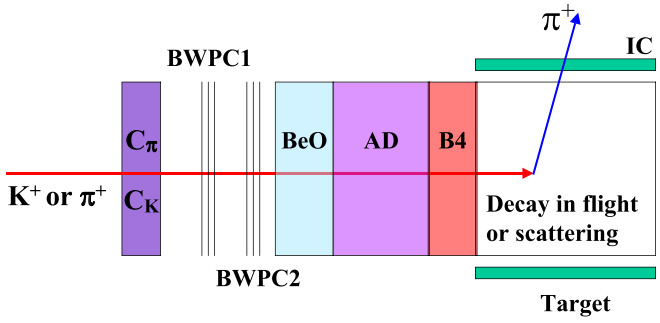

FIG. 9 (color online). Schematic diagrams of the single beam background: (1) single beam K^+ background and (2) single beam π^+ background. The various detector elements and acronyms are described in the text.

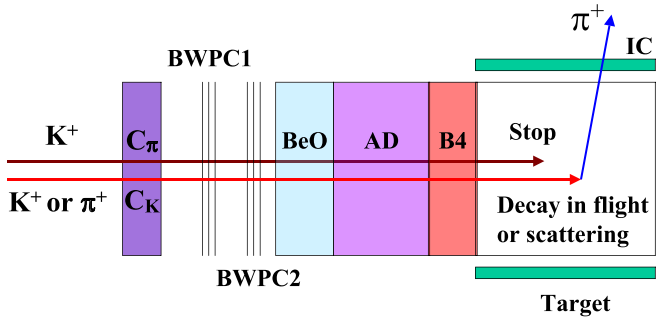

FIG. 10 (color online). Schematic diagrams of the double beam background: (1) double beam $K^+ - K^+$ background and (2) double beam $K^+ - \pi^+$ background. The various detector elements and acronyms are described in the text.

the target coincident with the delayed π^+ detected by the RS.

The CEX background could occur if a K^+ produced a K^0 in the target and if the K^0 turned into a K_L^0 that subsequently underwent semileptonic decay. This process could produce background if the charged lepton from a K_L^0 decay was undetected and the π^+ satisfied the kinematics of the signal region (Fig. 11). Rejection of the CEX background was achieved by using the fact that a K_L^0 usually did not deposit energy along the path in the target, leaving a gap observed between K^+ and π^+ fibers in the target. Also exploited was matching between the reconstructed z position of the decay and the energy deposited by the incoming K^+ and the short flight time of K_L^0 in the target.

B. Analysis method and strategy

Disentangling the $K^+ \to \pi^+ \nu\bar{\nu}$ decay from background in this experiment was challenging due to the poor kinematic signature and very small expected rate of the $K^+ \to \pi^+ \nu\bar{\nu}$ signal. These necessitate enormous suppression of background events by rejecting events with very low levels of extraneous activity. This high level of veto makes it impractical to accurately simulate the background rejection power of the detector at the required $\sim 10^{-10}$ level of sensitivity. Therefore, an accurate estimate of the background must be obtained from the data.

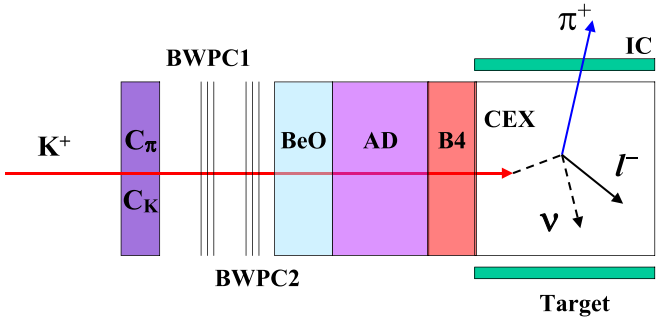

FIG. 11 (color online). Schematic diagram of the charge exchange interaction background. The various detector elements and acronyms are described in detail in the text.

1. Blind analysis method

A "blind" analysis method was developed to search for the $K^+ \to \pi^+ \nu\bar{\nu}$ signal in data samples. In this method, background sources were identified *a priori*. The signal region for the $\pi\nu\bar{\nu}(1)$, determined so that the sensitivity was optimized, was "blinded" or hidden until the background and acceptance analysis was completed. When possible, selection criteria were developed using the monitor samples to avoid examining the signal region. If monitor samples were inadequate and the $\pi\nu\bar{\nu}(1)$ trigger sample were required, at least one selection criterion distinguishing signal from backgrounds was inverted (i.e., used to select a background region) to avoid examining the signal region. In addition, the final background estimates were obtained from different samples than that used to determine the selection criteria. Each set of three consecutive $\pi\nu\bar{\nu}(1)$ events were selected for "1/3" and "2/3" sample groups. The 1/3 group was used to determine the selection criteria and an unbiased background estimate was obtained from the 2/3 group. The signal region was examined only after the background analysis was completed.

2. Bifurcation method for evaluating background

The principal method for background evaluation relied on information from outside the signal region and involved the application of two complementary but uncorrelated cuts. Figure 12 illustrates this bifurcation method showing the parameter space of two cuts, "CUT1" and "CUT2." The number of background events in the signal region (i.e., region "A") was A events. If the two cuts are uncorrelated, that is, if the rejection of a cut does not depend on the rejection of the other cut, the ratio of the number of background events in region A to region "B" must be equal to the ratio in region "C" to region "D," i.e., $A/B = C/D$. Background events in the signal region are therefore obtained from the relation $A = BC/D$.

In practice, the present bifurcation analysis was done through two branches. A "normalization branch" analysis was used to obtain the number of events in B region. A "rejection branch" study was done to get the ratio of D/C. The rejection was defined as $R = (C + D)/C$. The background level in the signal region was then estimated as $N_{\rm bkg} = B/(R - 1)$. For the case of very small statistics,

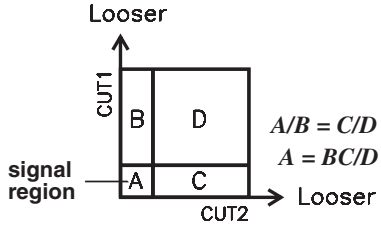

FIG. 12. Pictorial explanation of the bifurcation method. Background level in region A can be estimated from the observed number of events in the other regions, if CUT1 and CUT2 are uncorrelated.

CUT1 was subdivided into two cut categories, and B was estimated in the same way as the "first" bifurcation.

To check if the two bifurcated cuts were uncorrelated, cuts were loosened simultaneously (as described in Sec. IV A). The loosening factors were controlled by the predicted background functions, in which the loosening factors were the inputs and the outputs were the cut positions. By design the functions provided the relative background level and the acceptance. The background level provided by the functions should agree with the observed number of events within the newly defined regions if CUT1 and CUT2 were uncorrelated. This method thus provided input to the evaluation of systematic uncertainties (Sec. III G 10).

3. Analysis strategy

The data analysis used the following key steps to determine the selection criteria, evaluate the background level, investigate the systematic uncertainty, measure the acceptance and finally obtain the branching ratio.

(i) Data were first reconstructed and processed with a number of selection criteria to remove obviously bad events. Then the surviving events were divided into 1/3 and 2/3 portions, in which three subsamples were also skimmed out according to different background features (Sec. III E).

(ii) Blind analysis was adopted in designing, calibrating and tuning the selection criteria. Signal-like and background samples were taken from the monitor trigger samples when applicable. When the three skimmed subsamples were used to have the same experimental features of the signal, at least one critical selection criterion was inverted to avoid examining the signal region (Sec. III F).

(iii) The background level was initially evaluated by applying the bifurcation method to the 1/3 data and controlled to be much less than one event by tuning the selection criteria. At least two uncorrelated cuts with large background rejections were chosen. data samples (Secs. III G 1–III G 5).

(iv) The final cut positions were optimized with respect to the signal-to-background level estimated from the 1/3 data. This was achieved using the predicted background functions estimated in the bifurcation analysis (Secs. III G 6 and III G 7).

(v) Correlations between the bifurcated cuts were checked by conducting a series of reevaluations of the background levels outside the signal region. A study of single cut failure was also conducted to investigate a possible flaw in the technique. To avoid the potential bias of the 1/3 background study, the final background evaluations were taken from the 2/3 portion (Secs. III G 8 and III G 9).

(vi) Acceptances were measured with the monitor trigger samples except for the signal phase space, the trigger

efficiency and those that could not be extracted from the monitor trigger data. These were obtained from Monte Carlo (MC) simulations. The branching ratio of $K_{\pi 2}$ was used to validate the acceptance measurement. Single event sensitivity was obtained from the total K^+ exposure and the acceptance (Sec. III H).

(vii) The signal region was examined. Events observed in this region were all considered as the signal candidates (Sec. III I).

(viii) The branching ratio was obtained from a likelihood analysis incorporating the predicted background rate and acceptance within the signal region (Sec. IV).

C. Track reconstruction

Throughout this analysis, the events were reconstructed under the assumption that they were $K^+ \to \pi^+ \nu \bar{\nu}$ events with only a single π^+ track in the detector.

1. Beam time measurements

To fully reconstruct an event, the initial time of the beam particle was required. The beam instruments provided several beam times from TDC and CCD measurements on the C_K, the C_π, the BWPC and the B4. For the TDC measurements, offline analysis treated all PMT hits coincident with each other as a cluster. The average time of the TDC hits in each cluster gave t_{C_K}, t_{C_π}, t_{BW} and t_{BM}, respectively. The CCD measurements were used to discriminate cases with more than one particle in a beam (referred to as pileup).

2. Clustering in the RS

The track reconstruction routine started by finding clusters in the RS. The hit counters of a positively charged track (the track counters) were searched for using the TDC timing information in the RS. A good $T \cdot 2$ sector was found as that closest in time to the DS. From this $T \cdot 2$ sector, adjacent counters in subsequent layers within 10 ns of the $T \cdot 2$ time and with energy greater than 0.5 MeV were selected in the outgoing and clockwise direction to find the track counters. A good cluster involved at least six consecutive layers from inside to outside. Once an RS track cluster was identified, the track time (t_{rs}) was computed by averaging all the time measurements of the track counters. The stopping counter was defined as the one in the outermost layer which was in the most clockwise direction. The $T \cdot 2$ sector in a cluster served as a guide for tracking in UTC.

3. Tracking in the UTC

When an RS cluster was established, the UTC tracking routine started searching for clusters of hit anode wires in the $x - y$ plane [59]. Hit wires in each superlayer were grouped into clusters based on their spatial proximity to one another. A straight line fit provided a crude vector in each superlayer. The solutions due to the left-right ambiguity were included at this stage. These vectors were then linked to form a track segment in the UTC. A circle fit was performed with a set of drift distances with left-right ambiguity resolution. The radius of the circle gave the measurement of transverse momentum.

If a UTC track in the $x - y$ plane was found, the corresponding track projection on the $\phi - z$ plane (ϕ was defined as the revolution angle with respect to the closet approach to the vertex) was then sought in the clusters of hit strips on the UTC cathode foils. A time window of ± 15 ns was used to reduce the accidental hits. The calculation of the z position for a cluster adopted the ratio method suggested by Ref. [70], which used the three strips with the highest ADC counts to derive the centroid and to reduce the bias on the z position measurement. A straight line fit was performed in $\phi - z$ plane if the z hits were found in at least 3 foils, thus determining the slope and intercept. The slope was then used to convert the measured transverse momentum to the total momentum.

In case of more than one track pointing to the same $T \cdot 2$ sector, a good UTC track was defined as the one closest to the first RS sector crossing point or to the clockwise edge of the stopping counter otherwise. The UTC tracking efficiency was checked with the $K\mu 2$ monitor data and was measured to be better than 95%. The inefficiency was due to the fact that for the high rate environment accidental hits in the UTC caused problems in pattern recognition.

4. Tracking in the target and $B4$

Traveling almost parallel to the target fibers, the incident K^+ deposited significant energy in each fiber (usually >4 MeV) and was in coincidence with the BS. The daughter π^+ traveled nearly perpendicular to the target fibers, and thus left less energy in each fiber (1 MeV on average) and was in coincidence with the t_{rs}. The BS, t_{rs} and fiber times, positions and energies were the key elements to identify the K^+ and π^+ fibers. All the K^+ and π^+ fibers were linked to form a K^+ cluster and a π^+ cluster. A good event should only have one K^+ cluster and one π^+ cluster.

After a UTC track was found, the target pattern recognition routine started to look for the fibers belonging to the K^+ path and the π^+ path separately on a 1 cm wide strip along the UTC track extrapolated into the target. The corresponding energies for K^+ and π^+ (E_K and E_{tg}) and times (t_K and t_π) were calculated from the sum and average in the clusters, respectively. The range of π^+ in the target (R_{tg}) was calculated as the helix traversed by the π^+ from the K^+ decay position to the inner surface of the IC with the polar angle θ correction.

Because of ambiguity in the entry and stopping ends in the pattern of the incoming beam, the target reconstruction routine used the B4 measurement on the K^+ entrance point, which was reconstructed by clustering the hits in the two B4 layers to determine the beam time t_{BM}, the

energy-weighted beam position and the energy loss in B4. The cluster with t_{BM} closest to the t_K was chosen as the one caused by the K^+ beam. A 0.36 cm position precision was obtained by the B4 hodoscope in the $x-y$ plane. With the B4 position measurement, the target reconstruction was repeated to give a better pattern recognition. The K^+ decay vertex in the $x-y$ plane was determined by the K^+ fiber closest to the UTC track but farthest from the K^+ entrance point determined by the B4, while the z position was calculated from the UTC track extrapolation in the $\phi - z$ plane.

Target CCD information improved the pattern recognition and π^+ energy measurement when pileup occurred in a K^+ fiber. When t_K and t_π were separated by more than 2 ns, the CCD pulses in all of the K^+ fibers were studied to identify any hidden π^+ energy.

Isolated hit fibers outside the 1 cm search strip and within the time window of $t_{rs} \pm 5$ ns caused by possible photon(s) or other beam particles were classified into "photon" fibers if their energies were greater than 0.1 MeV.

Once the first round of target reconstruction was finished, the π^+ passage and K^+ decay vertex were determined in the target. The procedure of UTC track fitting was repeated with this additional information. This aided the resolution of the left-right ambiguity in the UTC track reconstruction. Iteration of the target reconstruction was also performed with the improved UTC track.

5. Track passage in the IC

An allowed IC hit pattern was either one or two adjacent sectors per event. The IC provided energy loss (E_{IC}) and time (t_{IC}) measurements. If there was an IC sector crossing, the E_{IC} was from the sum of two IC sectors and the t_{IC} was from the energy-weighted average. It was observed that 1% of tracks had extra hits in the ICs, confounding the measurements of energy and time in ICs. This was resolved by using TD information in addition to the TDC and ADC information. The t_{IC} was always the one closest to the t_{rs} and, the corresponding energy was taken as E_{IC}. The range R_{IC} was computed as the length of the extrapolated UTC track from the inner to the outer IC radius.

6. Tracking in the RS and RSSC

With a charged track reconstructed in UTC and target, the tracking in RS started from the previously found RS cluster. The stopping counter was first analyzed by fitting the TD information with a double pulse assumption to find a $\pi^+ \to \mu^+$ decay signature. This also determined the μ^+ energy (E_μ) from the π^+ decay at rest.

A sector crossing point as illustrated in Fig. 13 was searched for in the RS. A $K^+ \to \pi^+ \nu\bar{\nu}$ candidate should not have more than 2 sector crossings. Precise position measurement in $x-y$ plane was obtained from the sector

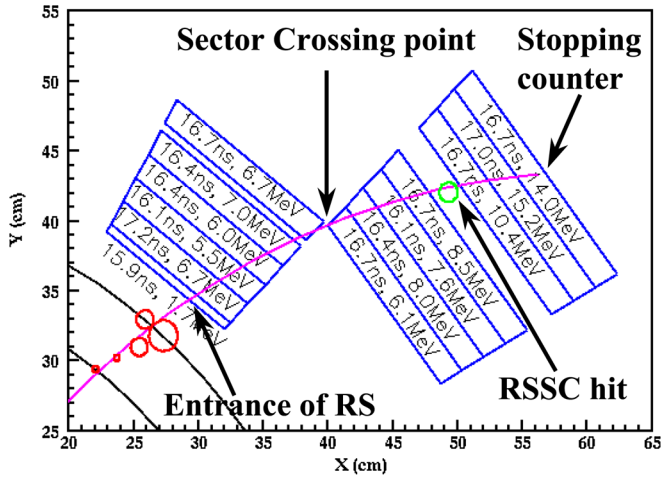

FIG. 13 (color online). Illustration of the range stack track fitting in $x-y$ plane. All the relevant definitions are given in this plot. The arc represents the extrapolation of the fitted UTC track.

crossing points. The z positions were determined by using the end-to-end time differences in the hit counters except the T counter. The average z position resolution was observed to be about 4 to 5 cm.

Another precise position measurement was provided by the RSSCs. All the adjacent hit straw chambers in the RSSC of the hit sector were grouped to form a cluster. The candidate cluster in each sublayer of RSSC was defined as the one closest to a series of arcs drawn from the UTC track extrapolation to the T counter through the sector crossing point(s). The $x-y$ position was obtained from the average of two sublayers in the same RSSC. To minimize the effect of cross talk, the earliest hit in one sublayer was chosen as the true hit. The z measurement was given by the time difference, and the precision was about 1.5 cm.

An RS track fit in the $x-y$ plane used the entrance point provided by the UTC track extrapolation, the sector crossing point(s), the RSSC hit position(s) and the expected path length predicted by the energy losses in the RS layers, taking into account π^+ track propagation with energy loss given by the Bethe-Bloch equation in a 1 T magnetic field. The χ^2 of the fitted track was minimized by changing the incident momentum and the angle at the entrance to the RS (Fig. 13).

The total energy loss of the track in the RS (E_{rs}) was obtained by summing up all the energy losses in the track counters, with E_μ from the fit to pulse shape subtracted from the energy in the stopping counter. The range in the RS (R_{rs}) was calculated from the path length of the fitted track with the polar angle correction. The range in the stopping counter was estimated from the π^+ energy loss.

7. Kinematic measurements of a track

The total range R and energy E of the track were calculated as $R = R_{tg} + R_{IC} + R_{rs}$ and $E = E_{tg} + E_{IC} + E_{rs}$,

respectively. The total momentum P of the charged track was obtained from the UTC with corrections due to energy loss in the target and IC. Since the momentum reduction in both the target and IC were calculated from the range, some correlation between P and R was expected, and thus they should not be treated as uncorrelated in the bifurcation analysis. All of these three kinematic measurements also included tiny contributions from the inactive materials in the UTC. In this analysis, the momentum, energy and range resolutions were measured to be 1.1%, 2.8% and 2.9% (rms), respectively, from a study of $K_{\pi 2}$ events (Table II).

D. Monte Carlo simulation

Detector responses were modeled by a Monte Carlo simulation package, which was developed for the E787 experiment and maintained or improved for E949. The package used several subroutines from the electromagnetic-shower simulation package EGS4 [71] and a number of routines written specially for the experiment, including all of the detector elements, except for the beam instrumentation upstream of the target. Simulation samples were generated with the same format as the data except for omission of the pulse-shape information and most of the beam counter information.

1. Simulation of K^+ propagation

The simulation of K^+ propagation started from a beam file, which contained K^+ events with a list of measured parameters: the K^+ stopping position, the t_K, the number of K^+ fiber hits, the number of accidental fiber hits, the B4 hit position, the stopping target fiber element, the time, energy, fiber element for each K^+ and accidental hit in the target. This file was obtained from an analysis of the stopping distribution of the $K\mu 2$ monitor data. With this beam file and the corrections described in Sec. III D 3, the K^+ propagation had exactly the same target pattern of the data in the simulation. Every K^+ decay started from the stopping fiber at the given K^+ stopping position. The $K\mu 2$ monitor data had sufficient statistics for all the simulation studies in this analysis.

2. Simulation of K^+ decay product

The $K^+ \to \pi^+ \nu \bar{\nu}$ decay was generated with the matrix element of semileptonic $K^+_{\ell 3}$ decay via the V-A interaction, while the $K_{\mu 2}$ decay and the $K_{\pi 2}$ decay were generated via pure phase space. Among the K^+ decay products, photon and electron interactions and their energy deposits were calculated using the routines from EGS4. For charged particles, the energy deposits were calculated by adding the energy losses of each ionization along the steps taken by the particles. The number of ionization and excitation events was determined by dividing the total average energy deposited along the step, obtained using the Bethe-Bloch formula, by the minimum energy that a particle lost in a collision. Multiple Coulomb scatterings of charged particles with various nuclei in the detector were calculated according to the theory of Moliere [72], with corrections for the spin of the scattered particle and the form factor of the nucleus [73]. Hadronic interactions of positively charged π^+'s in the plastic scintillators were calculated using a combination of data and phenomenological models [74]. An option in the simulation package allowed users to turn off nuclear absorption reactions and decays in flight of π^+'s. This was useful in the study of the acceptance.

TABLE II. Comparison of the momentum, range and energy resolutions between data and simulation for the $K_{\pi 2}$ peak.

Experiment	σ_P (MeV/c)	σ_R (cm)	σ_E (MeV)
Data	2.299 ± 0.006	0.866 ± 0.002	2.976 ± 0.005
MC	2.399 ± 0.029	1.018 ± 0.008	3.018 ± 0.025

3. Simulation of trigger

All the trigger conditions were simulated except for the DC, $L1.1$, $L1.2$ and those related to the beam instruments. Since the beam file generated from the $K\mu 2$ monitor data included the trigger bias, a correction was needed to recover the true beam distribution. This was done by introducing a weight function derived from a comparison between simulated $K\mu 2$ triggers and data. In order to get a better precision, perpendicular tracks were used to calculate the $K\mu 2$ trigger acceptance as a function of radial distance of the stopping position in the $x - y$ plane.

4. Comparison between data and simulation

The performance of the Monte Carlo simulation was checked by comparing kinematic resolutions between data and simulation as given in Table II for the $K_{\pi 2}$ decay mode. A 0.15 cm deviation was observed in the range resolution, which is still not understood. This difference could have affected the acceptance estimate and was investigated when performing the acceptance study (see Sec. III H 5). It should also be emphasized that the main role of Monte Carlo simulation in the E949 experiment was to estimate the acceptance factors that could not be obtained from real data (e.g., geometrical and relevant trigger acceptances).

E. Data processing and preselection

Data were stored on the DLT tapes with a total data size of 7 Terabytes. Two steps of data processing ("pass 1" and "pass 2") were taken to reduce and skim the data to a reasonable volume.

1. Pass 1

Pass 1 involved filtering cuts, which consisted of event reconstruction quality cuts and loose μ^+ background re-

jection cuts. Runs with trigger or hardware problems that could not be corrected offline were removed from the data analysis. Tracks were required to be successfully reconstructed, not to stop in those detector elements which had known hardware problems and to have momentum $\leq$ 280 MeV/c.

A $\pi^+ \to \mu^+$ double pulse was required to be found by the fit to the TD pulse in the stopping counter and no extra hits were found in the other 3 sectors associated with the stopping counter TD channel. Since photon activity around the stopping counter could cause confusion in the energy measurement, events with sector crossing in the stopping layer were rejected. Also rejected were the events with a charged track that came to rest in the support materials for the second RSSC layer embedded between the 14th and 15th RS layers. Pass 1 reduced the data volume by a factor of two.

2. Pass 2

Pass 2 involved cuts that were applied to the sample of events surviving pass 1 to skim the data into three categories according to the event features. Each category was uniformly divided into a 1/3 portion and 2/3 portion. Pass 2 consisted of five data skimming criteria: quality of the target reconstruction, loose photon veto, quality of the $\pi^+ \to \mu^+$ double pulse fitting result, single beam K^+ requirement and delayed coincidence cut. These are as discussed below and listed in Table III.

(i) The target reconstruction required that the K^+ decay vertex be inside the target volume, $|t_K - t_{BM}| <$ 4 ns, $|t_\pi - t_{IC}| < 5$ ns and E_{IC} be consistent with that expected from the calculated π^+ range.

(ii) The loose photon veto rejected events for $|t - t_{rs}| <$ 2 ns with an energy in the BV greater than 1.5 MeV, $|t - t_{rs}| < 1.5$ ns with an energy in the EC greater than 3.5 MeV, $|t - t_{rs}| < 1.5$ ns with $E_{RS} >$ 3.0 MeV, or $|t - t_{rs}| < 1$ ns with $E_{tg} > 5.0$ MeV, where t was the time measurement in each photon veto counter.

(iii) The $\pi^+ \to \mu^+$ sequence required a μ^+ decay pulse in the stopping counter and the absence of hits within ± 2.5 ns of the μ^+ time around the stopping counter.

(iv) The beam requirements for signal events were such that the energy loss in the B4 was greater than 1 MeV, the t_{BM} differed from t_{rs} by more than 1.5 ns, and the number of C_π hits was less than 4 with $|t_{C_\pi} - t_{rs}| < 1.5$ ns.

(v) The delayed coincidence required $t_\pi - t_K > 1$ ns.

As defined in Table III, skim 1(4), 2(5) and 3(6) were enhanced in $K_{\pi 2}$, μ^+ and beam backgrounds, respectively, for the 2/3(1/3) portions. These six skims of pass 2 output data facilitated the studies to develop the final selection criteria and evaluate the backgrounds. Signal candidates, if any, remained in the six streams. Study of selection criteria using these samples was always done with at least one cut inverted to ensure that a blind analysis was conducted.

TABLE III. The cuts used in pass 2 for selecting the data streams. Skim 1(4), 2(5) and 3(6) were used for studying the $K_{\pi 2}$, μ^+ and beam background, respectively. See text for more details.

Cuts	Skim 1 & 4	Skim 2 & 5	Skim 3 & 6
Target reconstruction	√	√	√
Photon veto		√	√
$\pi^+ \to \mu^+$ sequence	√		√
Beam K^+ requirement	√	√	
Delayed coincidence		√	

F. Selection criteria of post pass 1 and pass 2

Further selection criteria were designed and applied in order to gain more background reduction. According to their characteristics, the selection criteria were classified into four categories: single beam K^+ selection criteria, kinematic reconstruction, π^+ identification and photon veto. All the cuts were selected to optimize the background rejection and the signal acceptance. Data samples used for this study came from either the 1/3 data (from skim 4 to skim 6) or the monitor trigger events defined in Sec. II H 3, depending on the nature of the selection criteria that were studied.

1. Single beam K^+ requirements

The beam cuts were used to identify beam particles scattering either in the beam instruments or in the target and to ensure a single beam K^+ particle, making full use of time measurements from various subdetectors, energy loss measurements and pattern recognition information in both the B4 and the target as discussed below.

Beam times: The t_{C_K}, t_{C_π}, t_{BW} and t_{BM} cuts were used to reject extra beam particles scattering in the target when one of them agreed with t_{rs} within ± 2 ns. Since the incoming K^+ beam intensity was high discriminator dead time was important and the time measurements used the CCD information in addition to the TDC information from the C_K, C_π and B4 hodoscope. Figure 14 shows the single beam K^+ signal indicated by the $K\mu 2$ monitor and the beam background other than the $K_{\mu 2}$ or $K_{\pi 2}$ peak events rejected in the $\pi\nu\bar{\nu}(1)$ momentum distribution.

Energy loss in B4: The tuning of the energy loss cut in the B4 hodoscope used the acceptance sample from the $K\mu 2$ monitor sample and the rejection sample from the scattered π^+'s in the skim 6 sample. This cut required that the energy loss for an incoming beam particle should be consistent with a K^+ (> 1.1 MeV) as shown in Fig. 15.

Delayed coincidence: The acceptance samples were taken from the $K_{\mu 2}$ peak events in the $K\mu 2$ monitor sample, while the rejection sample was from the scattered π^+'s in the skim 6 sample. As shown in Fig. 16, the distribution of $t_\pi - t_K$ for K^+ decays at rest was an ex-

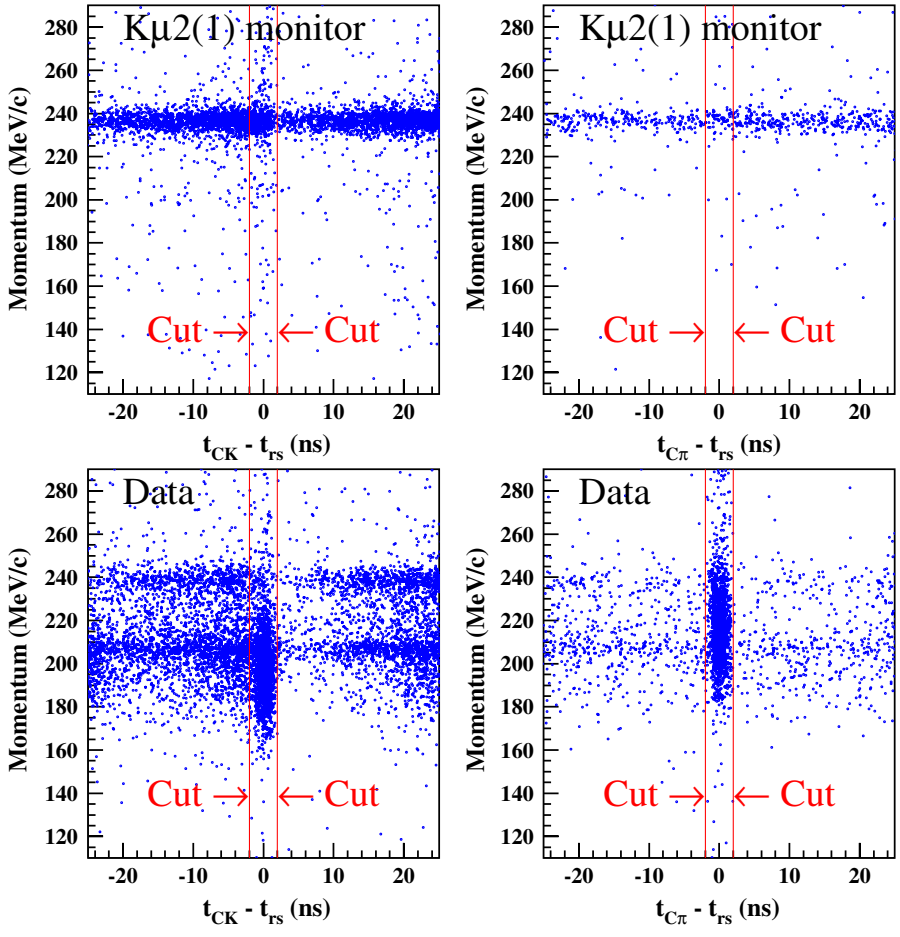

FIG. 14 (color online). The momentum of charged particles versus $t_{C_K} - t_{rs}$ and $t_{C_\pi} - t_{rs}$. The $K\mu 2$ monitor was used to represent the single beam K^+ events. The data plots indicate beam background contamination at beam time (t_{C_K} or t_{C_π}) close to t_{rs} in the $\pi\nu\bar{\nu}(1)$ trigger sample. The arrows indicate the rejected timing regions. The statistics in these plots account for about 0.3% of N_K.

ponential, as expected, consistent with the known K^+ lifetime [18]. The distribution for the scattered π^+'s shows a prompt peak around 0 ns. The delayed coincidence cut required $t_\pi - t_K > 2$ ns. When not all subdetector time measurements were available, the time resolution was degraded; the delayed coincidence cut was adjusted up to 6 ns delay to take into account the resolution. It was expected that this delayed coincidence cut had the same

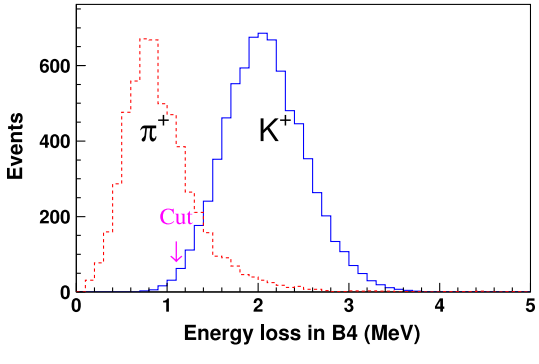

FIG. 15 (color online). The energy loss in the B4 hodoscope for beam K^+ (solid line) and beam π^+ (dashed line). The K^+'s were the $K_{\mu 2}$ peak events in the $K\mu 2$ monitor sample, while the π^+'s were the scattered π^+'s in the skim 6 sample. The arrow indicates the cut position.

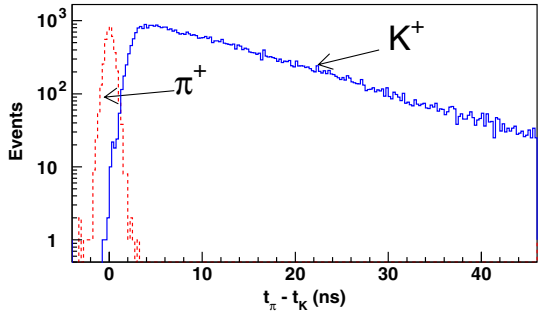

FIG. 16 (color online). Distribution of the time difference, $t_\pi - t_K$ measured by the target, for the $K_{\mu 2}$ peak events (solid line) from the $K\mu 2$ monitor sample and the scattered π^+'s (dashed line) from the skim 6 sample. Beam π^+'s can be assigned a time t_K by the target fiber reconstruction due to misidentification.

rejection power to the background from K^+'s decaying in flight.

Beam likelihood: The K^+ stops in the target were required to have energy loss in the B4 and target consistent with that expected for the measured K^+ stopping position. These conditions helped to eliminate single beam backgrounds with a scattered π^+ which did not have a consistent path length in the target. The three quantities were combined into a likelihood function. Figure 17 shows the likelihood distributions for signal and background using the $K_{\mu 2}$ peak events in the $K\mu 2$ monitor sample and the scattered π^+'s in the skim 6 sample.

Pileup cut: The pulse shape recorded with the target CCDs provided pileup information. The time development of the output signal was fitted with both single- and double-pulse assumptions. If the fitted pulse was more likely to be a double pulse and the time of the second pulse was coincident with the K^+ decay time, the event was rejected.

Pathology cuts: In the target scintillator, charged particles sometimes underwent nuclear interactions or photons had electromagnetic showers. Complicated target patterns could shift background events into the signal region. Some flaws in the selection criteria were identified by inspecting the background events that showed up outside the signal region to be described in Sec. III G 8. Below are the situations addressed by pathology cuts.

(i) Target π^+ cluster with an identified kink. This was an indication of a hard scattering process, which might lead to an incorrect measurement of kinematic quantities.

(ii) In the B4 the measured energies derived from the ADC and CCD were required to be consistent within 1.5 MeV and the measured times derived from the TDC and CCD were required to be consistent within 2 ns. Inconsistency in either the times or energies was likely due to a second beam particle.

(iii) Target π^+ fiber next to the decay vertex with energy greater than 3.5 MeV. This might indicate a K^+ fiber being misidentified as a π^+ fiber, causing an incorrect measurement of kinematic quantities.

(iv) Target π^+ fiber with energy greater than 5 MeV. This might imply a $K_{\pi 2}$ or a radiative $K_{\mu 2}$ event with a photon hiding in the π^+ fiber.

(v) If a target edge fiber was identified as a K^+ fiber with a time within 3 ns of the nearby IC, the event was rejected. This feature was often an indication of a double beam background.

(vi) Target fibers on the opposite side of the π^+ track with respect to the vertex having energy greater than 2 MeV within ± 3.0 ns of t_π. This usually indicated a $K_{\pi 2}$ event with a photon conversion opposite to the π^+.

(vii) Target π^+ track on the opposite side of the π^+ track with respect to the K^+ decay vertex. This usually indicated a double beam or a cosmic ray background in addition to the first K^+ beam particle.

(viii) Target edge fiber greater than 5 MeV within ± 4 ns of t_{rs}. This suggested some photon activity in the edge fibers, or a double beam event with the second beam hiding in the track.

(ix) Any activity found in either the UPV or RV within ± 4 ns of t_{rs}.

Most pathology cuts were related to target pattern recognition. These backgrounds could not be tagged with the usual procedure of background analysis until the outside-the-box study given in III G 8.

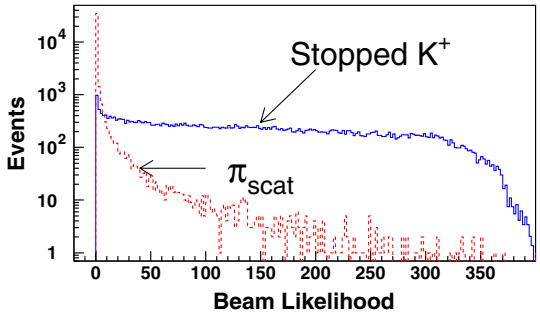

FIG. 17 (color online). Beam likelihood for K^+ decays at rest (solid line) from the $K\mu 2$ monitor sample and scattered π^+'s (dashed line) from the skim 6 sample. The energy loss of K^+ in the target was required to be greater than 25 MeV and the number of K^+ fibers was required to be greater than 2 before evaluating the beam likelihood.

2. Decay π^+ kinematic requirements

Once the π^+ kinematic reconstruction routines produced the range-, energy- and momentum-related quantities, cuts on the kinematic values (referred to as KIN cuts), were identified and divided into several subgroups which are described below.

Fiducial cuts: The π^+ stopping layer was required to be RS layers 11–18. No charged track was allowed to stop in the RSSC layer embedded between the 14th and the 15th RS layer. Events were also rejected if the stopping layer was 14 with an RSSC hit found in the same RS sector or one sector clockwise of the stopping counter. The cosine of the polar angle for a charged track was required to be within ± 0.5. The z position from the UTC track extrapolation to each RS layer was required to be as narrow as ± 30 cm to reject $K_{\mu 2}$ backgrounds with longer path lengths in RS. The effective UTC fiducial volume was defined to be $|z| < 25$ cm at the UTC outermost layer.

Signal phase space: The phase space cuts required that the momentum, kinetic energy and range of a π^+ track should be in $211 \leq P \leq 229$ MeV/c, $115 \leq E \leq 135$ MeV, and $33 \leq R \leq 40$ cm. As the resolution of kinematic quantities depended on the azimuthal and polar angles of the π^+ track, the lower limits of the phase space region were further defined by the requirements (referred to as $K_{\pi 2}$ kinematic cuts) that $\mathrm{Pdev} = \Delta P/\sigma_P \geq 2.5$,

$\text{Edev} = \Delta E/\sigma_E \geq 2.5$, and $\text{Rdev} = \Delta R/\sigma_R \geq 2.75$ where the ΔP, ΔE and ΔR were the deviation from the $K_{\pi 2}$ kinematic peak positions, and σ_P, σ_E and σ_R were the corresponding resolutions, which were correlated with the azimuthal and polar angles.

Tracking quality in target: Good target tracking relied upon a consistent pattern of hits in the target. This required the nearest target K^+ fiber of the track to the B4 hit position to be no more than 2 cm away. The K^+ decay vertex was required to be nearest to the extreme tip of the K^+ cluster. No more than one fiber gap was allowed between the K^+ decay vertex and the closest π^+ fiber. A target track could include either π^+ fibers with photons or photon fibers misidentified as the π^+ fibers, leading to an incorrect energy measurement or event classification if the photon veto also failed. The π^+ fibers were therefore examined using likelihoods based on the comparisons of the time, energy, and distance to the track between those values expected from the simulated $K^+ \to \pi^+ \nu \bar{\nu}$ sample and the measured values from the $K\pi 2(1)$ monitor events.

Tracking quality in UTC and RS: At least 4 hits out of 6 cathode foils were required to ensure a good measurement of a track in the UTC. Further quality checks were developed with respect to the $K_{\mu 2}$ momentum peak, taking account of all the possible circumstances that could lead to an incorrect momentum measurement, such as no hit in the outermost foil layer, less than 12 layers of anode wire hits, overlapping tracks, or too many wire hits in a cluster being excluded from the fit. The cuts were adjusted so that the momentum resolution effect did not give a significant contribution to the $K_{\pi 2}$ and μ^+ background estimates (Sec. III G). Another good way to ensure a good UTC measurement was to require consistency among UTC, RS and RSSCs. In the $x - y$ plane, this could be achieved by requiring consistency between the UTC extrapolation and the positions of the sector crossing and the RSSC hits. Similarly, in the $\phi - z$ plane consistency was required between the UTC extrapolation and the z positions measured by RSSC and RS. To establish these requirements, the μ^+'s in skim 5 were selected with all the other cuts applied, except that the maximum momentum cut was not applied and the $\pi^+ \to \mu^+ \to e^+$ decay sequence cuts (see Sec. III F 3) were inverted, and the π^+'s in skim 6 were selected with all the cuts applied, except that the cuts on single beam K^+ were inverted (Sec. III F 1). These signal and background samples were also used in the relevant studies of energy loss in the RS and range-momentum consistency in UTC and RS.

Energy loss in RS: It was noted that a μ^+ from the $K_{\mu 2}$ might fake a π^+ due to scattering. In addition a π^+ from the $K_{\pi 2}$ might fake a signal due to either a photon or an accidental hit being hidden in the track counters. The resulting background was removed by comparing the energy measurement in each RS layer with the expected value from the range. The energy deviation was required

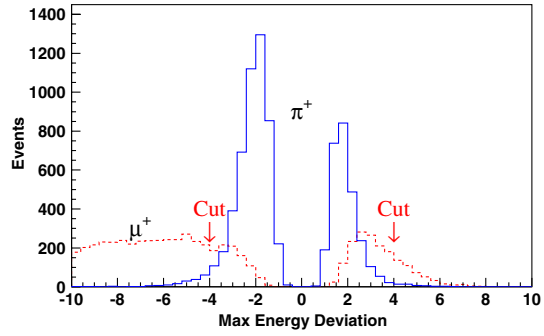

FIG. 18 (color online). Distributions of the maximum energy deviation for π^+'s (solid line) and μ^+'s (dashed line) in RS. The cut positions are indicated by the arrows.

to be within $\pm 4\sigma$ for each RS counter as shown in Fig. 18. In addition to each layer, a probability for energy loss consistency was also calculated with all track counters except for the T counter, the stopping counter and the counters with sector crossings. As shown in Fig. 19, the probability cut provided good separation between π^+'s and μ^+'s. Another way to reject the μ^+ background was to calculate the likelihood from the ratio of the expected (E^i_{expt}) and measured (E^i_{meas}) energy of a track in the ith layer, $\Delta E \equiv \log E^i_{\text{expt}} - \log E^i_{\text{meas}}$, taking into account the Landau tail of the expected energy distribution. This calculation was done up to and including the layer prior to the stopping layer. Figure 20 shows good π/μ separation using the calculated likelihood value. It was noted that this cut on the likelihood was correlated with the cuts on the energy deviation and the probability given above.

Range-energy consistency in IC and target: Despite the poor resolution of energy measurements in the IC and target, they could still provide a certain level of particle identification in addition to that from the RS. Signal and background samples used in this study were from the $K\pi 2(1)$ and $K\mu 2$ monitors. The difference between the E_{IC} and the expected value from R_{IC} was required to be between -5 to 1.75 MeV. The target range (R_{tg}) in cm and

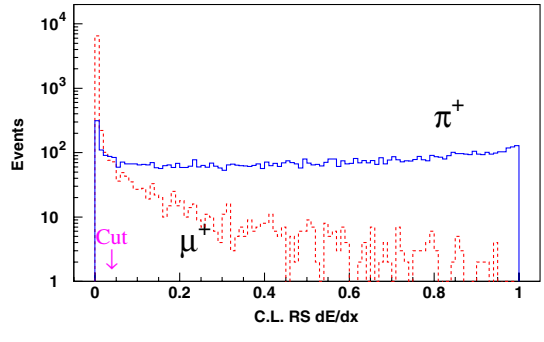

FIG. 19 (color online). Distributions of the probability of energy loss consistency in the RS dE/dx measurement for π^+'s (solid line) and μ^+'s (dashed line). The arrow indicates the cut position.

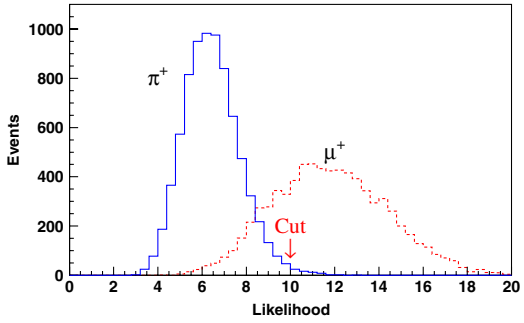

FIG. 20 (color online). Likelihood distributions of the RS energy measurement for π^+'s (solid line) and μ^+'s (dashed line). The arrow indicates the cut position.

energy (E_{tg}) in MeV were used to cut events in which $R_{tg} > 12$ cm, $E_{tg} > 28$ MeV, $9.5 \times E_{tg} > 28 \times R_{tg}$ or $10 \times E_{tg} < 21.5 \times (R_{tg} - 2)$ to reject background with a photon hiding along the π^+ track in the target.

Range-momentum consistency in UTC and RS: This cut was used to check whether the range of the charged track was consistent with that for a π^+. The range deviation in RS was defined as $\chi_{rm} = (R_{rs} - R_{utc})/\sigma_R$, where R_{utc} was the expected range calculated from the momentum measured by the UTC with a π^+ hypothesis, and σ_R was the uncertainty of the measured range as a function of the momentum. The μ^+'s and π^+'s were selected from skim 5 and skim 6 samples, respectively, as used in the study of energy loss in the RS, except that the maximum momentum requirement was also applied in skim 5 to remove the $K_{\mu 2}$ range tail events. The distributions of the range deviation for π^+'s and μ^+'s were shown in Fig. 21. Good π/μ separation was observed.

3. $\pi^+ \to \mu^+ \to e^+$ decay sequence

All cuts for identifying the $\pi^+ \to \mu^+ \to e^+$ decay sequence were put into a special group (referred to as TD cuts). The TD information recorded the pulse shape, providing a tool to recognize the decay sequence. As can be seen below, the TD cuts were independent of the kinematic reconstruction and photon veto and could be used in the bifurcation study. The signature for this decay sequence was

(i) Three energy deposits (pulses) corresponding to the π^+ kinetic energy, $\pi^+ \to \mu^+\nu_\mu$ and $\mu^+ \to e^+\nu_e\bar{\nu}_\mu$ decays were found in the stopping counter.

(ii) The kinetic energy of the μ^+ from $\pi^+ \to \mu^+\nu_\mu$ decay was 4.1 MeV, but due to saturation the observed energy was about 3 MeV [75]. Since the path length of the μ^+ was ~1.4 mm in RS, the fraction of μ^+ exited the stopping counter without depositing more than 1 MeV was only ~1% of π^+ decays.

(iii) The e^+ from $\mu^+ \to e^+\nu_e\bar{\nu}_\mu$ decay has a kinetic energy of $E_e < 53$ MeV. Most of the e^+'s exited the stopping counter and deposited energy in the other RS counters.

The three energy deposits from the $\pi^+ \to \mu^+ \to e^+$ decay sequence should be observed by the TDs at both ends of the stopping counter.

For the μ^+ background, only two pulses due to muon kinetic energy and decay would be produced. A μ^+ could fake a π^+ when an extra pulse was detected in addition to the expected two pulses. To suppress the μ^+ background, two stages of cuts were imposed.

At the first stage evidence for the $\pi^+ \to \mu^+\nu_\mu$ decay was sought. The pulse development in the stopping counter as recorded by the TDs was fitted with a single- and double-pulse hypothesis in an interval of ~4 π^+ lifetimes (typically 104 ns). The template shapes used in the fit were derived from the average of measured pulses from μ^+ traversal for each end of each RS counter. In addition, a correction was applied to the template shape to take into account the change in shape due to propagation along the counter. The parameters of the single-pulse fit were the time, the total area of the pulse and a constant corresponding to a pedestal of typically 3 TD counts. The parameters of the double-pulse fit were the time of the first pulse, the time difference of the two pulses, the total pulse area, the fractional area of the second pulse and the pedestal. A fit to a triple-pulse hypothesis was attempted if evidence for a third pulse was found based on a rudimentary analysis of

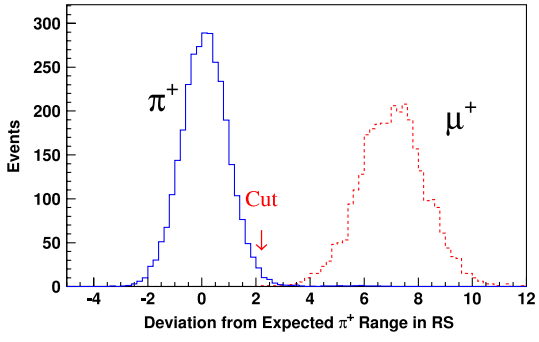

FIG. 21 (color online). Distributions of the range deviation in the RS for π^+'s (solid line) μ^+'s (dashed line) tracks. The arrow indicates the cut position.

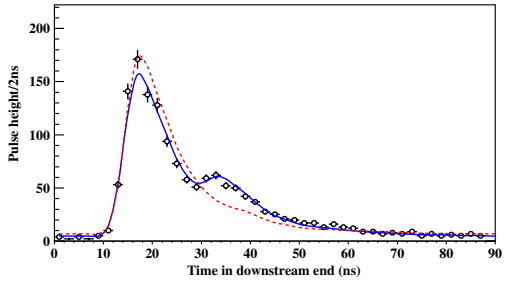

FIG. 22 (color online). Results of fits with the single- and double-pulse hypotheses to the TD pulse shapes in the stopping counter. The solid curve is for the double-pulse hypothesis and the dashed curve is for the single-pulse hypothesis.

the TD information or if evidence for the $\pi^+ \to \mu^+ \nu_\mu$ decay from the double-pulse fit was lacking. The two additional parameters in the fit were the time difference of the third pulse with respect to the first and the fractional area of the third pulse. The results of the single- and double-pulse fit hypotheses for $\pi^+ \to \mu^+ \nu_\mu$ decay were shown in Fig. 22. Loose requirements were first applied on the observed μ^+ energy $1 < E_\mu < 14$ MeV and on the relative quality of the results of the single- and double-pulse fits, $R(1) > 1$ or $R(2) > 2$, and $R(1) \times R(2) > 1$ where the quantities are defined in Table IV.

At the second stage, five cuts listed in Table V were then applied to suppress the following four mechanisms when a $\mu^+ \to e^+$ decay could fake the three-pulse $\pi^+ \to \mu^+ \to e^+$ decay sequence.

(i) π^+ time accidental: Accidental activity produced the first pulse, while the $\mu^+ \to e^+$ decay gave the second and third pulses in the timing sequence.

(ii) Early μ^+ decay: The $\mu^+ \to e^+$ decay occurred at an early time (≤ 100 ns), producing the second pulse, and accidental activity was identified as the third pulse.

(iii) μ^+ time accidental: The $\mu^+ \to e^+$ decay made the third pulse, while the second pulse was produced by accidental activity occurring between the μ^+ stop and decay.

(iv) Tail fluctuation: A fluctuation in the falling edge of the first pulse was identified as the second pulse. The decay positron from the μ^+ decay made the third pulse.

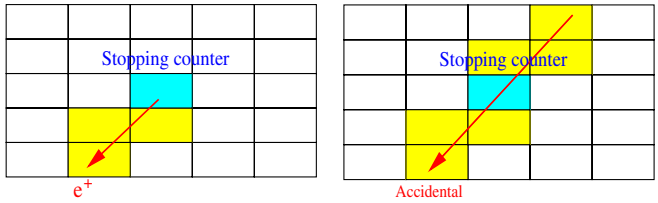

FIG. 23 (color online). Schematic view of signal (left) and background (right) of the $\mu^+ \to e^+$ decay. Each rectangle represents an RS counter. The central counter represents the stopping counter and the shaded rectangles represent hit counters. The arrow indicates the possible direction of the positron or charged track producing the hits.

π^+ time consistency cut: This cut suppressed the π^+ time accidental background. When accidental activity made the first pulse and a charged track made the second pulse in the stopping counter, the timing of the first pulse obtained by the TD ($t_{\pi,TD}$) was not coincident with t_{RS} obtained from the other RS counters along the track. Events were rejected if $|t_{\pi,TD} - t_{RS}| > 2.5$ ns.

$\mu^+ \to e^+$ decay requirement: The positron from the $\mu^+ \to e^+$ decay (the third pulse) generally deposited energy in the stopping counter and other neighboring counters as depicted in Fig. 23. The positron finding started by looking for a cluster of TDC hits in the RS counters in the region within ± 1 sector and ± 2 layers of the stopping counter. The cluster should include the stopping counter and an additional hit in the same sector as the stopping counter. Candidates for the positron were found when the average time of the hits in the cluster was within ± 2.4 ns

TABLE IV. Definitions of quantities determined by the pulse fitting in the stopping counter. The z positions were determined from the energy ratio between the two ends of the stopping counter. The z position of the nominal π and μ pulse was z_π or z_μ, respectively. The term "second" pulse identifies the μ^+-candidate pulse. The neural net is described in the second stage of cuts.

Quantity	Definition or use
E_μ	Energy of the second pulse
T_μ	Time of the second pulse
$\chi^2_n(i)$	χ^2 for the n-pulse hypothesis for the counter end i ($i = 1, 2 =$ upstream, downstream)
$R(i)$	$\chi^2_1(i)/\chi^2_2(i)$
$\log_{10}(R(1) \cdot R(2))$	Neural net input
$\log_{10}(\chi^2_1(1) \cdot \chi^2_1(2))$	Neural net input
dz	$= z_\pi - z_\mu$, neural net input component
dt	Time difference between both counter ends for the second pulse, neural net input

TABLE V. List of the backgrounds targeted by $\pi^+ \to \mu^+ \to e^+$ decay sequence cuts.

Cut	π^+ time accidental	Early μ^+ decay	μ^+ time accidental	Tail fluctuation
π^+ time consistency cut	√			
$\mu^+ \to e^+$ decay requirement		√		
Cut on μ^+ time accidental			√	
Cut on μ^+ time accidental in the track counters			√	
Neural net $\pi^+ \to \mu^+$ decay cut			√	√

of the TDC time (the third pulse) in the stopping counter. The z positions of the hits in the cluster, obtained from the end-to-end time differences of the hits, were also required to be consistent with the z position in the stopping counter. If the candidate was due to a track that passed through the stopping counter, then hits might be found on both sides of the stopping counter (Fig. 23). The early μ^+ decay background was removed by requiring that the second pulse from the TD pulse fitting agreed with the time of the cluster.

Cut on accidental activity: Accidental activity in the stopping counter was frequently associated with activity in other RS counters as well as the BV, BVL and EC. Hence, events with activity coincident with the second pulse in the stopping counter were targeted for rejection. The time windows and energy thresholds for the various subsystems in RS, BV, BVL and EC were optimized in order to have the highest rejection power at a given acceptance value of 94% for this cut. Events were rejected if the energy sum of the hits within a time window in any of the subsystems was greater than the threshold. There was also a kind of accidental activity that overlapped the charged track and made a second pulse in the stopping counter. To reject this accidental background, fits were performed to a double-pulse hypothesis in the two RS counters along the track prior to the stopping counter. If the time of the fitted second pulse was within ± 5 ns of the second pulse in the stopping counter, the fitted energy of the second pulse was greater than 1 MeV and the χ^2 ratios of the single- to the double-pulse fit hypotheses were greater than 4, then the event was rejected.

Neural net $\pi^+ \to \mu^+$ decay cut: The tail fluctuation background mimicking the energy deposit for a μ^+ at the falling edge of the π^+-induced pulse was characterized by a small decay time and a low pulse area in the second pulse. The variables shown in Fig. 24 and described in Table IV differed for events induced by $\pi^+ \to \mu^+\nu_\mu$ and $\mu^+ \to e^+\nu_e\bar{\nu}_\mu$ decays. Application of a fixed cut to each variable would cause a non-negligible acceptance loss. In order to achieve a higher acceptance at the same rejection as the fixed cuts, a neural network (NN) technique was adopted. The NN function was derived via a multilayer perception program incorporated in the library of Physics Analysis Workstation (PAW) [76]. To create the NN function, the scattered π^+'s and $K_{\mu 2}$ range tail events in the $\pi\nu\bar{\nu}(1)$ trigger, which passed all other $\pi^+ \to \mu^+ \to e^+$

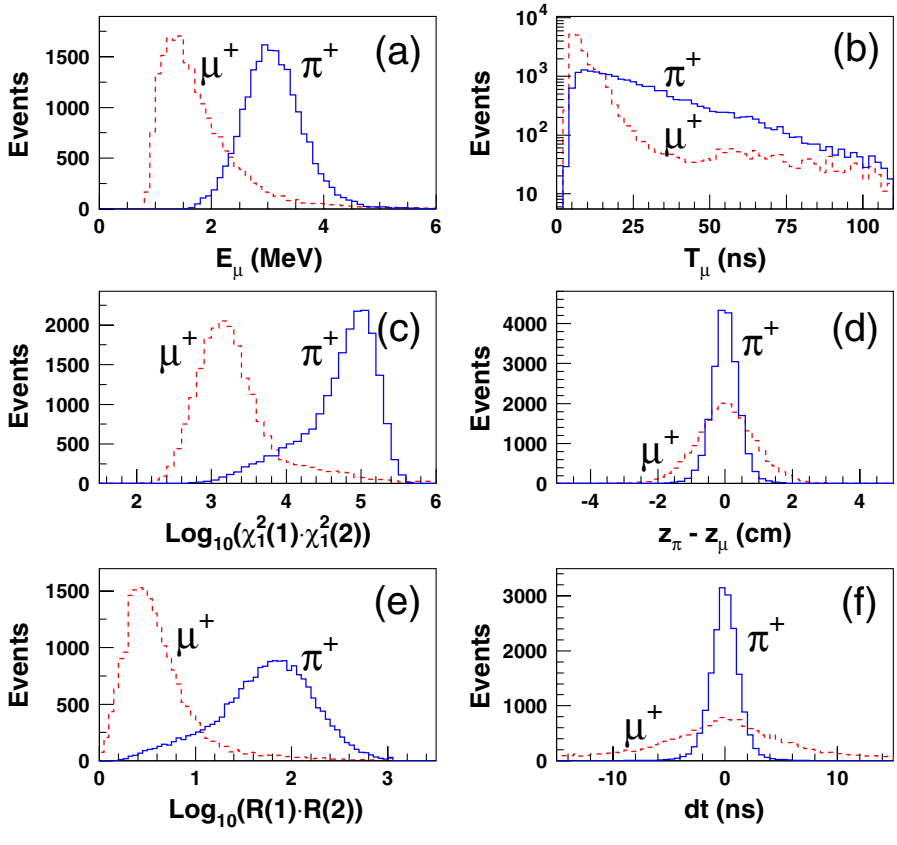

FIG. 24 (color online). Distributions of the input variables for the neural net function in $\pi^+ \to \mu^+\nu_\mu$ induced (solid lines) and $\mu^+ \to e^+\nu_e\bar{\nu}_\mu$ induced (dashed lines) decays. The energy of the second pulse (a), time of the second pulse (b), log of the product of the single-pulse fit χ^2's for both ends (c), z position difference between the first and second pulses obtained from the energy ratio of both ends (d), log of the product of the χ^2 ratios of single- to double-pulse fits for both ends (e) and time difference of the second pulses in both ends (f).

decay sequence cuts, were used as signal and background samples, respectively. A 5-variable NN function was obtained using the six variables shown in Fig. 24 with the differences in z position and time combined to create a single input variable,

$$\chi^2(z,t) \equiv (dz/\sigma_{dz})^2 + (dt/\sigma_{dt})^2, \tag{24}$$

where the z position and the time were obtained from the energy ratio of both ends, and time difference of the second pulses in both ends. The resolution of dz (dt) was σ_{dz} (σ_{dt}). Figure 25 shows the distributions of the output of the NN function for π^+'s and μ^+'s. The rejection of the NN $\pi^+ \to \mu^+$ decay cut as a function of the acceptance is shown in Fig. 26

4. Photon veto

To achieve the background level much less than one event, the total π^0 rejection was required to be of order of 10^6. A rejection factor of $\sim 10^4$ was already achieved online, leaving a further $\sim 10^2$ rejection factor to be achieved by the offline analysis. The corresponding photon veto cuts (referred to as PV cuts) were used to identify the photon activities detected by all the PV counters.

A search for the photons coincident with the track time was performed in the subsystems of the BV, BVL, RS, EC, target, IC, VC, CO and μCO. The timing resolution of each photon detection system was a key ingredient in determining the time window for the PV due to the false veto rate in the high rate experimental environment. Figure 27 shows the measurements of the timing resolution for each system as a function of the visible energy. Since the EC consisted of 4 rings and the inner ring (ring1) was exposed to high accidental rates from the beam, the corresponding time resolution was worse. The time window and energy thresholds in each subsystem were optimized by

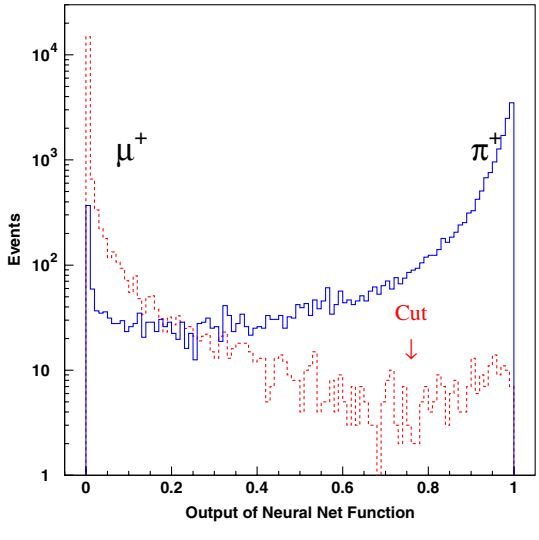

FIG. 25 (color online). Distributions of the outputs of the NN function for π^+ (solid line) and μ^+ (dashed line) events. Events with an output of the NN function less than 0.76 were rejected.

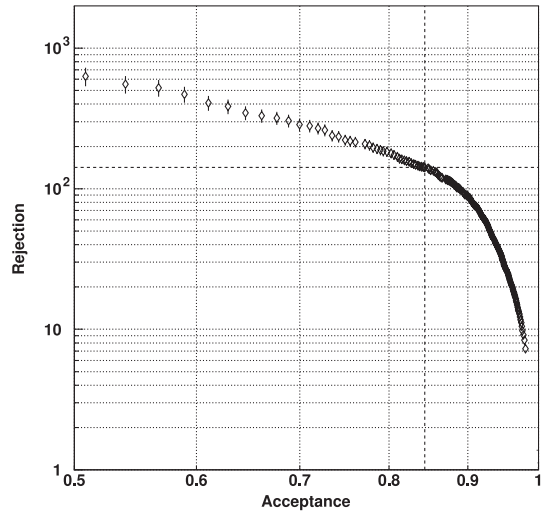

FIG. 26. Rejection of the NN $\pi^+ \to \mu^+$ decay cut as a function of the acceptance. The intersection of the vertical and horizontal dashed lines shows the rejection and acceptance at the nominal cut position.

adjusting the cut positions to maximize rejection for a given acceptance. The rejection sample was from skim 4 with $K_{\pi 2}$ events, while the acceptance sample was from the $K\mu 2$ monitor. To ensure the events were from the $K_{\pi 2}$ peak, the measured range, energy and momentum of the charged track were required to be within three standard deviations of the nominal values. For the $K_{\mu 2}$, the momentum of the charged track was required to be within three standard deviations of the nominal value, and the range was required to be longer than 37 cm to remove any event which could contain photon(s). The selected $K_{\pi 2}$ and $K_{\mu 2}$ events were also required to pass the KIN cuts and the beam cuts.

The optimization process [77] started from the initial set of cut parameters. For a new set of parameters, the rejection and acceptance were remeasured. Only one subsystem's cut parameters were varied at a time. If the rejection increased without losing acceptance or the acceptance increased without losing rejection, the set of parameters was regarded as a good input for the iteration. More preferable cases occurred when both the rejection and acceptance were improved. Figure 28 illustrates this optimization process for the photon veto. The optimization process continued until no more gain was obtained in rejection without losing acceptance. The boundary point was measured at every given acceptance position. As a result, a profile curve, which gave the maximum achievable rejection, was obtained.

Figure 29 shows the offline rejection of the photon veto cuts against the $K_{\pi 2}$ background as a function of acceptance. The time window and energy threshold for each category are tabulated in Table VI. As a reminder, the total offline photon veto is not the simple product of the rejections listed in Table VI due to mutual correlations.

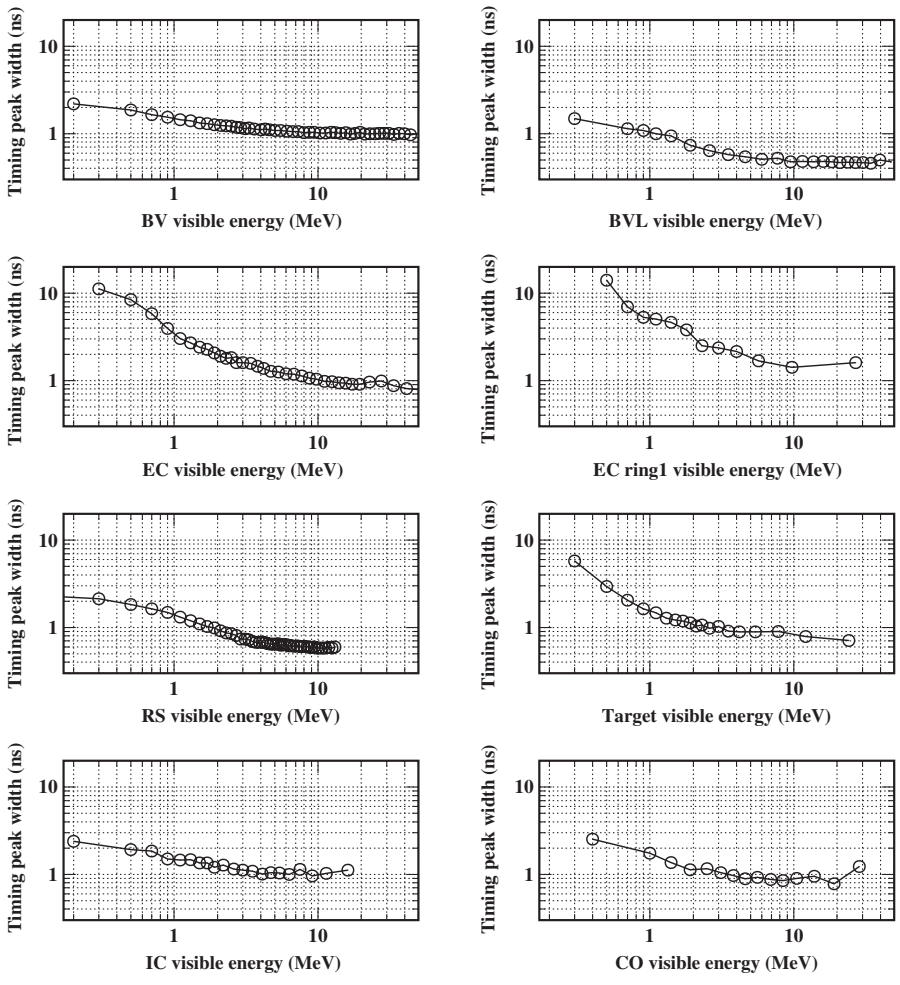

FIG. 27. The timing resolution as a function of visible energy in various PV counters.

G. Background evaluation

To have an unbiased result, the signal region was always masked until all the background evaluation studies were completed. As described in Sec. III A, the stopped K^+ decay background and the beam background were subdivided into the following categories:

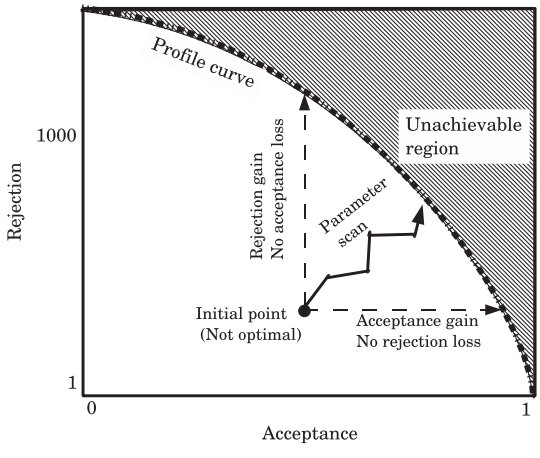

FIG. 28. Illustration of the optimization process to determine the photon veto parameters.

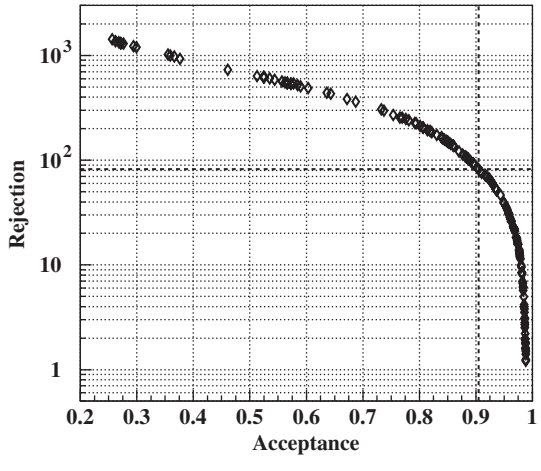

FIG. 29. Offline rejection of the photon veto cuts against the $K_{\pi 2}$ background as a function of the acceptance. The crossing point of the vertical and horizontal lines shows the rejection and acceptance at the cut position.

TABLE VI. Time window and offline energy threshold for each category of the photon veto cuts. Also listed are individual rejection values contributed by each subsystem.

Category	Time window (ns)	Energy threshold (MeV)	Rejection
BV	±4.50	0.20	14.556
BVL	±2.00	0.00	1.247
RS	±1.50	3.80	3.329
EC	±2.25	3.80	2.296
Inner EC	±1.75	1.00	1.186
Target	±1.30	4.79	1.493
IC	±2.25	0.40	1.321
VC	±2.00	1.60	1.054
CO	±1.25	0.80	1.052
μCO	±1.50	2.80	1.003

(i) $K_{\pi 2}$ background,
(ii) $K_{\mu 2}$ range tail background,
(iii) μ^+ band backgrounds,
(iv) single beam background,
(v) double beam $K^+ - K^+$ background,
(vi) double beam $K^+ - \pi^+$ background, and
(vii) CEX background.

Except for CEX, all background levels were estimated using the data by means of the bifurcation method. Table VII gives the bifurcation cuts, the data stream categories and the results for the 1/3 data sample. The background levels given in Table VII must be scaled by a factor of 3 to obtain estimates for the full sample. The 1/3 sample was studied first in order to tune and optimize the cuts. Then the 2/3 sample was used to give the final background estimates. When the normalization branch contained only one or few events in region B, a second bifurcation analysis was performed in this branch to improve the statistics. Details of these procedures are given in the following sections.

1. $K_{\pi 2}$ background

A $K_{\pi 2}$ decay event should have a charged track with a monochromatic momentum, range and energy plus two photons. Experimentally, if a $K_{\pi 2}$ event appeared in the signal region, the photons from the π^0 decay must have escaped detection and the $K_{\pi 2}$ kinematics must have been distorted by scattering or resolution effects as well.

In the background study, the two bifurcation cuts were chosen as the PV cuts (CUT1) and the signal phase space cuts in the KIN cuts (CUT2), since both of these could independently give powerful rejection of the $K_{\pi 2}$ background. In order to remove the contamination from μ^+ and beam events, the bifurcation analysis sample was selected from the skim 4 sample by applying the TD cuts, the beam cuts and the KIN cuts other than the phase space cuts. In the rejection branch, $K_{\pi 2}$ events were selected by inverting the signal phase space cut in the KIN cuts ($\overline{\text{CUT2}}$), giving 95 797 events for the region C + D. The PV cuts (CUT1) were then applied to the remaining $K_{\pi 2}$ events, leaving 1124 events for the region C. In the normalization branch, the $K_{\pi 2}$ events with photon activity were selected by inverting the PV cut ($\overline{\text{CUT1}}$). The signal phase space cuts in the KIN cuts (CUT2) were applied to the above selected $K_{\pi 2}$ sample, resulting in no events ($B = 0$) left in the normalization branch.

To deal with the above situation and give nonzero events in the normalization branch, another (second) bifurcation analysis was performed by separating the $K_{\pi 2}$ kinematic cuts into Edev (CUT1) and Rdev + Pdev cuts (CUT2), since the E measurement was almost independent of R and P measurements. These two bifurcation cuts were applied sequentially to the selected $K_{\pi 2}$ sample in the normalization branch. In this second bifurcation study, the lower boundary cuts on E, R and R were removed. Changing the cut positions on the Rdev, Pdev and Edev gave the number of events in the normalization branch (N_{RP}) and the rejection branch (R_E) in the second bifurcation analysis, which were then used to calculate the expected number of events in the normalization branch by means of $B = N_{RP}/(R_E - 1)$. This second bifurcation method gave smaller uncertainty, providing a way to optimize the phase space cut positions to reject the $K_{\pi 2}$ background with less acceptance loss. The expected number of events from the second bifurcation analysis was found to be ~10% less than the observed number from the first bifurcation analysis in the region B + D. This was due to the small level of correlation between R and E when

TABLE VII. Results of the bifurcation analyses for the backgrounds in the 1/3 sample only. All the results for the region B were from the second bifurcations except for the single-beam background as explained in the text. Details for CUT1 and CUT2 are described in the text. Errors are statistical only.

Bkg.	CUT1	CUT2	Category	B	$(C+D)/C$	BC/D
$K_{\pi 2}$	PV	KIN	Skim 4	0.39 ± 0.11	85.2 ± 2.5	0.0046 ± 0.0013
$K_{\mu 2}$	TD	KIN	Skim 5	1.81 ± 0.16	$(4 \pm 1) \times 10^2$	0.0041 ± 0.0011
μ^+ band	TD	KIN	Skim 5	2.37 ± 0.74	$(4 \pm 1) \times 10^2$	0.0053 ± 0.0021
Single beam	DC	B4	Skim 6	8	$(7 \pm 4) \times 10^3$	0.0011 ± 0.0007
Beam $K^+ - K^+$	BWPC	B4	Skim 6	0.04 ± 0.04	117 ± 37	0.0003 ± 0.0003
Beam $K^+ - \pi^+$	BWPC	B4	Skim 6	0.26 ± 0.11	$(7 \pm 4) \times 10^3$	<0.0001

estimating the π^+ range in the stopping layer from the measured energy in the stopping layer. The cut positions were chosen at Rdev > 2.75, Edev > 2.5 and Pdev > 2.5, in order to reduce the expected $K_{\pi 2}$ background level to about 0.01 events level as shown in Table VII. Figure 30 shows the expected $K_{\pi 2}$ background from the second bifurcation in the $1/3$ normalization branch as a function of the Edev cut position. The acceptance was measured using the simulated $K^+ \to \pi^+ \nu\bar{\nu}$ sample.

The expected number of events from the second bifurcation was used to give the result for the normalization branch, which was then used to give the estimated background level for the $1/3$ sample as shown in Table VII.

2. μ^+ background

The μ^+ background consisted of the $K_{\mu 2}$ range tail events and the μ^+ band events as indicated in Fig. 8. These μ^+'s lost energy and eventually came to rest in RS and could migrate into the signal region through resolution effects if the TD cuts failed.

The two bifurcation cuts with the most powerful rejection were the TD cuts (CUT1) and the selected KIN cuts (CUT2), which excluded the fiducial cuts, the lower boundary in the signal phase space cuts, the cuts on the tracking quality in target and the cuts on the range-energy consistency in IC and target as detailed in Sec. III F 2. The μ^+ background sample used for the bifurcation study was

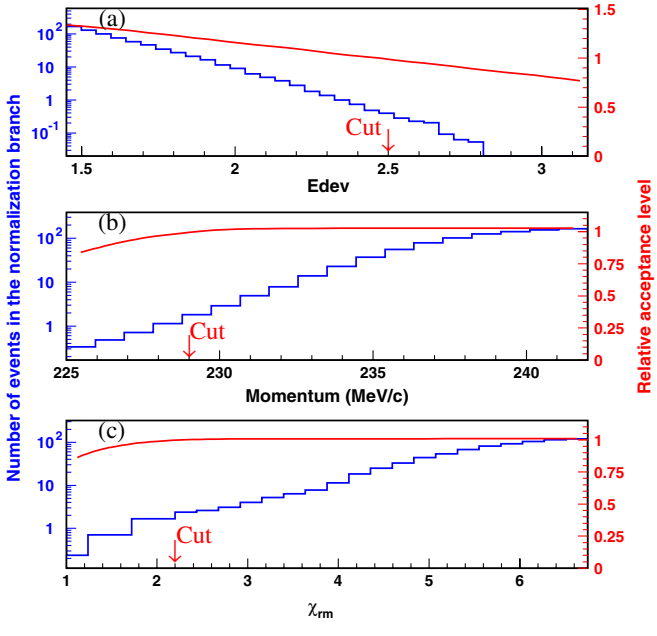

FIG. 30 (color online). The expected kinematic background events in the $1/3$ normalization branch (histogram with left axis) as a function of $K_{\pi 2}$ kinematic cut (Edev) position for the $K_{\pi 2}$ background (a), maximum momentum cut position for the $K_{\mu 2}$ range tail background (b) and range-momentum cut (χ_{rm}) position for the μ^+ band background (c). Also shown is the relative acceptance change as the cuts (curve with right axis).

selected from the skim 5 sample by applying the PV cuts, the beam cuts and the KIN cuts not used in this bifurcation study, in order to remove the $K_{\pi 2}$ and beam backgrounds. In the rejection branch, there were 7119 μ^+ events in the region C + D when inverting the selected KIN cuts ($\overline{\text{CUT2}}$). The TD cuts (CUT1) were applied to the μ^+ events, leaving 16 events in the region C. In the normalization branch, the μ^+ events were obtained by inverting the TD cuts ($\overline{\text{CUT1}}$). The selected KIN cuts (CUT2) were applied to the above selected μ^+ sample, leaving only one event ($B = 1$) in the normalization branch.

The result from the bifurcation analysis given above had a large statistical uncertainty, since only one event remained in the normalization branch. The $K_{\mu 2}$ range tail and the μ^+ band events were the only two possible μ^+ backgrounds in the signal region. The origins of these two backgrounds were due to the momentum and range resolution effects. Once these resolution effects were known in the signal region, a better estimate of corresponding events B in the normalization branch could be obtained. In this analysis, the events with $P > 225$ MeV/c were regarded as the $K_{\mu 2}$ range tail background.

The momentum resolution effects could be well described by using the momentum distribution from the $K_{\mu 2}$ peak events. In order to enhance the number of events in the normalization branch, the RS energy loss cuts were removed from the KIN cuts. Also removed were the upper boundary cuts on the R, E and P. The $K_{\mu 2}$ peak events were selected by requiring $R > 50$ cm. The selected $K_{\mu 2}$ peak events in the $\pi\nu\bar{\nu}(1)$ trigger were found to have longer range in the target, leading to a bias of 0.5 MeV/c higher momentum measurement when applying a π^+ hypothesis to the contribution from the energy loss in the target. After subtracting this bias for each $K_{\mu 2}$ peak event, the momentum distribution was seen to be in good agreement with that from the $K_{\mu 2}$ range tail events and with more statistics in the signal region defined below 229 MeV/c. Normalizing the number of $K_{\mu 2}$ peak events to that of the $K_{\mu 2}$ range tail events observed in the region B + D gave the expected number of events B in the normalization branch. The expected $K_{\mu 2}$ range tail background is given in Table VII. Figure 30 shows the number of $K_{\mu 2}$ range tail background events as a function of the maximum momentum cut position in the normalization branch.

The μ^+ band background came from the RP resolution effects, which were well described by the range deviation (χ_{rm}) in RS. Enhancing the number of events in the study of the RP resolution effects was achieved by removing the PV cuts and the RS energy loss cuts in the normalization branch sample, since they were not correlated with the range and momentum measurements. Within the statistical uncertainty, both distributions were seen to be consistent except that the distribution without the above requirements

gave higher statistics in the normalization branch (Fig. 30). The estimated background level for the μ^+ band is given in Table VII.

3. Single beam background

In the study of single beam background, the two bifurcation cuts chosen were the offline delayed coincidence (DC) cuts (CUT1) and the B4 energy loss cut (CUT2). The offline DC cuts were from the precise offline time measurements from the beam instrumentation, the target, the IC and the RS (they were not the ones used in the trigger). The events were selected from the skim 6 sample by applying the PV cuts, the KIN cuts, the TD cuts, and the beam cuts except for the DC cuts and the B4 energy loss cut. In the normalization branch, the single beam events were selected by inverting the DC cuts ($\overline{\text{CUT1}}$). The B4 energy loss cut (CUT2) was applied to the above selected single beam sample, leaving 8 events in the region B for the normalization branch. In the rejection branch, 29 100 single beam events in the region C + D were selected by inverting the B4 energy loss cut ($\overline{\text{CUT2}}$). The DC cuts were applied to these selected events, resulting in 4 events in the region C. The rejection factor was applied for both the π^+ scattering events and the K^+ decay-in-flight events, since there was no reason to have different rejections for these. The background estimate for the single beam background is given in Table VII.

4. Double beam background

As already defined in Sec. III A, the double beam background could be due to a $K^+ - K^+$ event or a $K^+ - \pi^+$ event. For this double beam background, the DC cuts were insufficient to remove the double beam background, but the time difference between the beam instrumentation (C_K, C_π, BWPCs and B4) and the π^+ track was a good indicator. Another independent way was to use the target pattern to identify extra particles other than the initial K^+ hit.

The two bifurcation cuts chosen were the BWPC timing cuts (CUT1) and the B4 timing cuts (CUT2). The events were selected from the skim 6 sample by applying the PV cuts, the KIN cuts, the TD cuts and the beam cuts except for the BWPC and the B4 timing cuts. These cuts removed the $K_{\pi 2}$, μ^+ and single beam backgrounds. In the normalization branch, there were no events left if the B4 timing cuts (CUT2) were applied. In order to give a more precise estimate, the second bifurcation was adopted. Time measurements including the trailing edge TDC time from the C_K and C_π were used to select $K^+ - K^+$ events and $K^+ - \pi^+$, separately. The bifurcation analyses were then performed using the B4 timing cuts and the target pattern recognition cuts. Results are given in Table VII. In the rejection branch, the double beam background events were selected by inverting the B4 timing cuts ($\overline{\text{CUT2}}$). The $K^+ - K^+$ and $K^+ - \pi^+$ events were tagged by the C_K and C_π, separately; this resulted in 1170 and 22 150 events for both cases. Applying the BWPC timing cuts (CUT1) resulted in 10 and 3 events observed for the $K^+ - K^+$ and $K^+ - \pi^+$ backgrounds, respectively. The resulting rejections and background estimates are given in Table VII. The $K^+ - K^+$ background was found to dominate the double beam background.

5. Charge exchange background

Since there was no reliable way to isolate the CEX events from the $\pi\nu\bar{\nu}(1)$ trigger data, the background study could only rely on the Monte Carlo simulation. The CEX simulation needed a number of inputs, such as the CEX regeneration rate as a function of K_L^0 energy, the K_L^0 decay vertex and the K_L^0 momentum, all of which could only be obtained from the real data. A special CEX monitor trigger as described in Sec. II H 3 was used for collecting data with two charged tracks from the K_S^0 decay. The K_S^0's were reconstructed in the $\pi^+\pi^-$ decay mode and used to measure the K_S^0 production rate, momentum spectrum, the B4 hit information, decay vertex distribution, and pattern of target K^+ fibers' time and energy. Since a K^0 decays approximately equally to K_L^0 and K_S^0 states, the measured rate of K_S^0 decays can be used to obtain the K_L^0 production rate in the target

$$R_{K_L^0} \equiv \frac{N_{K_S^0}}{\epsilon_{K_S^0} \cdot A_{PV} \cdot \mathcal{B}(K_S^0 \to \pi^+\pi^-) \cdot N_K/PS} \tag{25}$$

$$= 2.73 \times 10^{-5}, \tag{26}$$

where the quantities used in this calculation are summarized in Table VIII.

Both $K_L^0 \to \pi^+\mu^-\bar{\nu}_\mu$ ($K_{\mu 3}^0$) and $K_L^0 \to \pi^+e^-\bar{\nu}_e$ (K_{e3}^0) decays were simulated to estimate the CEX background level. Each decay mode was generated with the amount of K_L^0 decays equivalent to 7.604×10^{15} K_L^0's. These Monte Carlo events were passed through all of the selection criteria, except for the $\pi^+ \to \mu^+ \to e^+$ decay sequence cuts and the beam cuts that were not related to target quantities. There were 56 K_{e3}^0 events and 21 $K_{\mu 3}^0$ events surviving in the signal region. Therefore, the expected CEX events can be estimated by means of

TABLE VIII. K_L^0 production rate and the quantities that are used to estimate it.

Description	Parameter	Values
Number of selected K_S^0 events	$N_{K_S^0}$	8086
K_S^0 selection efficiency	$\epsilon_{K_S^0}$	0.138
Photon veto efficiency	A_{PV}	0.680
$K_S^0 \to \pi^+\pi^-$ branching ratio	$\mathcal{B}(K_S^0 \to \pi^+\pi^-)$	0.686
Number of K^+ triggers (10^{12})	N_K	1.77
Prescaling factor	PS	384
K_L^0 Production rate	$R_{K_L^0}$	2.73×10^{-5}

$$N_{\rm CEX} = (N_{\rm pass}^{K^0_{e3}} + N_{\rm pass}^{K^0_{\mu 3}}) \times \frac{N_K}{N_K^{MC}} \times F_{\rm acc}$$
$$= (56 + 21) \times \frac{1.77 \times 10^{12}}{7.604 \times 10^{15}} \times 0.250$$
$$= 0.004\,48 \pm 0.000\,51({\rm stat}), \qquad (27)$$

where $N_{\rm pass}^{K^0_{e3}}$ and $N_{\rm pass}^{K^0_{\mu 3}}$ are the numbers of K^0_{e3} and $K^0_{\mu 3}$ events surviving all the cuts, N_K^{MC} was the total exposure of generated K^+'s and $F_{\rm acc}$ was the acceptance of the TD and beam cuts that were not applied to in the simulation.

6. Initial background evaluated from 1/3 *sample*

The initial total background evaluation based on the 1/3 sample was $0.05 \pm 0.01_{\rm stat}$ events, which came from the results in Table VII and Eq. (27). Given this relatively low background level, the signal region was expanded to gain acceptance at the cost of more background. In addition to the total background level, the bifurcation analyses gave the corresponding predicted background functions for the TD, the PV and the kinematic cuts, with which the expected background level and relative acceptance change for a given cut position were obtained. These functions were used in optimizing the selection criteria, studying the correlation of two bifurcation cuts and determining the branching ratio as well.

7. Optimization of signal region

The distributions of signal and background in the cut space were described well by the predicted background functions and were used to enlarge the signal region. The cuts to be loosened were the NN $\pi^+ \to \mu^+ \to e^+$ decay cut in the TD cuts (Fig. 26), the PV cuts (Fig. 29) and the $K_{\pi 2}$ kinematic cuts (Fig. 30). Loosening the cuts for the beam backgrounds and the other TD and KIN cuts did not provide much acceptance gain. Simultaneously loosening the cut positions of the NN $\pi^+ \to \mu^+ \to e^+$ decay, PV and $K_{\pi 2}$ kinematic cuts could increase the background levels to an unacceptable level. Instead, when one of the three cuts was loosened, the cut positions of the other two were kept unchanged. The revised (extended) signal region consisted of the standard signal region plus three extensions. Hereafter, the revised and standard signal regions are referred to as the extended signal region and the standard region, respectively. The regions created by loosening the NN $\pi^+ \to \mu^+ \to e^+$ decay cut, the PV cuts, and the $K_{\pi 2}$ kinematic cuts are referred to as $\pi^+ \to \mu^+ \to e^+$ extended, PV extended, and $K_{\pi 2}$ kinematic extended regions, respectively. All of which included the standard regions. The loosening factors for these three cuts, $f_{\pi\mu e} = 4.2$, $f_{PV} = 4.0$ and $f_{K_{\pi 2}} = 9.5$, meant the corresponding background increased by the same factor. The total estimated acceptance gain by enlarging the signal region was 31% (12% from the NN $\pi^+ \to \mu^+ \to e^+$ decay cut, 7% from the PV cuts, and 12% from the $K_{\pi 2}$ kinematic cuts).

8. Correlation and single cut failure study

The bifurcation procedure described above assumed that the two bifurcation cuts were not correlated. This assumption was tested by comparing the predicted and observed rates near but outside the signal region.

A schematic representation of the region near, but outside, the signal region is shown in Fig. 31. A near region outside the signal region (A′ without the black region in Fig. 31) was defined by loosening two bifurcation cuts (CUT1 and CUT2) simultaneously by the fixed factors a and b, respectively. If the predicted background functions associated with the CUT1 and CUT2 were correct, the expected number of background events in the near region (BG') was estimated by the bifurcation method as

$$BG' = B'C'/D' - BC/D. \qquad (28)$$

If a deviation was seen between the observed and the predicted numbers in the near region, then a correlation between the bifurcation cuts could be indicated and the background estimate might be unreliable. The observation was performed in the same way as the bifurcation method used in the background estimation in the signal region, except that two bifurcation cuts were loosened by factors of a and b.

The results of the correlation study for the $K_{\pi 2}$, $K_{\mu 2}$ range tail and μ^+ band backgrounds are summarized in Table X for the 2/3 data sample. Good agreement was found between the observed and the predicted number of events. The test results were obtained from the comparisons between the observed and the predicted numbers of events using the predicted background function method.

In addition to the study of correlation between the cuts used for the bifurcation method, events that passed all

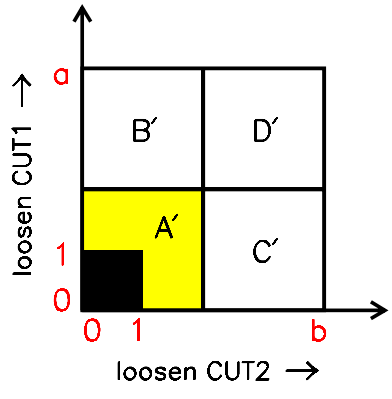

FIG. 31 (color online). Pictorial explanation of the correlation study using the events near, but outside the signal region. The vertical axis "a" and the horizontal axis "b" are for the loosening factors, while the 1×1 black region represents the standard signal region.

TABLE IX. Total background level and the contribution from each background source for both standard and extended signal regions as estimated from the 2/3 data samples. The errors are statistical.

Background	Standard	Extended
$K_{\pi 2}$	0.019 ± 0.004	0.216 ± 0.023
$K_{\mu 2}$ range tail	0.010 ± 0.001	0.044 ± 0.005
μ^+ band	0.005 ± 0.002	0.024 ± 0.010
Single beam	0.004 ± 0.002	0.006 ± 0.002
Double beam	0.003 ± 0.002	0.003 ± 0.002
CEX	0.004 ± 0.001	0.005 ± 0.001
Total	0.05 ± 0.01	0.30 ± 0.03

except for a single cut were examined to determine if each cut operated as designed for the appropriate background mechanism. Such a study provided a way to discover any new type of background or potential analysis flaw. In the 1/3 sample, six of the eight events that failed a single cut only were far from the cut position, while the other two events showed potential analysis flaws. The first flaw would artificially increase the measured range and momentum of π^+'s from $K_{\pi 2}$ decays that exited the upstream end of the target through the gap between the front face of the target and the B4 hodoscope. Additional cuts with minimal acceptance loss were devised to eliminate such events. The second revealed a possible correlation between the PV cuts and the KIN cuts when using the π^+ polar angle (θ) as a reference to exclude the accidental hits in the opposite site of the PV counters. The corresponding calculation used in the PV cuts was subsequently removed. All the cuts designed at this stage were referred to as pathology cuts as described in Sec. III F 1.

9. Final background evaluated from 2/3 sample

Evaluation of the final background levels came from the 2/3 sample. To get the values for the extended box, the corresponding values were scaled by the loosening factors given in Sec. III G 7. It was noted that loosening the NN $\pi^+ \to \mu^+ \to e^+$ decay cut, the PV cuts, and the $K_{\pi 2}$ kinematic cuts could lead to a small change in the beam background levels. Therefore, the beam backgrounds were reestimated in the extended signal region. The TD rejection and PV rejection were measured to be 445 ± 111 and 84.3 ± 1.2 with the 2/3 sample in good agreement with those obtained from the 1/3 sample given in Table VII. The final background estimates are summarized in Table IX.

The total background level in the extended signal region was estimated to be $0.30 \pm 0.03_{\text{stat}}$ events, which was dominated by the $K_{\pi 2}$ background contribution. As the background distribution was not uniform in the signal region, the predicted background functions obtained in the background study were exploited to interpret any possible candidate events observed and to give a proper branching ratio measurement by using the likelihood technique described in Sec. IV.

10. Systematic uncertainty

Systematic uncertainty in the background estimates arose from the possible correlation between the two bifurcation cuts. The correlation was investigated using the 2/3 sample and the results are given in Table X. In addition, the ratios of observations over predictions were used to quantify the degree of consistency and were found to be consistent with unity within a relative uncertainty of 15%, confirming that the background estimations obtained with the bifurcation method were reliable.

H. Acceptance and sensitivity

To reduce the estimated background level to less than one event in the signal region, this analysis utilized many selection criteria. The corresponding acceptances for these selection criteria were estimated directly from the data when possible, by splitting them into components that could be measured separately using the monitor trigger

TABLE X. Results of a correlation study for the $K_{\pi 2}$ (top), $K_{\mu 2}$ range tail (middle) and μ^+ band (bottom) backgrounds in the 2/3 sample. The errors in the predictions are statistical uncertainties.

$K_{\pi 2}$	(PV cuts) $\times$ ($K_{\pi 2}$ kinematic cuts)				
Loosening factor	10×10	20×20	20×50	50×50	50×100
Prediction	1.1 ± 0.2	4.9 ± 0.6	12.4 ± 1.3	31.1 ± 3.1	62.4 ± 5.6
Observation	3	4	9	22	53
$K_{\mu 2}$ range tail	($\pi^+ \to \mu^+ \to e^+$) $\times$ (maximum momentum cut)				
Loosening factor	10×10	20×20	50×50	80×50	120×50
Prediction	0.4 ± 0.0	1.4 ± 0.1	9.1 ± 0.6	14.5 ± 1.0	21.8 ± 1.5
Observation	0	1	12	16	25
μ^+ band	($\pi^+ \to \mu^+ \to e^+$) $\times$ (range-momentum cut)				
Loosening factor	10×10	20×20	50×20	80×20	80×40
Prediction	0.3 ± 0.1	1.3 ± 0.4	3.2 ± 0.9	5.2 ± 1.5	10.4 ± 2.8
Observation	1	1	4	5	11

data or the Monte Carlo simulation. The latter gave the estimates on the decay phase space, the trigger efficiency and the nuclear interaction effects.

1. Acceptance factors from $K_{\mu 2}$ events

Since the $K_{\mu 2}$ events have the same features as the signal regarding the K^+ beam, the charged track and the event topology, the acceptances associated with the relevant cuts as listed in Table XI were directly measured using the $K\mu 2$ monitor trigger data. Below are the details of these measurements.

Tracking in RS: To measure the acceptance of RS tracking, additional requirements ("setup cuts") were applied to $K\mu 2$ monitor data to ensure a good track in the RS without using RS measurements. The events were required to have an IC hit with $t_{IC} - t_{C_K} > 5$ ns, at least 1.2 MeV energy loss in B4, and successful tracking in both the UTC and target. All surviving $K_{\mu 2}$ events were examined for consistency with RS tracking. The acceptance of the RS tracking cuts is given in the second row of Table XI.

Tracking in UTC and target: Because there should be no photon activity for $K_{\mu 2}$ peak events, the $K\mu 2$ monitor was an ideal sample to measure the acceptance of target pattern recognition criteria. The sample was taken from events surviving the RS tracking cuts discussed above. To eliminate possible beam background contamination, this sample was also required to meet the timing requirements on the beam instruments. A 5 ns timing consistency was also required between t_{IC} and t_{rs}. A subset of the PV cuts was applied to suppress possible $K_{\mu 2\gamma}$ contamination. The BV and BVL elements of the PV cuts were not applied to avoid self-vetoing by long-range $K_{\mu 2}$ events. Events surviving the setup cuts were then checked with the UTC and target requirements except for those involving π^+ energy and range measurement in the target, giving a measurement of the acceptance of tracking in UTC and target (Table XI).

Beam selection criteria: The $K_{\mu 2}$ events were chosen from those satisfying the requirements on tracking in the UTC and target described above but without the timing requirements on the beam instruments. To suppress beam background contamination, the momentum deviation was required to be within two standard deviations of the $K_{\mu 2}$ peak with $|\cos\theta| < 0.5$. Also required was that there should be no discernible scattering of tracks in the RS. The remaining events then passed through the beam cuts except for the pathology cuts using π^+ energy and range measurement information described in Sec. III F 1, providing a measurement of the corresponding beam selection acceptance. Because $K_{\mu 2}$ events were simple single tracks, the efficiency of the DC trigger was also measured and included in the acceptance of beam selection criteria (Table XI).

Photon veto: The acceptance of the PV cuts included contributions from both the online and offline PV. Ideally, $K_{\mu 2}$ events should not contain any photons, and could thus be used to measure the acceptance loss due to the PV cuts. In the first step of this procedure, the selection criteria were applied to remove possible beam backgrounds. However, it was noted that some μ^+'s could penetrate the whole RS and reach the PV counters, resulting in a time-coincident PV hit and therefore an overcounting in the acceptance loss due to the PV cuts. To avoid this problem, the selected $K_{\mu 2}$ sample was further required to have the stopping layers prior to the 19th RS layer. The PV cuts were then applied to the surviving $K_{\mu 2}$ events, yielding a measurement of the acceptance loss due to the application of the PV cuts. Since the $K\mu 2(1)$ trigger did not have an online PV cut applied, this acceptance factor also included the contribution from the online PV (Table XI).

Track stop in RSSC: This cut was classified into the fiducial cuts in Sec. III F 2 and aimed at vetoing possible associated photon activity detected by the RSSC, even though it was not included in the PV cuts. Using the $K\mu 2$ monitor events and applying the above cut to those with hits in the second layer of RSSC gave a measurement of the corresponding acceptance value (Table XI).

Muon veto in RS: The $\pi\nu\bar{\nu}(1)$ trigger condition $\overline{19_{ct}}$ was also called as a muon veto in RS. This trigger requirement could result in acceptance losses when an accidental hit happened in the 19th layer along with an otherwise good signal candidate event. This loss was measured with the $K\mu 2$ monitor events, which were selected by requiring the stopping layer to be RS layer 17 and the range to be longer than 40 cm, in addition to applying all the cuts used in the above studies except for the momentum cut. In this selected sample, the online trigger condition $\overline{19_{ct}}$ was checked, giving a measurement of the acceptance for the muon veto in RS (Table XI).

TABLE XI. Acceptances of the $K^+ \to \pi^+\nu\bar{\nu}$ selection cuts measured from the $K_{\mu 2}$ monitor trigger data. The acceptance of beam cuts does not include those using the energy measurement in the target. The errors are statistical.

Cut	Acceptance
Tracking in RS	0.99996 ± 0.00001
Tracking in UTC and target	0.99568 ± 0.00010
Beam selection criteria	0.50779 ± 0.00074
Photon veto	0.76784 ± 0.00218
Track stop in RSSC	0.98195 ± 0.00015
Muon veto in RS	0.99591 ± 0.00057
$A_{K_{\mu 2}}$	0.3796 ± 0.0013

2. Acceptance factors from $K_{\pi 2}$ events

The $K\pi 2(1)$ monitor trigger data were used to measure the acceptances for the pathology beam cuts involving the π^+ energy and range measurement and the KIN cuts involving the range-energy consistency in IC and target. This was a complement to the measurement of acceptance

factors from the $K_{\mu 2}$ events. The $K_{\pi 2}$ events were selected with all cuts applied except for those to be measured. To ensure good $K_{\pi 2}$ events, the momentum, range and energy were required to be within two standard deviations of the $K_{\pi 2}$ peak positions and observation of a $\pi^0 \to \gamma\gamma$ decay was required. The result was

$$A_{K_{\pi 2}} = 0.8785 \pm 0.0029_{\text{stat}}. \tag{29}$$

3. Kinematic acceptance from beam π^+ events

The π_{scat} monitor trigger data provided a pure π^+ sample to measure the KIN cuts related to the particle type: the cut on π^+ stopping layer in the fiducial cuts, the cuts on tracking quality in UTC and RS, the cuts energy loss in RS and the cut on range-momentum consistency in UTC and RS. The events were required to pass the pass 1 cuts and the TD cuts. The K^+ selection criteria in the beam instruments were inverted to select beam π^+'s. The t_{IC} was required to be within ± 5 ns of t_{rs}. The signal phase space cuts were additionally applied to select the events. The acceptance was measured to be

$$A_{\pi_{\text{scat}}} = 0.6161 \pm 0.0085_{\text{stat}} \pm 0.0189_{\text{sys}}. \tag{30}$$

Since these π^+'s came from the beam π^+'s scattering in the target and not from the K^+ decays at rest, classification of the K^+ fibers and π^+ fibers could be complicated because of their nearly coincident times and differences in fiber energy deposits of scattered π^+'s and K^+ decays at rest. Both of these features would result in more uncertainties in the momentum, energy and range measurements in these π^+ events. Systematic uncertainties were therefore investigated by loosening or tightening the signal phase space cuts by ± 1 standard deviation. The corresponding variation in acceptance was treated as the systematic uncertainty.

4. $\pi^+ \to \mu^+ \to e^+$ decay acceptance from beam π^+ events

The acceptance of $\pi^+ \to \mu^+ \to e^+$ decay sequence cuts was measured by using the π_{scat} monitor trigger data. This acceptance measurement included the online and offline (TD) π^+ identification cuts. The online ones included $L1.1$ and $L1.2$ in trigger. The sample was selected using the same cuts as those used in measuring $A_{\pi_{\text{scat}}}$ except for the cuts to be measured here. It should be noted that this measurement included the acceptance loss due to the π^+ absorption and π^+ decay in flight. This loss was estimated to be 1.4% using Monte Carlo in Sec. III H 5 and should be corrected to remove the double counting problem in the acceptance. The final acceptance of $\pi^+ \to \mu^+ \to e^+$ decay sequence cuts was given below

$$A_{\pi\to\mu\to e} = 0.3523 \pm 0.0077_{\text{stat}} \pm 0.0067_{\text{sys}}. \tag{31}$$

Since the $\pi^+ \to \mu^+ \to e^+$ decay sequence cuts might be correlated to particle identification KIN cuts when using information from the RS, the effect on acceptance was investigated with and without the RS energy loss cuts. The observed about 2% variation on the relative acceptance was assigned as the systematic uncertainty.

5. Acceptance factors from Monte Carlo simulation

Monte Carlo simulations of the $K^+ \to \pi^+\nu\bar{\nu}$ were used to evaluate the trigger acceptance, the phase space acceptances and the acceptance loss due to π^+ absorption, decay in flight, and nuclear interaction, which could not be measured directly by the monitor trigger data. The $K^+ \to \pi^+\nu\bar{\nu}$ Monte Carlo samples were generated with and without including the nuclear interaction.

Trigger requirements: All the trigger requirements as described in Sec. II H were simulated by Monte Carlo except for the DC, $L1.1$ and $L1.2$, which were already measured using the $K_{\mu 2}$ and π_{scat} monitor trigger data. From the Monte Carlo without including the nuclear interaction, the acceptance for the trigger requirements was

$$A_{\text{trig}} = 0.1796 \pm 0.0010_{\text{stat}} \pm 0.0084_{\text{sys}}, \tag{32}$$

where the systematic uncertainty was estimated to be 4.7% from the measurement on the branching ratio of $K_{\pi 2}$ in Sec. III H 8. It was noted that the trigger acceptance measured here was primarily due to geometry.

Phase space: The phase space acceptance was used to determine the acceptance of offline cuts on the momentum, range and energy. To measure the phase space acceptances (A_{PS}), events were first taken from those surviving from the trigger in the Monte Carlo simulation, and then the phase space cuts were applied. The π^+ nuclear interaction was not included in this simulation. The acceptance was measured to be

$$A_{PS} = 0.3630 \pm 0.0029_{\text{stat}}, \tag{33}$$

which included the loss due to both π^+ absorption and decay in flight.

Correction for nuclear interaction: The nuclear interaction effect was investigated separately, in order to study the systematic uncertainty associated with it. $K^+ \to \pi^+\nu\bar{\nu}$ events were generated with and without nuclear interaction, respectively. The ratio between the trigger acceptances multiplied by the ratio between the phase space acceptances gave the correction for nuclear interaction

$$A_{\text{nucl}} = 0.4953 \pm 0.0077_{\text{stat}} \pm 0.0248_{\text{sys}}, \tag{34}$$

where the systematic uncertainty took into account the observed 0.15 cm difference on the range resolution (Table II). This difference could affect the acceptance due to the Rdev cut and translated into a 5% uncertainty in the acceptance. It should be pointed out that this definition took into account the losses associated with nuclear interactions. For example, there could be extra energy in the detector associated with nuclear interactions that

caused the PV counters to fire. This loss was not included in the $K_{\mu 2}$-based acceptance $A_{K_{\mu 2}}$ given in Table XI because muon-nuclear interactions are rare.

6. Correction to $T \cdot 2$ trigger inefficiency

The $T \cdot 2$ trigger required coincident hits both in the innermost two RS layers and in the IC. It was noted that the $T \cdot 2$ simulation result did not include the acceptance loss due to the geometrical and counter inefficiencies of the T counters. The geometrical inefficiency was due to tracks passing through azimuthal gaps between adjacent T counters. The counter inefficiency occurred if the scintillation light induced by the charged track was not detected by the PMTs. This inefficiency was measured by using the $K_{\mu 2}$ and $K_{\pi 2}$ events in the KB monitor data. UTC track extrapolation was required to give the expected $T \cdot 2$ counter. The online $T \cdot 2$ trigger condition of the reconstructed event data was checked to measure the $T \cdot 2$ efficiency for $K_{\mu 2}$ and $K_{\pi 2}$ events, separately. Since the energy losses in the $T \cdot 2$ counter from the $K_{\mu 2}$ and $K_{\pi 2}$ events were different, simulations were done for these decay modes to obtain the average energy loss for $K_{\mu 2}$ and $K_{\pi 2}$. Using an energy extrapolation gave the correction to the $T \cdot 2$ inefficiency for the signal

$$A_{T\cdot 2} = 0.9358 \pm 0.0011(\text{stat}) \pm 0.0140(\text{sys}), \tag{35}$$

where the systematic uncertainty accounted for the fact that there was a 1.5% variation when changing the z requirement on the UTC track extrapolation to the $T \cdot 2$ counter.

7. Normalization to the $K_{\mu 2}$ branching ratio

Since a beam K^+ could decay after the Čerenkov counter with a daughter satisfying the B4 and target requirement in KB, or a beam K^+ could deposit energy in the B4 and target but exit the target without stopping, the total number of K^+'s that satisfy the KB trigger requirement should be corrected for the K^+ stopping fraction (f_s). This fraction was obtained by normalizing the total K^+ exposure to the $K_{\mu 2}$ branching ratio. The $K_{\mu 2}$ events were selected from the $K\mu 2$ monitor trigger data with the same selection criteria as those used for signal, excluding all the cuts related to the π^+ particle type, the BV and the BVL. The momentum, range and energy cuts for signal were replaced by a minimum 40 cm range requirement on the $K_{\mu 2}$ events. The $K_{\mu 2}$ acceptance measurement was also performed in the same way as that for the signal. This stopping fraction was computed by

$$\begin{aligned} f_s &= \frac{N_{K_{\mu 2}}}{N_K^{\text{eff}}(K_{\mu 2}) \cdot Acc(K_{\mu 2}) \cdot \mathcal{B}(K^+ \to \mu^+ \bar{\nu}_\mu)} \\ &= 0.7740 \pm 0.0011_{\text{stat}}, \end{aligned} \tag{36}$$

where the $N_{K_{\mu 2}} = 355\,119$ and was the number of surviving $K_{\mu 2}$ events. $N_K^{\text{eff}}(K_{\mu 2}) = 4.1475 \times 10^6$ and was the total exposure of K^+'s (N_K) with a prescaling factor for the $K\mu 2$ monitor trigger during the data acquisition period. $Acc(K_{\mu 2}) = 17.4\%$ and was the acceptance.

8. Confirmation of the $K_{\pi 2}$ branching ratio

Measurement of the $K_{\pi 2}$ branching ratio confirmed the validity of the evaluation of the acceptance of the $K^+ \to \pi^+ \nu \bar{\nu}$ selection cuts. Stopped $K_{\pi 2}$ events were selected from the $K\pi 2(1)$ monitor trigger data by imposing cuts similar to the $K^+ \to \pi^+ \nu \bar{\nu}$ selection criteria except for those used for the PV cuts and for defining the kinematic signal region. Good $K_{\pi 2}$ events should also meet the requirements on the energy, momentum and range, which were defined to be within three standard deviations of the $K_{\pi 2}$ peaks. Figure 32 shows the stability of the measured $K_{\pi 2}$ branching ratio as a function of run number. The $K_{\pi 2}$ branching ratio was measured to be

$$\begin{aligned} \mathcal{B}(K^+ \to \pi^+ \pi^0) &= \frac{N_{K_{\pi 2}}}{N_K^{\text{eff}}(K_{\pi 2}) \cdot Acc(K_{\pi 2}) \cdot f_s} \\ &= 0.219 \pm 0.005_{\text{stat}}, \end{aligned} \tag{37}$$

where $N_{K_{\pi 2}} = 16\,405$ and was the number of surviving $K_{\pi 2}$ events. $N_K^{\text{eff}}(K_{\pi 2}) = 1.3233 \times 10^6$ and was the total exposure of K^+'s (N_K) with a prescaling factor for the $K\pi 2(1)$ monitor trigger during the data acquisition period. $Acc(K_{\pi 2}) = 7.3\%$ and was the acceptance. This branching ratio was in agreement with the world average [18] value of 0.209 ± 0.001 within 4.7%, indicating the validation of the acceptance measurement. This difference was treated as the systematic uncertainty and assigned to the acceptance A_{trig} in Eq. (32).

9. Summary of acceptance and sensitivity

The acceptances of the $K^+ \to \pi^+ \nu \bar{\nu}$ decay were split into several parts as given above. Table XII summarizes all the contributions to the total acceptance in the standard region $A_{\text{total}}^{\text{standard}}$. To get the acceptance in the extended signal region, the estimated acceptance gains given in Sec. III G 7 were applied to the acceptances for $A_{\pi \to \mu \to e}$, $A_{K_{\pi 2}}$ and A_{PS}, yielding the final acceptance of

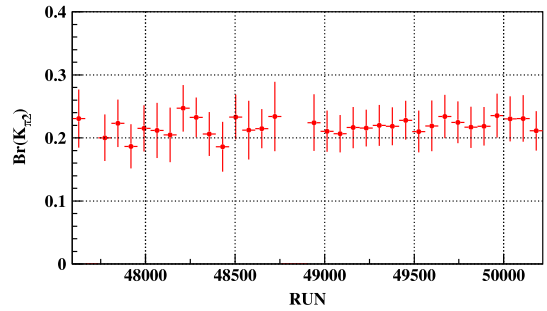

FIG. 32 (color online). Measurement of the $K^+ \to \pi^+ \pi^0$ branching ratio as a function of run number in E949.

TABLE XII. A breakdown of the acceptance for the $K^+ \to \pi^+ \nu\bar{\nu}$ selection criteria.

Contribution	Acceptance
$A_{K_{\mu 2}}$	$0.3796 \pm 0.0013_{\rm stat}$
$A_{K_{\pi 2}}$	$0.8785 \pm 0.0029_{\rm stat}$
$A_{\pi_{\rm scat}}$	$0.6161 \pm 0.0085_{\rm stat} \pm 0.0189_{\rm sys}$
$A_{\pi\to\mu\to e}$	$0.3523 \pm 0.0077_{\rm stat} \pm 0.0067_{\rm sys}$
$A_{\rm trig}$	$0.1796 \pm 0.0010_{\rm stat} \pm 0.0084_{\rm sys}$
A_{PS}	$0.3630 \pm 0.0029_{\rm stat}$
$A_{\rm nucl.}$	$0.4953 \pm 0.0077_{\rm stat} \pm 0.0248_{\rm sys}$
$A_{T\cdot 2}$	$0.9358 \pm 0.0011_{\rm stat} \pm 0.0140_{\rm sys}$
f_s	$0.7740 \pm 0.0011_{\rm stat}$
$A_{\rm total}^{\rm standard}(\times 10^{-3})$	$1.69 \pm 0.05_{\rm stat} \pm 0.13_{\rm sys}$

$$Acc = (2.22 \pm 0.07_{\rm stat} \pm 0.15_{\rm sys}) \times 10^{-3}. \quad (38)$$

This value is 10% higher than that in E787. It is noted that the acceptance of the standard E787 signal region for the E949 data was 84% of the acceptance for the E787 data due to losses incurred by the higher than expected instantaneous rates (Sec. II A). Based on the total exposure of K^+'s (N_K), the single event sensitivity (SES) of the E949 2002 run was given by

$$\text{SES} = (2.55 \pm 0.08_{\rm stat} \pm 0.18_{\rm sys}) \times 10^{-10}. \quad (39)$$

I. Examining the signal region

After the background analysis and the acceptance measurement were completed and satisfactory, all the selection criteria were then applied to the data. At the stage of examining the signal region, no cut could be changed.

One candidate event was observed inside the signal region. A close check also found that this candidate was located in the $\pi^+ \to \mu^+ \to e^+$ extended region as described in Sec. III G 7. Figure 33 shows the range and kinetic energy of the events that passed all of the selection criteria, except for the phase space cuts on both the range and energy. This candidate together with the events observed in E787 are also shown in Fig. 33. As indicated in the figure, the signal box definition in E949 was extended in comparison to that in E787. Figure 34 is an event display for this candidate. This event had a momentum of 227.3 MeV/c, a kinetic energy of 128.9 MeV and a range of 39.2 cm. Kinematically, this candidate event agreed with all the requirements as a signal, though it existed near the limit expected for signal. The measured quantities of the observed candidate used in the selection criteria were compared to the expected distributions for signal to evaluate the signal probability distributions for the candidate. The probabilities for the single beam K^+ requirements, the decay π^+ kinematic requirements and the $\pi^+ \to \mu^+ \to e^+$ decay sequence cuts showed a fairly flat distribution, which was consistent with the expected signal distribution. There was no observed photon activity for this candidate.

IV. RESULTS

In this section we describe the method used to obtain the $K^+ \to \pi^+ \nu\bar{\nu}$ branching ratio and the impact of the E949 and E787 $K^+ \to \pi^+ \nu\bar{\nu}$ candidates on the unitarity triangle. We also describe the implication of the results on the search for the hypothetical decay $K^+ \to \pi^+ X^0$ where X^0 is a stable, massless, noninteracting particle [78].

A. Background functions

We defined a number of cells in the extended signal region of differing signal/background, and calculated the

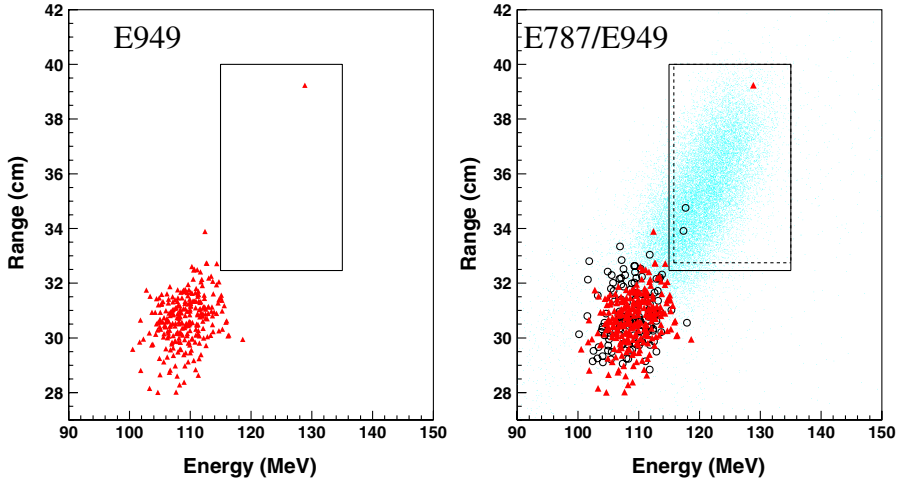

FIG. 33 (color online). Range versus kinetic energy of the events satisfying all of the cuts, except for the phase space cuts on both the range and energy. The plots are shown separately for E949 only (left) and E787 plus E949 results. The rectangle represents the signal region defined in E787 (dashed lines) and E949 (solid lines). Events around $E = 108$ MeV were due to $K_{\pi 2}$, which were not removed by the photon veto cuts. The light points in the right-hand plot represent the expected distribution of $K^+ \to \pi^+ \nu\bar{\nu}$ events from simulation.

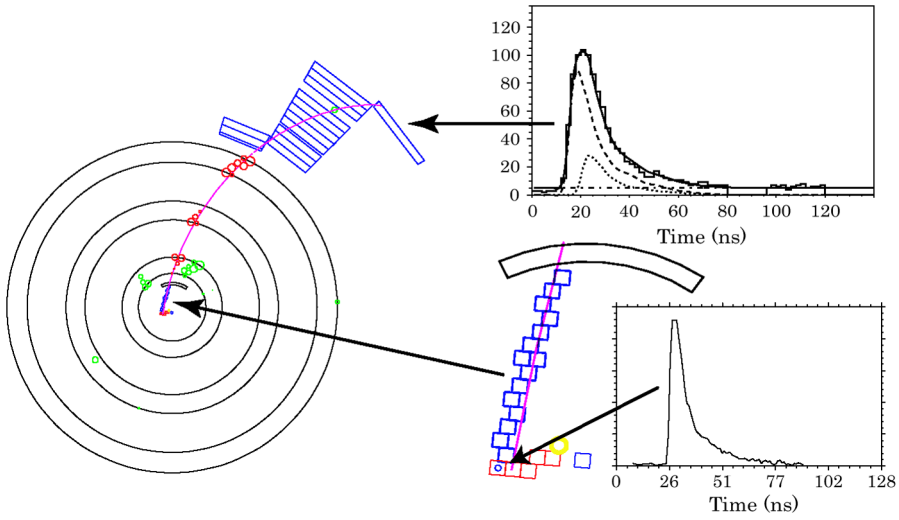

FIG. 34 (color online). Reconstruction of the candidate event (end view). The clusters of squares indicate both the K^+ track and the π^+ track in the target. The hit IC sector is shown next to the π^+ cluster in the target. The curve is the result of the UTC track fit. The circles along the track are the hits in the UTC. The radius of each circle gives the drift distance. The RS and RSSC hit layers are shown outside the UTC. Also displayed are the TD data in the π^+ stopping counter, the reconstruction in the target and the CCD data in the K^+ stopping fiber. In the fit to the TD pulse shape, the π^+ pulse (dashed line) and the μ^+ pulse (dotted line) are shown separately. No obvious π^+ pulse was observed in the CCD pulse shape for the K^+ stopping fiber.

expected signal/background (dA/dN) using individual $A^{\rm type}_{\pi\nu\nu}$ and $N^{\rm type}_{\pi\nu\nu}$ functions for each rejection or background type. In total, we had seven types: TD rejection, PV rejection, $K_{\pi 2}$ background, $K_{\mu 2}$ range tail background, μ^+ band background, single-beam background and double-beam background. The variation of each type for different cut position or cell could be expressed as the change of $N^{\rm type}_{\pi\nu\nu}$ as a function of the corresponding acceptance $A^{\rm type}_{\pi\nu\nu}$, yielding seven functions in total used in this analysis. Two of them were the TD rejection versus acceptance function (Fig. 26) and the PV rejection versus acceptance function (Fig. 29). Three of them were the relative background rate in the normalization branch versus the relative acceptance functions for the kinematic background backgrounds (Fig. 35). The rest were the relative background rate versus the relative acceptance functions for the beam backgrounds (Fig. 36). Both relative background rates and the relative acceptance curves were normalized to one at the cut positions.

B. Likelihood method

The $K^+ \to \pi^+ \nu\bar{\nu}$ branching ratio was determined using likelihood analysis incorporating the predicted background functions in the signal region. The likelihood ratio X was defined as

$$X \equiv \prod_{i=1}^{n} \frac{e^{-(s_i+b_i)}(s_i+b_i)^{d_i}}{d_i!} \Big/ \frac{e^{-b_i} b_i^{d_i}}{d_i!}, \qquad (40)$$

where s_i and b_i were the estimated signal and background in the ith cell, d_i was the number of signal candidates in the ith cell and the product ran over all n cells [79]. In addition

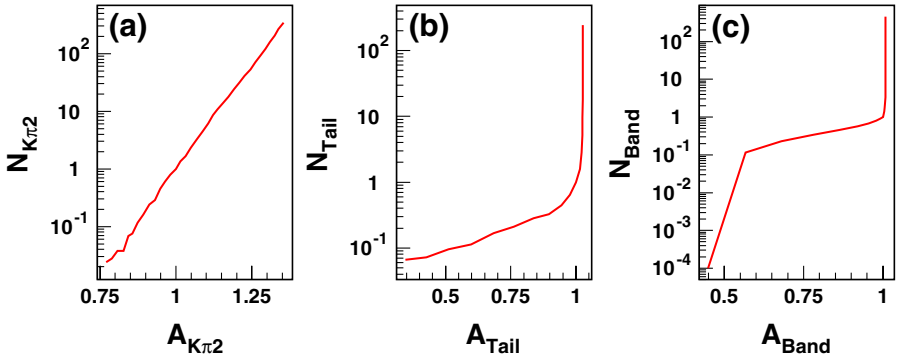

FIG. 35 (color online). The expected relative kinematic background rate in the normalization branch versus the relative acceptance for the $K_{\pi 2}$ background (a), the $K_{\mu 2}$ range tail background (b) and the μ^+ band background (c). Both background rates and acceptance curves were normalized to one at the cut positions.

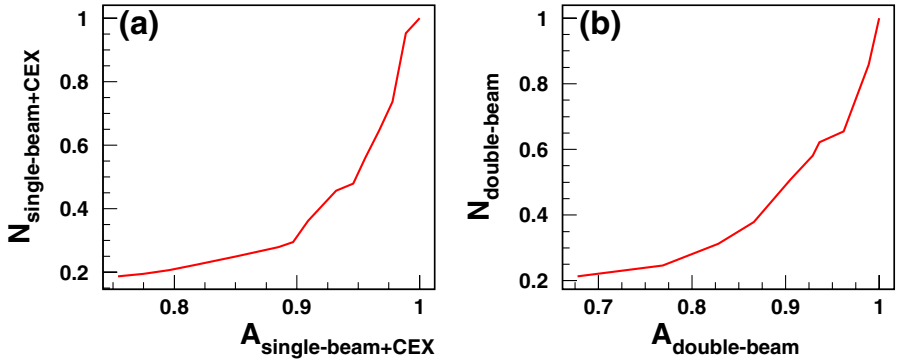

FIG. 36 (color online). The expected relative beam background rate versus the relative acceptance for the single-beam and CEX backgrounds (a) and the double-beam background (b). Both background rates and acceptance curves were normalized to one at the cut positions.

the likelihood estimator $X_{\rm obs}$ was defined as the value of X given the observed candidates. Cells were defined based on the predicted background functions described in the previous section. The predicted background functions showed that there was additional background rejection capability within the signal region that could be exploited by subdividing the signal region. The number of cells to be used for subsequent analysis, 3781, was established prior to the examination of the signal region.

The total background in the cell containing the signal candidate was estimated to be 5.75×10^{-5} dominated by a contamination of 4.92×10^{-5} events due to the $K_{\mu 2}$ range tail background. The ratio of the acceptance in this cell to the total acceptance in the standard region ($A_{\rm total}^{\rm standard} = 0.001\,694$) was estimated to be 1.21×10^{-4}. The expected number of signal events in this cell was

$$\begin{aligned} s_i &= N_K \cdot \mathcal{B} \cdot A_{\rm total}^{\rm standard} \cdot A_i \\ &= 1.77 \times 10^{12} \times \mathcal{B} \times 0.001\,694 \times 1.21 \times 10^{-4} \\ &= 3.628 \times 10^5 \times \mathcal{B}, \end{aligned} \tag{41}$$

where $\mathcal{B}$ was the $K^+ \to \pi^+ \nu\bar{\nu}$ branching ratio.

C. Branching ratio of $K^+ \to \pi^+ \nu\bar{\nu}$

The central value of the branching ratio, defined as the value of $\mathcal{B}$ that maximized $X_{\rm obs}$ [80], was 0.96×10^{-10}. Using only the E949 data, $\mathcal{B}(\mathrm{K}^+ \to \pi^+ \nu\bar{\nu}) = (0.96^{+4.09}_{-0.47}) \times 10^{-10}$ where the quoted 68% confidence level (C.L.) interval was determined from the behavior of X as described in Ref. [79] and included only the statistical uncertainty. The estimated probability that the E949 candidate was due to background alone was 0.074.

The results from E787 and E949 were combined to calculate the branching ratio for $K^+ \to \pi^+ \nu\bar{\nu}$. In the E787 $K^+ \to \pi^+ \nu\bar{\nu}$ analysis, two $K^+ \to \pi^+ \nu\bar{\nu}$ candidate events were observed in the signal region [55]. The number of cells describing the E949 signal region were augmented by 488 cells that defined the signal region for the E787 analysis to produce a likelihood estimator $X_{\rm obs}$ for the combined data.

The confidence intervals for the combined E787 and E949 results took into account the estimated systematic uncertainties in the signal acceptance and the background rates. The systematic uncertainty of each background source was estimated to be about 15% based upon the results of the correlation studies. From the study in Sec. III H, the systematic uncertainty on the acceptance was estimated to be about 8%. The systematic uncertainty of each background component and the acceptance were assumed to be uncorrelated and to follow a normal distribution with the magnitudes given above regarded as one standard deviation. With these assumptions, the $K^+ \to \pi^+ \nu\bar{\nu}$ branching ratio for the combined E787 and E949 result was $\mathcal{B}(\mathrm{K}^+ \to \pi^+ \nu\bar{\nu}) = (1.47^{+1.30}_{-0.89}) \times 10^{-10}$ where the uncertainty denoted the 68% C.L. interval. The corresponding 90% and 95% C.L. intervals were $(0.27, 3.84) \times 10^{-10}$ and $(0.17, 4.44) \times 10^{-10}$, respectively. The estimated probability that all the $K^+ \to \pi^+ \nu\bar{\nu}$ candidates observed in E787 and E949 were due to background was 0.001. The inclusion of the estimated systematic uncertainties had a negligible effect on the C.L. intervals due to the relatively poor statistical precision inherent in a sample of three candidate events.

D. Search for $\mathcal{B}(K^+ \to \pi^+ X^0)$

The experimental signature of a $K^+ \to \pi^+ X^0$ decay was identical to that of $K^+ \to \pi^+ \nu\bar{\nu}$ except that the kinematic signature afforded by the two-body decay ($P_\pi = 227.1$ MeV/c, $E_\pi = 127.0$ MeV, $R_\pi = 38.6$ cm) permitted the definition of a relatively high-acceptance, low-background signal region. The analysis method was identical to that used for the $K^+ \to \pi^+ \nu\bar{\nu}$ analysis except that the signal region was defined to be within two standard deviations of the expected momentum, energy and range of the π^+ with the upper limits to be tightened to $P \leq 229$ MeV/c, $E \leq 135$ MeV, and $R \leq 40$ cm to suppress $K^+ \to \mu^+ X$ background. The expected background level

was small (0.05 events), because the region was far from the $K_{\pi 2}$ peak. The acceptance studies for $K^+ \to \pi^+ X^0$ decay paralleled those for the $K^+ \to \pi^+ \nu\bar{\nu}$. The single event sensitivity for the E949 $K^+ \to \pi^+ X^0$ decay analysis was estimated to be $(0.82 \pm 0.02_{\rm stat} \pm 0.06_{\rm sys}) \times 10^{-10}$.

The candidate event observed in the signal region for $K^+ \to \pi^+ \nu\bar{\nu}$ E949 analysis was also in the $K^+ \to \pi^+ X^0$ signal region. However, no candidates were observed in the $K^+ \to \pi^+ X^0$ signal region of E787 [55]. The combined E787 and E949 sensitivity was 0.196×10^{-10} and, using the one observed candidate event without subtraction of the estimated background, the upper limit on the branching ratio was $\mathcal{B}(K^+ \to \pi^+ X^0) < 0.73 \times 10^{-10}$ at 90% C.L. using the Feldman-Cousins method [81]. This limit was larger than the previous 90% C.L. limit of 0.59×10^{-10} of E787 [55] due to the E949 candidate event.

E. Impact on the unitarity triangle

As described in Sec. I, the $K^+ \to \pi^+ \nu\bar{\nu}$ branching ratio was directly related to the real and imaginary parts of $\lambda_t \equiv V_{ts}^* V_{td}$ [Eq. (9)]. In Fig. 37 the regions of the complex λ_t plane allowed by the $K^+ \to \pi^+ \nu\bar{\nu}$ branching ratio determined from the combined E787 and E949 results were compared to the regions allowed by other recent measurements with small theoretical uncertainties [82]. The region favored by other CKM-sensitive measurements is at the edge of the 68% C.L. region allowed by the $K^+ \to \pi^+ \nu\bar{\nu}$ measurement.

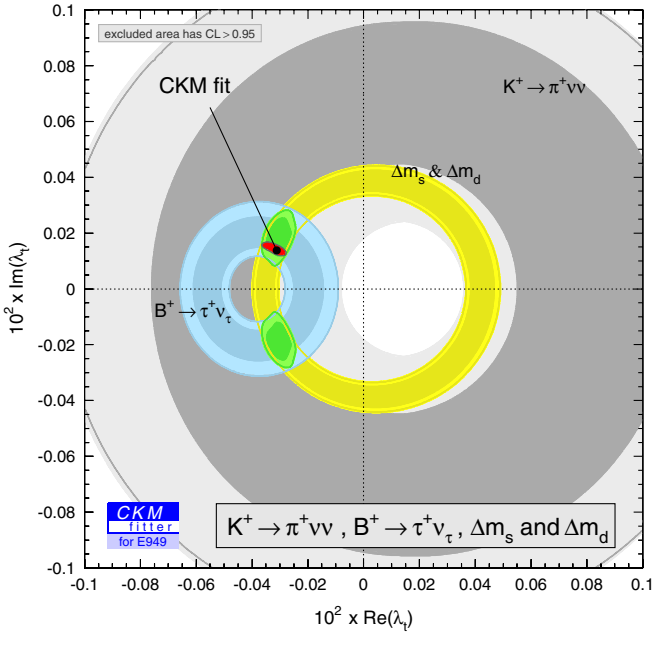

FIG. 37 (color online). The allowed regions in the λ_t plane allowed by the combined E787 and E949 determination of the $K^+ \to \pi^+ \nu\bar{\nu}$ branching ratio (gray), $B^+ \to \tau^+ \nu$ (blue) and B-mixing measurements (yellow). The regions outside the lighter (darker) shading have C.L. > 0.95 (0.68). The area excluded by $K^+ \to \pi^+ \nu\bar{\nu}$ at C.L. > 0.95 is indicated by the gray line. The red-shaded region is allowed by the combination of these measurements and the small black region denotes the region allowed by all CKM-related measurements as evaluated by the CKMfitter Group [82].

The other CKM-sensitive results [82] used to produce the confidence level intervals in Fig. 37 are dominated by measurements of B meson decays. The possible discrepancy between the λ_t regions allowed by the B-decay measurements and by $\mathcal{B}(K^+ \to \pi^+ \nu\bar{\nu})$ could be an indication of physics beyond the SM. As emphasized in Ref. [83], the clean theoretical interpretation of $K \to \pi\nu\bar{\nu}$ remains valid in most extensions of the SM in distinct contrast to the B-decay measurements currently used to determine the CKM parameters. Thus a precise measurement of $\mathcal{B}(K^+ \to \pi^+ \nu\bar{\nu})$ would provide an unambiguous consistency test of the flavor sector of the SM.

V. CONCLUSION

The rare decay $K^+ \to \pi^+ \nu\bar{\nu}$ is a flavor-changing-neutral-current process and proceeds via 1-loop diagrams mediated mainly by the top quark. Measuring $\mathcal{B}(K^+ \to \pi^+ \nu\bar{\nu})$ is one of the cleanest ways to extract $|V_{td}|$.

In this paper we have reported results from the BNL experiment E949, an upgraded version of the BNL-E787 experiment, designed to improve the sensitivity for measurement of $K^+ \to \pi^+ \nu\bar{\nu}$ decay. All the K^+ decays at rest were analyzed using a blind analysis technique in which the signal region was masked until the selection criteria were determined and the background levels were estimated. The development of the cuts and the estimation of the background levels were performed using a bifurcation method, and a likelihood analysis method was developed for interpreting the quality of candidate events. Enlargement of the signal region compared to E787 analysis increased the acceptance by 30% with a total background level in the signal region estimated to be 0.30 ± 0.03 events.

An examination of the signal region yielded one event near the upper kinematic limit of the decay $K^+ \to \pi^+ \nu\bar{\nu}$. Based on the candidate event, the branching ratio was determined to be $\mathcal{B}(K^+ \to \pi^+ \nu\bar{\nu}) = (0.96^{+4.09}_{-0.47}) \times 10^{-10}$. E787 and E949 results were combined and the branching ratio was determined to be $(1.47^{+1.30}_{-0.89}) \times 10^{-10}$ at the 68% C.L. level based on three events observed in the momentum region $211 \leq P \leq 229$ MeV/c. The estimated probability that all the $K^+ \to \pi^+ \nu\bar{\nu}$ candidates observed in E787 and E949 were due to background was 0.001. The measured branching ratio is in agreement with the SM prediction of $(0.74 \pm 0.20) \times 10^{-10}$ within the uncertainty.

ACKNOWLEDGMENTS

We gratefully acknowledge the support and efforts of the BNL Collider-Accelerator Division for the high quality K^+ beam delivered. We wish to thank Jose Ocariz of the

CKMfitter Group for producing Fig. 37. This research was supported in part by the U.S. Department of Energy, the Ministry of Education, Culture, Sports, Science and Technology of Japan through the Japan-U.S. Cooperative Research Program in High Energy Physics and under Grant-in-Aids for Scientific Research, the Natural Sciences and Engineering Research Council and the National Research Council of Canada, the Russian Federation State Scientific Center Institute for High Energy Physics, and the Ministry of Science and Education of the Russian Federation. S. C. was also supported by Program for New Century Excellent Talents in University from the Chinese Ministry of Education.

[1] W. Buchmuller, arXiv:hep-ph/0306047.
[2] A. D. Sakharov, JETP Lett. **5**, 24 (1967).
[3] V. A. Rubakov and M. E. Shaposhnikov, Usp. Fiz. Nauk **166**, 493 (1996) [Phys. Usp. **39**, 461 (1996)]; A. Riotto and M. Trodden, Annu. Rev. Nucl. Part. Sci. **49**, 35 (1999).
[4] V. V. Anisimovsky *et al.*, Phys. Rev. Lett. **93**, 031801 (2004).
[5] M. Kobayashi and T. Maskawa, Prog. Theor. Phys. **49**, 652 (1973).
[6] L. Wolfenstein, Phys. Rev. Lett. **51**, 1945 (1983).
[7] C. Jarlskog, Phys. Rev. Lett. **55**, 1039 (1985); Z. Phys. C **29**, 491 (1985); C. Jarlskog and R. Stora, Phys. Lett. B **208**, 268 (1988).
[8] A. J. Buras, M. E. Lautenbacher, and G. Ostermaier, Phys. Rev. D **50**, 3433 (1994).
[9] A. J. Buras, F. Schwab, and S. Uhlig, arXiv:hep-ph/0405132.
[10] T. Inami and C. S. Lim, Prog. Theor. Phys. **65**, 297 (1981).
[11] G. Buchalla and A. J. Buras, Nucl. Phys. **B548**, 309 (1999).
[12] G. Buchalla and A. J. Buras, Nucl. Phys. **B398**, 285 (1993).
[13] M. Musiak and J. Urban, Phys. Lett. B **451**, 161 (1999).
[14] A. J. Buras, M. Gorbahn, U. Haisch, and U. Nierste, Phys. Rev. Lett. **95**, 261805 (2005).
[15] A. J. Buras *et al.*, J. High Energy Phys. 11 (2006) 002.
[16] G. Isidori, F. Mescia, and C. Smith, Nucl. Phys. **B718**, 319 (2005).
[17] W. J. Marciano and Z. Parsa, Phys. Rev. D **53**, R1 (1996).
[18] W. M. Yao *et al.* (Particle Data Group), J. Phys. G **33**, 1 (2006).
[19] D. Rein and L. M. Sehgal, Phys. Rev. D **39**, 3325 (1989); J. S. Hagelin and L. S. Littenberg, Prog. Part. Nucl. Phys. **23**, 1 (1989); M. Lu and M. B. Wise, Phys. Lett. B **324**, 461 (1994); S. Fajfer, Nuovo Cimento Soc. Ital. Fis. **110A**, 397 (1997); C. Q. Geng, I. J. Hsu, and Y. C. Lin, Phys. Rev. D **54**, 877 (1996).
[20] F. Mescia and C. Smith, Phys. Rev. D **76**, 034017 (2007).
[21] A. J. Buras *et al.*, Nucl. Phys. **B714**, 103 (2005).
[22] G. Isidori, F. Mescia, P. Paradisi, C. Smith, and S. Trine, J. High Energy Phys. 08 (2006) 064.
[23] A. J. Buras *et al.*, Phys. Lett. B **500**, 161 (2001).
[24] A. J. Buras *et al.*, Nucl. Phys. **B566**, 3 (2000).
[25] C. H. Chen, J. Phys. G **28**, L33 (2002).
[26] G. Bhattacharyya and A. Raychaudhuri, Phys. Rev. D **57**, R3837 (1998).
[27] A. Deandrea, J. Welzel, and M. Oertel, J. High Energy Phys. 10 (2004) 038.
[28] G. Buchalla, G. Burdman, C. T. Hill, and D. Kominis, Phys. Rev. D **53**, 5185 (1996).
[29] Z. J. Xiao, Chin. Phys. Lett. **16**, 712 (1999).
[30] Z. J. Xiao, C. S. Li, and K. T. Chao, Eur. Phys. J. C **10**, 51 (1999).
[31] Z. J. Xiao, L. X. Lu, H. K. Guo, and G. R. Lu, Eur. Phys. J. C **7**, 487 (1999).
[32] T. Hattori, T. Hasuike, and S. Wakaizumi, Phys. Rev. D **60**, 113008 (1999).
[33] K. Agashe and M. Graesser, Phys. Rev. D **54**, 4445 (1996).
[34] X. G. He and G. Valencia, Phys. Rev. D **70**, 053003 (2004).
[35] B. Machet, Mod. Phys. Lett. A **15**, 579 (2000).
[36] Y. Grossman, Nucl. Phys. **B426**, 355 (1994).
[37] D. S. Gorbunov and V. A. Rubakov, Phys. Rev. D **64**, 054008 (2001).
[38] A. J. Buras, M. Spranger, and A. Weiler, Nucl. Phys. **B660**, 225 (2003).
[39] W. F. Chang and J. N. Ng, J. High Energy Phys. 12 (2002) 077.
[40] G. Burdman, Phys. Rev. D **66**, 076003 (2002).
[41] M. Blanke, A. J. Buras, A. Poschenrieder, S. Recksiegel, C. Tarantino, S. Uhlig, and A. Weiler, J. High Energy Phys. 01 (2007) 066.
[42] M. Blanke, A. J. Buras, S. Recksiegel, C. Tarantino, and S. Uhlig, J. High Energy Phys. 06 (2007) 082.
[43] C. H. Chen, C. Q. Geng, and T. C. Yuan, Phys. Rev. D **75**, 077301 (2007).
[44] C. Promberger, S. Schatt, and F. Schwab, Phys. Rev. D **75**, 115007 (2007).
[45] R. J. Oakes, Phys. Rev. **183**, 1520 (1969).
[46] U. Camerini *et al.*, Phys. Rev. Lett. **23**, 326 (1969).
[47] D. Ljung and D. Cline, Phys. Rev. D **8**, 1307 (1973).
[48] J. H. Klems, R. H. Hildebrand, and R. Steining, Phys. Rev. D **4**, 66 (1971).
[49] G. D. Cable *et al.*, Phys. Rev. D **8**, 3807 (1973).
[50] Y. Asano *et al.*, Phys. Lett. B **107**, 159 (1981).
[51] M. S. Atiya *et al.*, Nucl. Instrum. Methods Phys. Res., Sect. A **321**, 129 (1992).
[52] S. Adler *et al.*, Phys. Rev. Lett. **76**, 1421 (1996).
[53] M. S. Atiya *et al.*, Phys. Rev. D **48**, R1 (1993).
[54] S. Adler *et al.*, Phys. Rev. D **70**, 037102 (2004); Phys. Lett. B **537**, 211 (2002).
[55] S. Adler *et al.*, Phys. Rev. Lett. **88**, 041803 (2002); **84**, 3768 (2000); **79**, 2204 (1997).
[56] B. Bassalleck *et al.*, BNL Report No. BNL-67247, TRIUMF Report No. TRI-PP-00-06, 1999; http://www.phy.bnl.gov/e949/.

[57] D. A. Bryman *et al.*, Nucl. Instrum. Methods Phys. Res., Sect. A **396**, 394 (1997).
[58] M. Atiya *et al.*, Nucl. Instrum. Methods Phys. Res., Sect. A **279**, 180 (1989).
[59] E. W. Blackmore *et al.*, Nucl. Instrum. Methods Phys. Res., Sect. A **404**, 295 (1998).
[60] R. A. McPherson, Ph.D. thesis, Princeton University, 1995.
[61] I. H. Chiang *et al.*, IEEE Trans. Nucl. Sci. **42**, 394 (1995).
[62] T. K. Komatsubara *et al.*, Nucl. Instrum. Methods Phys. Res., Sect. A **404**, 315 (1998).
[63] T. Yoshioka *et al.*, IEEE Trans. Nucl. Sci. **51**, 334 (2004).
[64] J. Doornbos *et al.*, Nucl. Instrum. Methods Phys. Res., Sect. A **444**, 546 (2000).
[65] O. Mineev *et al.*, Nucl. Instrum. Methods Phys. Res., Sect. A **494**, 362 (2002).
[66] A. V. Artamonov *et al.*, Phys. Lett. B **623**, 192 (2005).
[67] H. Brafman *et al.*, IEEE Trans. Nucl. Sci. **32**, 336 (1985).
[68] The reference manual can be found at http://ppd.fnal.gov/elec/dyc3.
[69] The reference manual can be found in either http://midas.triumf.ca or http://midas.psi.ch.
[70] N. Khovansky *et al.*, Nucl. Instrum. Methods Phys. Res., Sect. A **351**, 317 (1994).
[71] W. R. Nelson *et al.*, SLAC Report No. SLAC 265, 1985.
[72] C. Caso *et al.*, Eur. Phys. J. C **3**, 1 (1998).
[73] P. Meyers, E787 Technical Note No. 77, 1985 (unpublished).
[74] A. J. Stevens, E787 Technical Note No. 140, 1987 (unpublished).
[75] J. B. Birks, Proc. Phys. Soc. London Sect. A **64**, 874 (1951).
[76] The reference manual can be found at http://paw.web.cern.ch/paw/mlpfit/pawmlp.html.
[77] A. V. Artamonov *et al.*, Phys. Rev. D **72**, 091102 (2005).
[78] F. Wilczek, Phys. Rev. Lett. **49**, 1549 (1982); J. L. Feng, T. Moroi, H. Murayama, and E. Schnapka, Phys. Rev. D **57**, 5875 (1998).
[79] T. Junk, Nucl. Instrum. Methods Phys. Res., Sect. A **434**, 435 (1999).
[80] This definition of the central value of the branching ratio has the desirable feature that in the limit of observed candidates $N_{\rm obs}$ with high signal-to-background, the central value is the same as that given by the product of the sensitivity (Sec. III H) and $N_{\rm obs}$ which is the fundamental definition of the branching fraction.
[81] G. J. Feldman and R. D. Cousins, Phys. Rev. D **57**, 3873 (1998).
[82] J. Charles *et al.* (CKMfitter Group), Eur. Phys. J. C **41**, 1 (2005); Updated results and plots available at http://ckmfitter.in2p3.fr.
[83] D. Bryman *et al.*, Int. J. Mod. Phys. A **21**, 487 (2006).